# Important Notice

This copy may be used only for the purposes of research and private study, and any use of the copy for a purpose other than research or private study may require the authorization of the copyright owner of the work in question. Responsibility regarding questions of copyright that may arise in the use of this copy is assumed by the recipient.

UNIVERSITY OF CALGARY

# Interpretation of Time-lapse Surface Seismic Data at a $CO_2$ Injection Site, Violet Grove, Alberta

by

Fuju Chen

A THESIS

SUBMITTED TO THE FACULTY OF GRADUATE STUDIES

IN PARTIAL FULFILLMENT OF THE REQUIREMENTS FOR THE

DEGREE OF MASTER OF SCIENCE

DEPARTMENT OF GEOLOGY AND GEOPHYSICS

CALGARY, ALBERTA

June, 2006

© Fuju Chen 2006

**THE UNIVERSITY OF CALGARY**
**FACULTY OF GRADUATE STUDIES**

The undersigned certify that they have read, and recommended to the Faculty of Graduate Studies for acceptance the thesis entitled "Interpretation of Time-lapse Surface Seismic Data at a $CO_2$ Injection Site, Violet Grove Alberta " submitted by Fuju Chen in partial fulfillment of the requirements for the degree of Master of Science.

Supervisor: Dr. D.C. Lawton
Department of Geology and Geophysics

Dr. R.R. Stewart
Department of Geology and Geophysics

Dr. D. Keith
Department of Chemical and Petroleum Engineering
Department of Economics

Date

## ABSTRACT

Time-lapse seismic technology has been implemented at the Violet Grove $CO_2$ injection pilot to monitor the $CO_2$ injection and storage in the Cardium Formation. A multi-component 2.5D surface seismic baseline survey was acquired in March 2005, prior to $CO_2$ injection; after 9 months of $CO_2$ injection, the first monitor multi-component surface seismic survey was acquired in December 2005.

Different time-lapse analysis methods, such as time shift, amplitude difference, $V_p/V_s$, post-stack impedance inversion, and AVO, were tested. Subtle changes at the Cardium Sand in the PS data and P-wave impedance inversion were found along Line 1 between the monitor and baseline surveys, but differences on Line 2 and 3 and in the 3D volume were less clear.

The analysis showed no significant changes in the seismic data above the reservoir, from which it is interpreted that no leakage is occurring from the reservoir. The lack of predicted anomalies at the Cardium level indicates also that the $CO_2$ is probably confined to a thin layer (<6m) of porous sand in the Cardium Formation.

## ACKNOWLEDGEMENTS

The author would like to express his sincere appreciation and respect to his supervisor Dr. Don Lawton not only for his guidance and encouragement during this research work, but also for his serious and responsible attitude to science and his students.

Special thanks are given to Dr. John Bancroft, Dr. Gary Margrave, Dr. E.S. Krebes, Dr. Robert Stewart, and Dr. Larry Lines for their academic instruction. The author would also like to thank Han-Xing Lu, Kevin Hall, Henry Bland, Rolf Maier, Chuck Ursenbach, Sandy Chen, Duojun Zhang, Zhihong Cao, Xiang Du, Richard Xu, Tingge Wang, Lingping Dong, and Marcia Coueslan for their technical support, kind help, and intelligent suggestions.

The author acknowledges the financial support by the Consortium for Research in Elastic Wave Exploration Seismology (CREWES) at University of Calgary, the Alberta Energy Research Institute (AERI), Natural Resources Canada (NRCan). Hampson-Russell Software Services and Landmark Graphics Corporation donated the soft-wares used in the interpretation. Penn West Petroleum generously supplied access to the observation well and provided logistic support.

## TABLE OF CONTENTS

## LIST OF FIGURES

## LIST OF TABLES

# CHAPTER 1: INTRODUCTION

## 1.1 Project background

In 1999, Canada produced 695 million tonnes (Mt) of $CO_2$ (Figure 1.1). The geological storage of $CO_2$ is a technically feasible way of making significant reductions in emissions of $CO_2$ into the atmosphere (Lawton, 2005). Several commercial $CO_2$ storage projects, such as the Sleipner gas field in the North Sea (Torp and Gale, 2002) and the Weyburn oil field in the Williston Basin in Canada (Herawati, 2002), have been implemented and reported since 1996. At the Sleipner gas field in the North Sea, $CO_2$ has been stripped from the produced natural gas and injected into a sand layer called the Utsira Sand since October 1996 (Figure 1.2). By 2004, nearly 8 million tonnes of $CO_2$ have been injected without any significant operational problems observed in the capture plant or in the injection well (Torp and Gale, 2004). At the Weyburn oil field in Canada, Encana, an operator in the field, began injecting significant amounts of $CO_2$ into the Marly reservoir, in order to enhance oil recovery, in October 2000. Initial $CO_2$ injection rates amounted to about 5000 tonnes/day, and it is anticipated that some 20 Mt of $CO_2$ will be permanently sequestered over the lifespan of the oil field (Herawati and Davis, 2002).

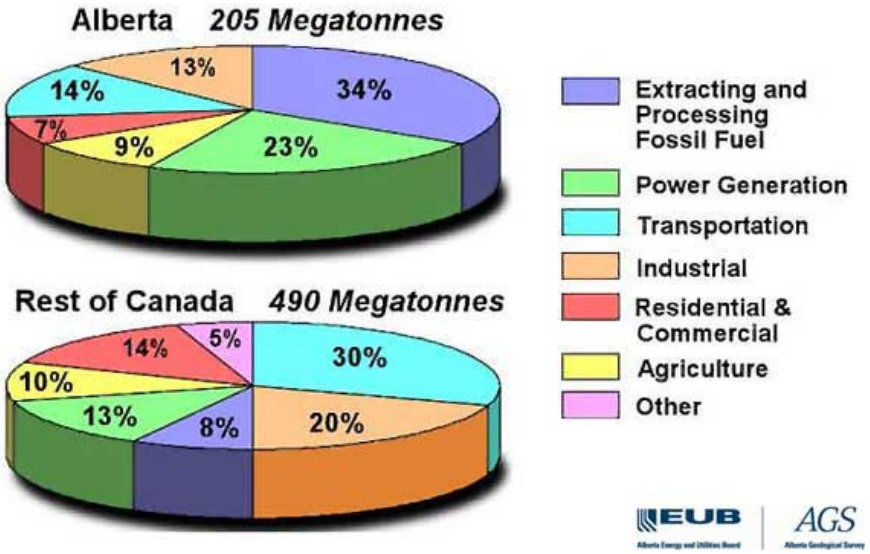


Figure 1.1 Alberta and Canada's $CO_2$ emissions profile in 1999 (from Alberta Geological Survey, 2000).

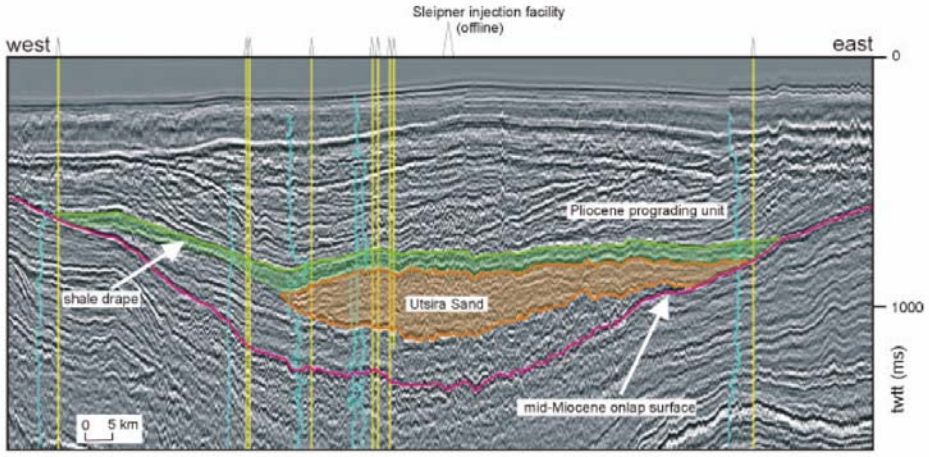


Figure 1.2 A regional seismic line close to the Sleipner field (from Chadwick, 2000).

In Western Canada, most of $CO_2$ emissions are from large stationary sources, such as thermal power plants, refineries, oil sand plants and cement plants. In addition, there are approximately 10,300 oil pools and 31,100 gas pools in the underlying Alberta and Williston sedimentary basins (Bachu, 2004), most of which are in the phase of

secondary and tertiary recovery. These conditions make it a viable option to reduce $CO_2$ emissions into the atmosphere by injecting it into depleted oil/gas reservoirs and for $CO_2$-flood enhanced oil recovery (EOR).

In 2004, an Alberta-based multidisciplinary $CO_2$ storage and monitoring program was instituted by Alberta Department of Energy (ADOE). The Violet Grove $CO_2$ injection site, operated by Penn West Petroleum Inc., is one of the four $CO_2$ EOR pilots and it was chosen for $CO_2$ storage and monitoring research (CCCSTN website, 2005).

**1.2 Thesis objectives and structure**

This thesis has two objectives. The main one is to identify the $CO_2$ distribution in the Cardium reservoir and monitor any possible $CO_2$ leakage at the Violet Grove $CO_2$ injection site by using time-lapse surface seismic data; the second one is to test different seismic methods and find the most effective methods for $CO_2$ monitoring.

This thesis is composed of 6 chapters. Chapter 1 gives a brief introduction about the $CO_2$ monitoring project, geological background of the $CO_2$ injection site, time-lapse technology, and the datasets used. In Chapter 2, a fluid substitution model is evaluated using the Gassmann method. The theory and assumptions of the Gassmann equations are discussed and modeling results are presented. Analysis and interpretation of time-lapse surface seismic data is presented in Chapter 3. Synthetic seismograms and seismic data calibration are introduced at the beginning of this chapter, followed by the seismic

interpretation. Time shift, amplitude difference, and $V_p/V_s$ analysis methods are presented. At the end of this chapter, the PS data is assessed to discriminate between fluid substitution anomalies and those caused by changes in effective stress. Post-stack impedance inversion and AVO inversion are presented in Chapters 4 and 5, respectively. Finally, in Chapter 6, the reservoir characters of the Cardium sand at the Violet Grove $CO_2$ injection site are compared with those of the Utsira sand at the Sleipner $CO_2$ project in the North Sea and conclusions are drawn.

### 1.3 Geological background of the Violet Grove CO2 injection site

The Violet Grove $CO_2$ injection site is located at the center of the Pembina Oil Field, approximately 120 km southwest of Edmonton in west-central Alberta, Canada (Figure 1.3). The Pembina Oil Field, discovered in 1953, is the largest conventional onshore oil field discovered in Canada and the United States. It extends over an area of approximately 3,000 $km^2$ and contains an estimated 7.4 billion barrels of original oil in place with gravity ranging from about 40˚ API to greater than 45˚ API (Nielsen, 1984). This field is a classical stratigraphic trap. The principal producing reservoir is the sandstone in the Upper Cretaceous Cardium Formation (Figure 1.4), which is bounded by black shales of the Blackstone Formation below and the Wapiabi Formation above. There is no evidence of disturbance from faults for the Cardium reservoir; therefore, it should be an ideal place for $CO_2$ storage.

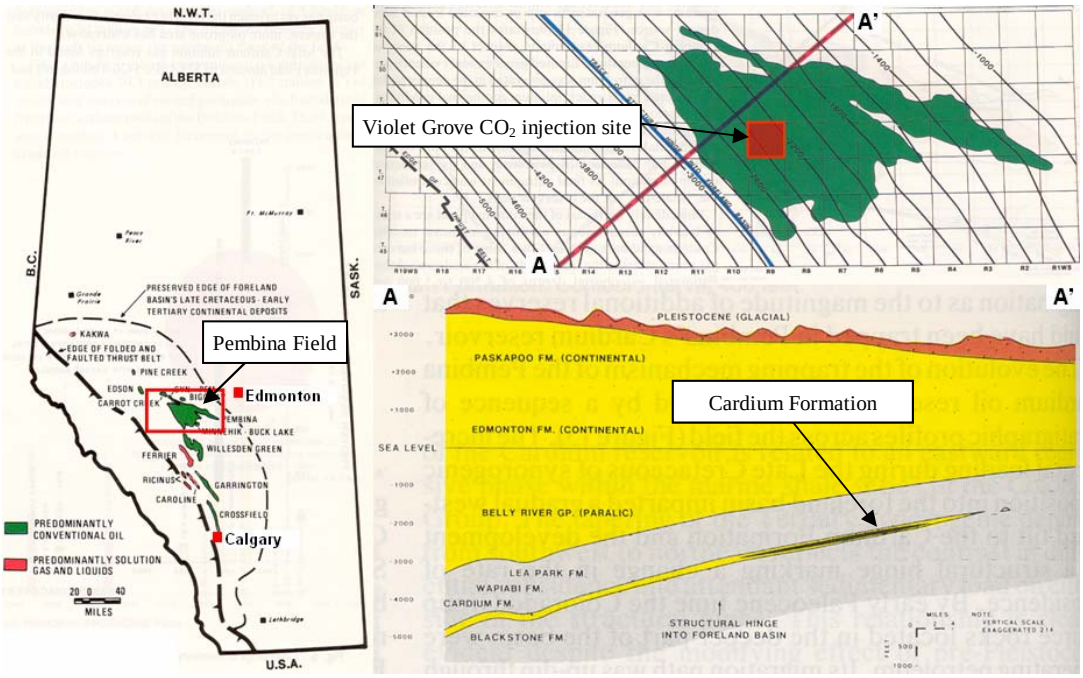


Figure 1.3 Location map of the Violet Grove $CO_2$ injection site (Nielsen, 1984).

The Cardium Formation consists of two lithostratigraphic units: the upper Cardium Zone Member and the lower Pembina River Member (Krause, 1984). The Cardium Zone Member is characterized by a bioturbated and finely laminated, black shale and shaly siltstone interval with infrequent pebbly stringers; on wire-line logs, it has a blocky resistivity profile (Figure 1.5). The Pembina River Member is characterized by an upwardly coarsening sequence, from shale through sandstone to conglomerate; on wire-line logs, there is a gradual upward increase in resistivity (Figure 1.5).

The main reservoirs of the Cardium Formation are the sands and conglomerates at the top of the Pembina River Member, with a total thickness of approximately 20m and a net thickness of about 6 m, respectively. The average porosity of the Cardium sands is

approximately 10%-20%. At the $CO_2$ injection site, the depth of the Cardium reservoir is of approximately 1650m below surface. The reservoir pressure and temperature are 19 MPa and 50 ˚C, respectively (Chalaturnyk, 2005). The oil produced at the Violet Grove is approximately 40˚ API.

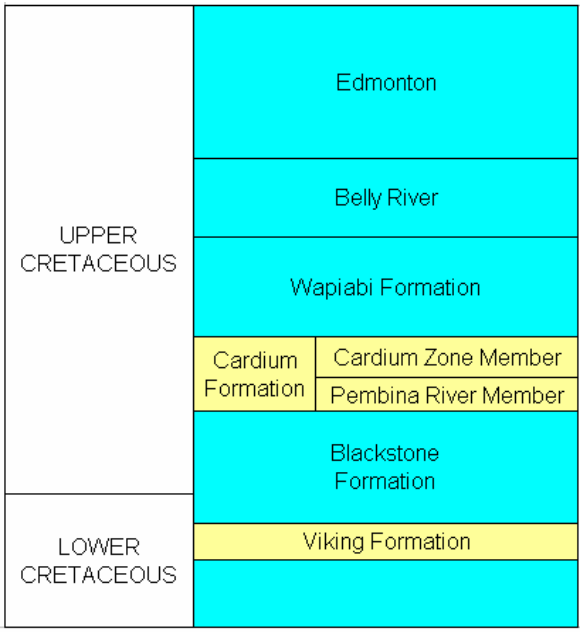


Figure 1.4 Stratigraphic column showing Lower and Upper Cretaceous strata in Pembina Oil Field (after Krause, 1984).

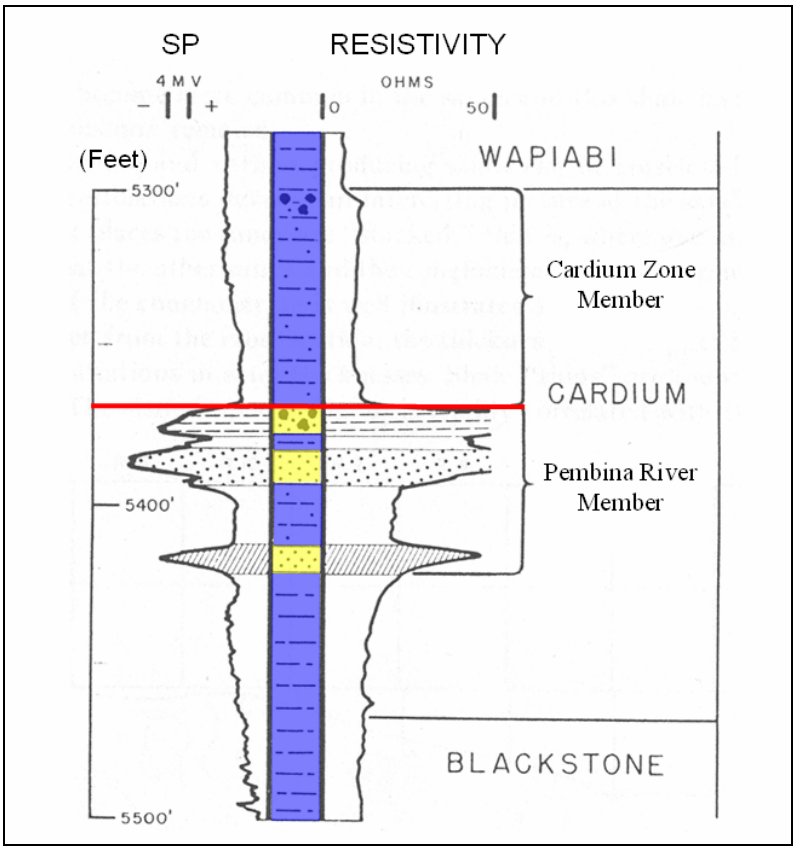


Figure 1.5 Typical logs of the Cardium Formation (from Patterson, 1957).

### 1.4 $CO_2$ monitoring and time-lapse seismic technology

The monitoring and verification of $CO_2$ storage is critically important because the public must be assured that the $CO_2$ has been removed permanently from the atmosphere. Time-lapse seismic technology is one of the integrated monitoring technologies. Petrophysical studies show that the seismic properties of rocks are influenced by changes of pore fluids, pressure and temperature, which commonly occur during the production of hydrocarbon reservoirs (Nur, 1989; Wang, 1991; Batzle, 1992). Time-lapse seismic surveys have evolved into a very promising, intensely investigated technique which has

been applied to monitoring the movement of fluid and pressure fronts, and water-oil contact during hydrocarbon production (Meyer, 2001; Gouveia, 2004). By analyzing changes of multiple seismic surveys acquired over a producing reservoir, such as travel time, amplitude, velocity, impedance, and etc., time-lapse seismic data can provide valuable insight on dynamic reservoir properties such as fluid saturation, effective stress and temperature.

The physical basis and feasibility of monitoring $CO_2$ floods by time-lapse seismic has been studied by, for example, Wang (1997; 1998). During $CO_2$ injection, the viscosity of the pore fluid and surface tension are reduced, and the pore fluid type, saturation, temperature, and pressure are changed which may result in anomalies in seismic attributes in the seismic data. Multi-component seismic data can be used to separate anomalies caused by $CO_2$ effect from those caused by changes of effective stress because the P-wave velocity is sensitive to both $CO_2$ saturation and pore pressure, whereas the S-wave velocity is sensitive only to pressure effects and is less sensitive to the $CO_2$ effect. Some case studies on monitoring $CO_2$ storage by time-lapse seismic have been described in recent years (e.g., Arts, 2002; Li, 2003). For example, to monitor the injected $CO_2$ at the Sleipner gas field, a project called the saline aquifer $CO_2$ storage (SACS) was established in 1998. As part of the SACS project, 3D seismic surveys have been used to monitor movement of $CO_2$ in the Utsira Formation. A baseline 3D survey

was recorded in 1994 prior to $CO_2$ injection, and the first monitor survey was acquired in 1999, after about 2 million tonnes of $CO_2$ had been injected. There exist strong amplitude differences and time shifts between the monitor and baseline surveys corresponding to layers of $CO_2$ saturated rock (Figures 1.6 and 1.7).

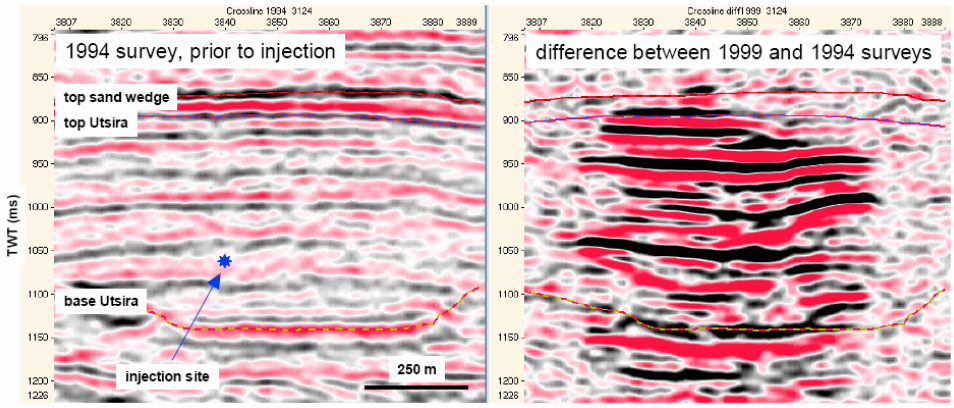


Figure 1.6 Seismic sections through the Sleipner $CO_2$ injection site. The monitor survey was shot in October 1999, when approx. 2.34 million tonnes of $CO_2$ had been injected (from Zweigel et al., 2001).

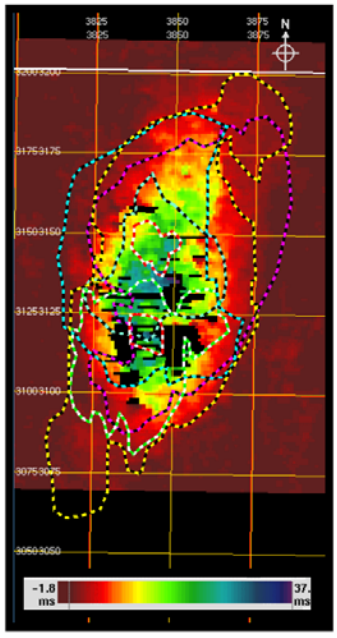


Figure 1.7 Time shift in milliseconds resulting from the cross-correlation between the seismic reflections below the $CO_2$ bubble of the 1994 survey (before injection) and the 1999 survey (from Arts, 2002).

### 1.5 Time-lapse seismic acquisition and processing at Violet Grove

To monitor $CO_2$ injection and discriminate between changes in the seismic response due to $CO_2$ from those due to pressure, a multi-component 2.5D surface seismic baseline survey was acquired in March 2005 by Veritas DGC Inc. with a 2 kg dynamite charge, prior to $CO_2$ injection. It consists of two parallel, multi-component lines, 400 m apart and oriented east-west, and one orthogonal multi-component north-south line. All lines are 3 km long. Two additional short north-south receiver lines of 0.8 km length were also

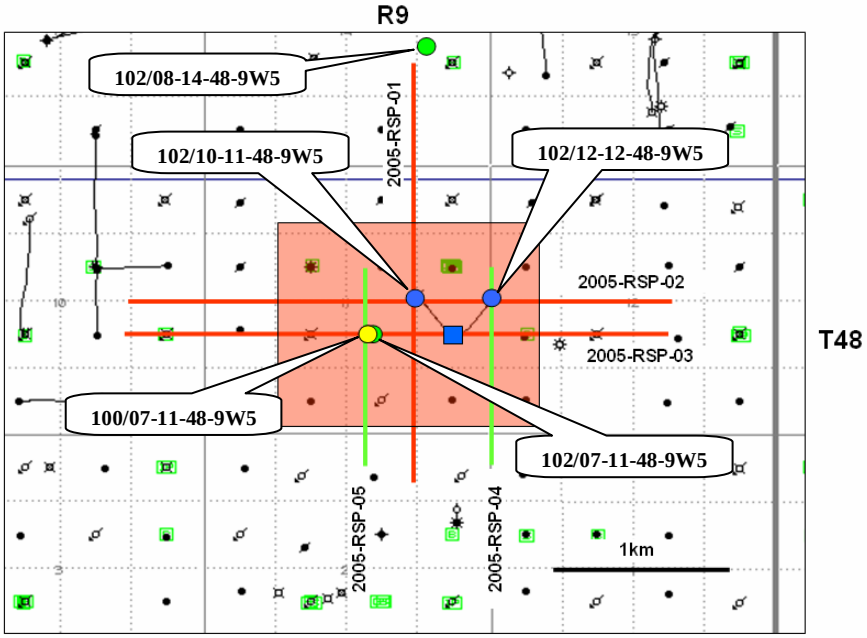


Figure 1.8 The Violet Grove $CO_2$ injection site map. Multi-component seismic lines are shown in red, receivers-only lines are shown in green. The 3D survey is shown by a semi-transparent red rectangle. The observation (VSP) well is shown by a yellow circle, the $CO_2$ injection wells are shown by blue circles, and the wells with digital logs are shown by green circles.

included to provide additional seismic coverage around the injection zone (Lawton, 2005; Figure 1.8). During acquisition, all lines were live with a receiver interval of 20m and a source interval of 40m. Acquisition parameters for the survey are summarised in Table 1.1. The fold map at the Cardium level is shown in Figure 1.9, in which we see that the stacking fold is greater than 12 around the observation well and the $CO_2$ injection pad. The fold along the 2D lines is much higher (250). 3D visualization of the Violet Grove baseline seismic survey is shown in Figure 1.10. Generally speaking, the quality of the seismic data is good.

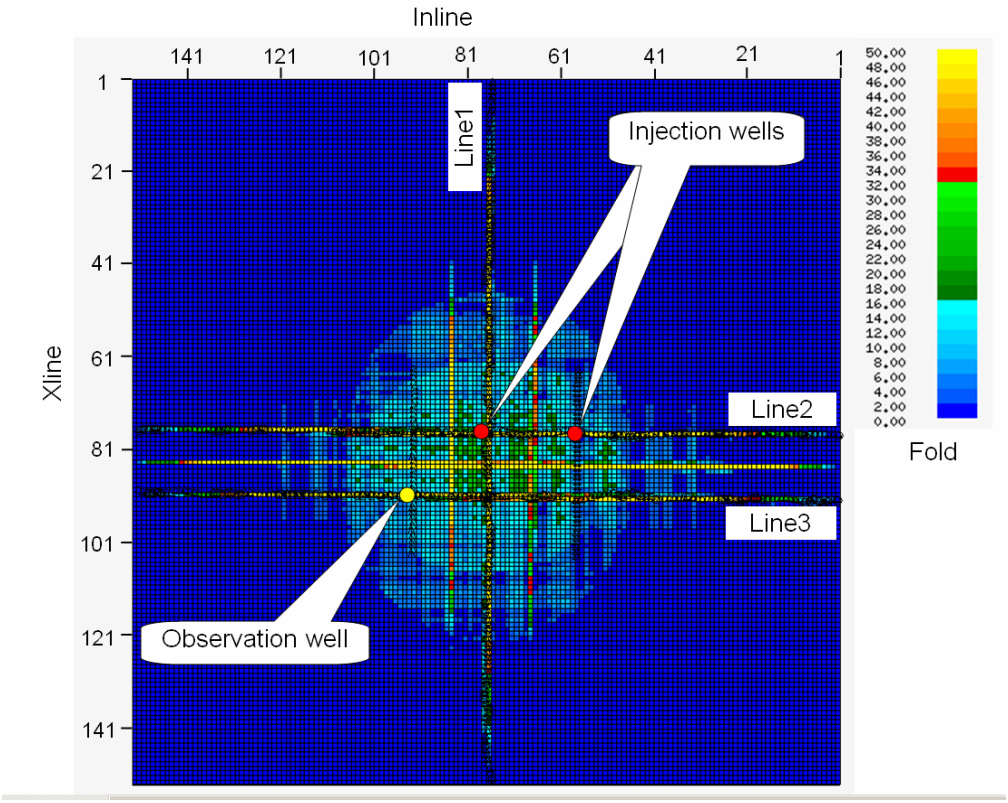


Figure 1.9 The stacking fold at the Cardium reservoir at the Violet Grove $CO_2$ injection site.

| Acquisition parameter | Value |
|---|---|
| Source spacing | 40 m |
| Source type | 2 Kg dynamite |
| Source depth | 15 to18 m |
| Receiver spacing | 20 m |
| Receiver type | Sercel DSU 3C |
| Instruments | Sercel 408 XL |
| Sample interval | 1 ms |

Table 1.1 Acquisition parameters for the Violet Grove $CO_2$ seismic monitoring program (Lawton, 2005).

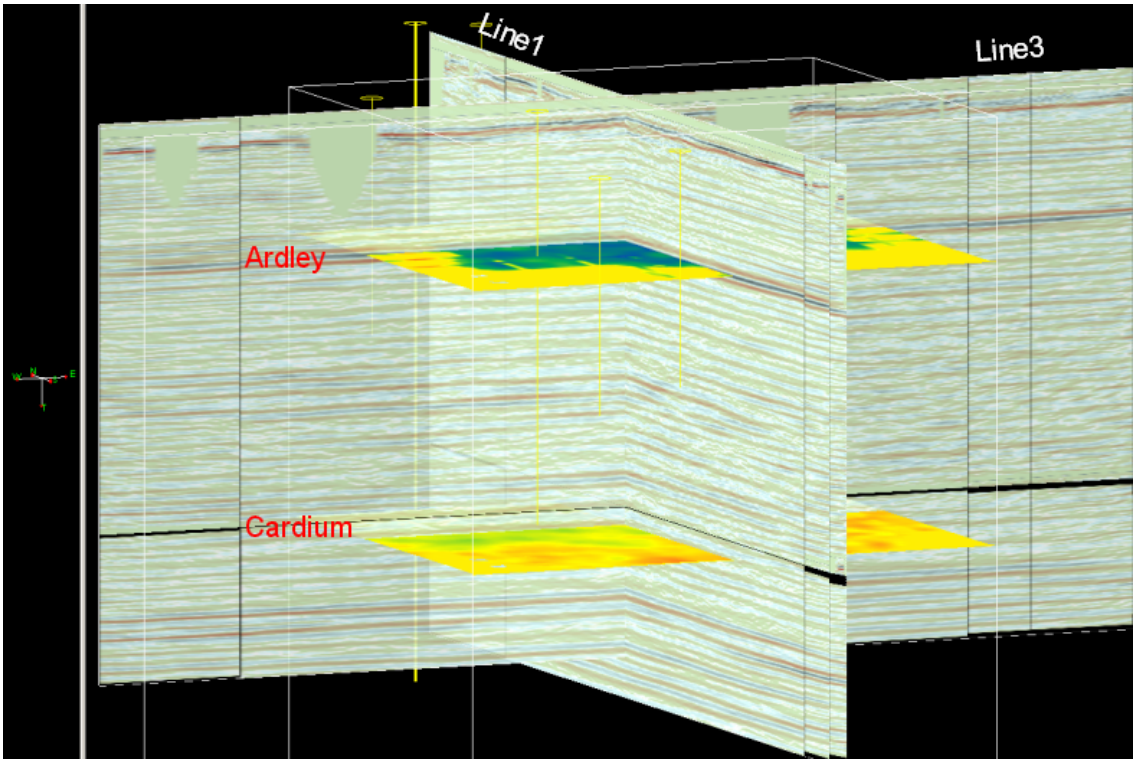


Figure 1.10 3D visualization of the Violet Grove baseline seismic survey

After 9 months of $CO_2$ injection (approximately 20, 000 tonnes), the first monitor multi-component surface seismic survey was acquired in December 2005, with as same acquisition parameters as the baseline survey.

The baseline and monitor surface seismic data were processed by Veritas DGC of Calgary with all non-repeated shots included. The 2D lines were processed as individual lines and also as a sparse 3D volume, which covers the injection pad. The processing flows are:

(1) PP 2D data processing flow:

1 Manual trace edits
2 Amplitude recovery: T-function
3 Min. phase surface consistent decon: OPR: 60 ms, pre-white: 0.1%, decon window: (0 2000 m, 100 2300 1200 2400ms)
4 Datum: 910 m; replace velocity: 2500 m/s; weather velocity: 950 m/s
5 Tomographic near surface refraction statics
6 Preliminary velocity analysis – DSR NMO from surface
7 Statics-automatic surface consistent
8 Spectral balancing: 5-160 Hz
9 Final velocity analysis - DSR NMO from surface
10 Statics-automatic surface consistent
11 First break mute
12 Structure statics – CDP trim
13 AGC, stack, FX deconvolution noise attenuation
14 Kirchhoff migration: 100% velocities
15 Filter: frequency: 5/10-100/120 Hz

(2) PS 2D data processing flow:

1 Polarization filter, manual trace edits
2 Amplitude recovery: TV-function for PS
3 Min. phase decon: OPR: 180ms, pre-white: 0.1%, decon window: (0 2000 m, 100 2700 1100 3000 ms)
4 Datum: 910m; replace velocity: 2500 m/s weather velocity: 950 m/s

5 Tomographic near surface refraction statics (shot only)
6 Intermediate $V_p/V_s$ analysis - DSR NMO from surface
7 Statics-automatic surface consistent
8 Noise attenuation
9 Spectral balancing: 6 - 70 Hz
10 Final $V_p/V_s$ analysis-DSR NMO from surface
11 Statics-automatic surface consistent, first break mute
12 Structure statics-ACP trim
13 AGC, CCP binning and stack
14 FX deconvolution noise attenuation
15 Kirchhoff migration: 100% velocities
16 Filter: frequency: 2/5-50/70 Hz

## (3) PP 3D data processing flow:

1 Tilt correction, manual trace edits
2 Min. phase surface consistent decon: OPR: 60 ms, pre-white: 0.1% , decon window: (0 2000 m 100 2300 1200 2400 ms)
3 Tomographic near surface structure statics (short wave)-2 layer drift
4 Datum: 910m; replacement velocity: 2500 m/s; weather velocity: 950 m/s
5 Preliminary double square root velocity analysis -NMO from surface
6 Statics – automatic surface consistent
7 Final DSR velocity analysis -NMO from surface
8 Spectral whitening, SC scaling, first break mute, 500 ms AGC
9 Structure statics (long wave)-2 layer drift statics - CDP trim
10 Stack, SW slant stack noise attenuation, 3D Kirchhoff migration
11 Filter: 5/10-100/120 Hz

## (4) PS 3D data processing flow:

1 Tilt correction, polarization filter, manual trace edits
2 Amplitude recovery: TV-function for PS
3 Min. phase decon: OPR: 180 ms, pre-white: 0.1%, decon window: (0 2000 m, 100 2700 1100 3000 ms)
4 Tomographic near surface structure statics (shot only)
5 Datum: 910 m; replacement velocity: 2500 m/s; weather velocity: 950 m/s
6 Preliminary $V_p/V_s$ analysis-DSR NMO from surface
7 Statics-station drift estimation, residual
8 Intermediate $V_p/V_s$ analysis -DSR NMO from surface, residual statics
9 Noise attenuation, spectral balancing
10 Final $V_p/V_s$ analysis -DSR NMO from surface, residual statics

11 Trim statics, CCP binning and stack
12 SW slant stack noise attenuation, 3D Kirchhoff migration
13 Filter: 5/10-50/70 Hz

The baseline and monitor surface seismic data were reprocessed by CREWES in 2006 with all the non-repeated shots excluded. The processing flows for 2D and 3D data are same (Table 1.2).

The baseline P-wave sections of Line 1 processed by Veritas and CREWES are shown in Figure 1.11 and 1.12, respectively. The datasets processed by Veritas were used only for $V_p/V_s$ analysis. The datasets processed by CREWES were used for all the other analysis and interpretation.

| | |
|---|---|
| TRACE EDIT<br>TRUE AMPLITUDE RECOVERY<br>SURFACE CONSISTENT DECONVOLUTION<br>TIME VARIANT SPECTRAL WHITENING<br>ELEVATION AND REFRACTION STATIC CORRECTIONS<br>VELOCITY ANALYSIS<br>RESIDUAL SURFACE CONSISTENT STATICS<br>NORMAL MOVEOUT<br>TRIM STATICS<br>FRONT END MUTING<br>CDP STACK<br>TIME VARIANT SPECTRAL WHITENING<br>TRACE EQUALIZATION<br>F-XY DECONVOLUTION<br>PHASE-SHIFT MIGRATION<br>FOR TRACE DISPLAY:<br>TRACE EQUALIZATION<br>BANDPASS FILTER<br>TIME VARIANT SCALING | TRACE EDIT<br>ASYMPTOTIC BINNING<br>SURFACE CONSISTENT DECONVOLUTION<br>TIME VARIANT SPECTRAL WHITENING<br>ELEVATION STATICS<br>APPLY FINAL REFRACTION AND RESIDUAL STATICS FROM P-P<br>CONSTRUCT INITIAL P-SV VELOCITY FROM FINAL P-P VEL.<br>VELOCITY ANALYSIS<br>RECEIVER RESIDUAL STATICS (HAND STATICS)<br>VELOCITY ANALYSIS<br>CONVENTIONAL RESIDUAL STATICS<br>VELOCITY ANALYSIS<br>NORMAL MOVEOUT<br>ACP TRIM STATICS<br>FRONT END MUTING<br>ACP STACK (DEPTH-VARIANT STACK AND DMO STACK)<br>TIME VARIANT SPECTRAL WHITENING<br>TRACE EQUALIZATION<br>F-XY DECONVOLUTION<br>PHASE-SHIFT MIGRATION<br>FOR TRACE DISPLAY:<br>TRACE EQUALIZATION<br>BANDPASS FILTER<br>TIME VARIANT SCALING |

Table 1.2 PP (left) and PS (right) data processing flows used by CREWES (Lu, 2006).

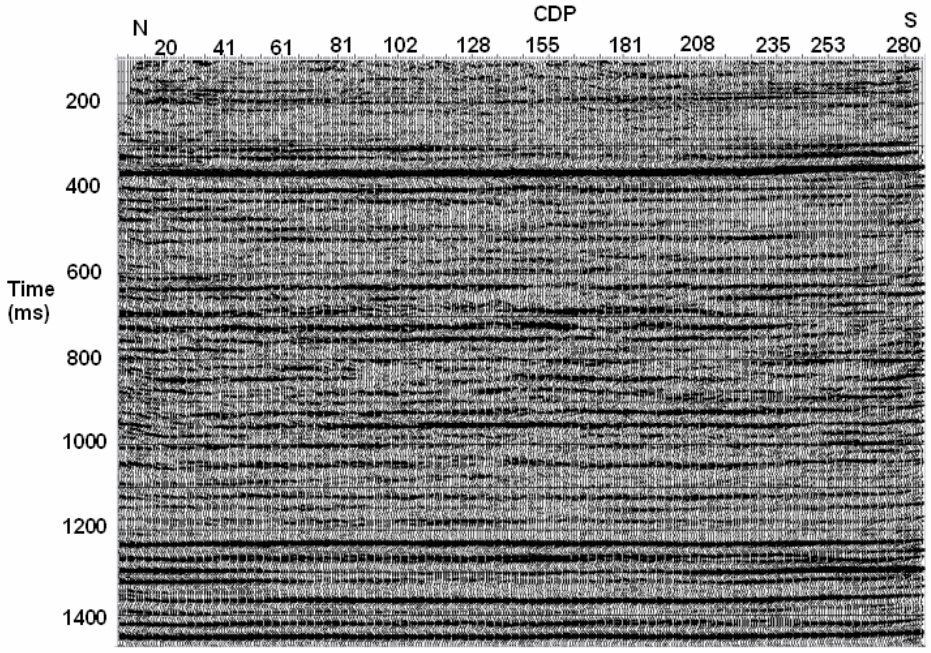


Figure 1.11 P-wave seismic section of Line 1 (baseline, processed by Veritas)

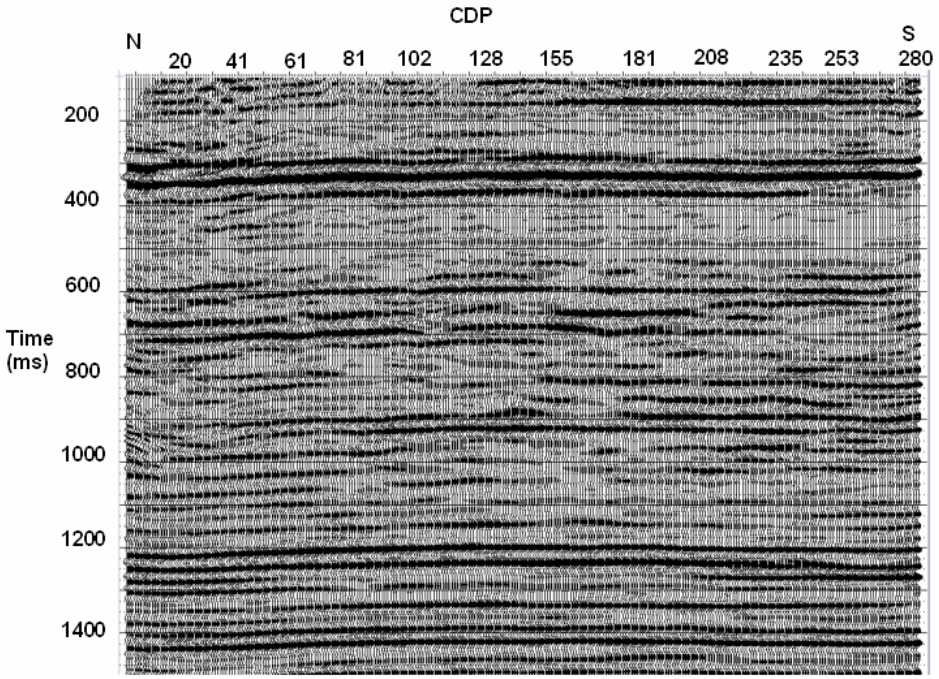


Figure 1.12 P-wave seismic section of Line 1 (baseline, processed by CREWES)

## CHAPTER 2: FLUID SUBSTITUTION: THE GASSMANN METHOD

The effect of fluid substitution on reservoir characterization using seismic data is an important part of seismic attribute work because it provides the interpreter with a tool for modeling and quantifying the various fluid scenarios which might give rise to an observed amplitude variation with offset (AVO) or 4D response (Smith, 2003). The most commonly used approach for fluid substitution at seismic frequencies is based on the work of Gassmann (1951), who calculated the bulk modulus of a fluid-saturated porous medium using the rock porosity, the bulk modulus of the porous rock frame, the bulk modulus of the mineral matrix, and the bulk modulus of the pore-filling fluids.

In exploration seismology, seismic waves carry information about subsurface rocks and fluids in the form of travel time, reflection amplitude, and phase variations (Wang, 2001). Rock physics is an essential link connecting seismic data to the presence of in-situ hydrocarbons and to reservoir characteristics (Han, 2004); on the other hand, rock physics information is also very most important for Gassmann analysis. As a result, rock physics of the Cardium reservoir has to be fully understood to interpret the time-lapse seismic data.

The ultimate goal of fluid substitution modeling and 4D seismic $CO_2$ monitoring is to delineate the changes of seismic properties caused by the injected $CO_2$ and to map the $CO_2$ distribution. To achieve this goal, seismic data has to be able to resolve the

compressibility contrasts between rocks saturated with $CO_2$ versus those saturated with in-situ fluids in the Cardium reservoir. Therefore, understanding the seismic properties of $CO_2$ and the original fluids under in-situ reservoir conditions is required for fluid substitution modeling.

This chapter consists of four parts: theory of Gassmann modeling, determination of required parameters, modeling results & discussions, and conclusions. In the first part, the theory of Gassmann equations and its assumptions are discussed. The second part discusses how to determine all the required rock and fluid parameters for the Gassmann equations. In the third part, the modeling results are presented and several caveats are discussed. Finally, some conclusions are drawn based on the modeling results.

## 2.1 Theory of Gassmann modeling

Correct interpretation of underground fluid variation from seismic data requires a quantitative understanding of the relationships among the velocity data and fluid properties in the form of fluid substitution formulae. These formulae are very commonly based on Gassmann's equations (Berryman, 1999), which relate the saturated bulk modulus of the rock to its porosity, the bulk moduli of the porous rock frame, the mineral matrix, and the pore-filling fluids (Smith, 2003):

$$K_{sat} = K^* + \frac{\left(1 - \frac{K^*}{K_o}\right)^2}{\frac{\phi}{K_{fl}} + \frac{(1-\phi)}{K_o} - \frac{K^*}{K_o^2}} \qquad (2\text{-}1)$$

where,

$K_{sat}$ is the saturated bulk modulus of rocks (un-drained of pore fluids),

$K^*$ is the bulk modulus of the porous rock frame (drained of any pore-filling fluid, but not the dry bulk modulus),

$K_o$ is the bulk modulus of the mineral matrix,

$K_{fl}$ is the bulk modulus of the pore fluids,

Ø is rock porosity.

The shear modulus $\mu_{sat}$ of the rock is assumed to be less affected by fluid saturation, so that:

$$\mu_{sat} = \mu^* \qquad (2\text{-}2)$$

where,

$\mu_{sat}$ is the shear modulus of the rock under saturated conditions, and $\mu^*$ is the rock frame shear modulus.

If P-wave sonic, S-wave sonic and bulk density logs are all available, then the saturated bulk and shear moduli of rocks can be calculated from wire-line log data through the following two equations (Smith, 2003):

$$K_{sat} = \rho_B \left( V_p^2 - \frac{4}{3} V_s^2 \right) \qquad (2\text{-}3)$$

$$\mu_{sat} = \rho_B V_s^2 \qquad (2\text{-}4)$$

If we assume that we have determined the rock porosity (Φ), the rock matrix bulk modulus ($K_o$), and the in-situ fluid bulk modulus ($K_{fl}$), then we can calculate the bulk modulus of the porous rock frame $K^*$, which is held constant during the process of fluid substitution, by using the backward Gassmann equation:

$$K^* = \frac{K_{sat}\left(\frac{\phi K_o}{K_{fl}} + 1 - \phi\right) - K_o}{\frac{\phi K_O}{K_{fl}} + \frac{K_{sat}}{K_o} - 1 - \phi} \qquad (2\text{-}5)$$

After fluid substitution, the in-situ reservoir fluid is substituted by new fluid; therefore, the density and bulk modulus of in-situ fluids ($\rho_{fl}$ and $K_{fl}$) are changed to the density and bulk modulus of the new fluid. This allows us to use the Gassmann equation again to calculate a new saturated bulk modulus for any desired fluid:

$$K_{sat}^{new} = K^* + \frac{\left(1 - \frac{K^*}{K_o}\right)^2}{\frac{\phi}{K_{fl}^{new}} + \frac{(1-\phi)}{K_o} - \frac{K^*}{K_o^2}} \qquad (2\text{-}6)$$

$$\mu_{sat}^{new} = \mu_{sat} \qquad (2\text{-}7)$$

Finally, we can rewrite equations 2-3 and 2-4 and calculate the new P-wave velocity and S-wave velocity:

$$V_p^{new} = \sqrt{\frac{K_{sat}^{new} + \frac{4}{3}\mu_{sat}}{\rho_B^{new}}} \qquad (2\text{-}8)$$

$$V_s^{new} = \sqrt{\frac{\mu_{sat}}{\rho_B^{new}}} \qquad (2\text{-}9)$$

Application of Gassmann's equation is based on the following assumptions: 1) the rock (both the matrix and the frame) is macroscopically homogeneous; 2) all the pores are interconnected or communicating; 3) the pores are filled with a frictionless fluid (liquid, gas, or mixture); 4) the rock-fluid system under study is closed (un-drained); 5) the pore fluid does not interact with the solid in a way that would soften or harden the frame (Wang, 2001).

Wang (2000) compared the Gassmann results and laboratory results of the effect of fluid displacement on seismic properties. He found that the effects of fluid displacements on seismic velocities agree well between the Gassmann-predicted and laboratory-measured values, provided that the frame properties provided to the Gassmann equation are measured at the irreducible water saturation or under moist conditions. He concluded that when the input frame properties are measured at the irreducible water saturation condition, the Gassmann-predicted and the laboratory-measured effects of fluid displacements on seismic properties might be directly applied to 4D seismic feasibility studies and interpretations.

## 2.2 Determination of required parameters

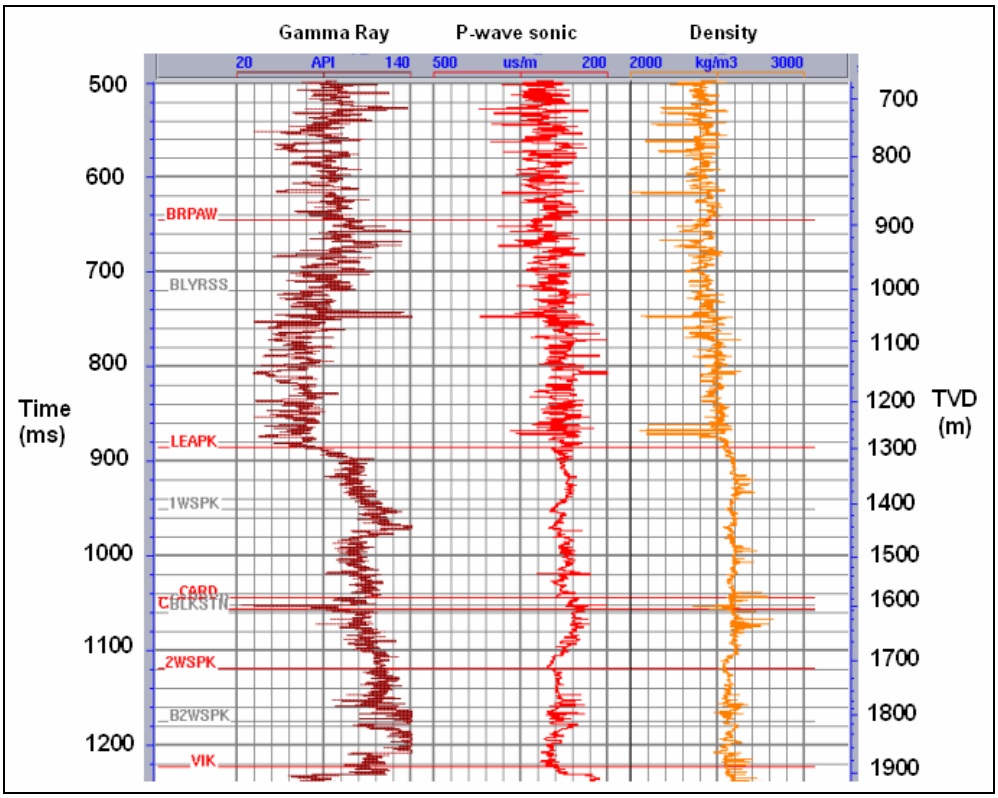


Figure 2.1 Logs of the well 102/08-14-48-9W5

Well 102/08-14-48-9W5, which has gamma ray, density, and P-wave sonic logs, was chosen to carry out the fluid substitution modeling (Figure 2.1). Before using Gassmann equations for fluid substitution, the following parameters must be determined first: (1) the S-wave velocity; (2) the fluid properties ($K_{fl}$, $\rho_{fl}$); (3) the shale content and porosity; and (4) the rock matrix properties ($K_o$). All these parameters can be calculated from log data or inferred from literature.

*2.2.1 S-wave velocity*

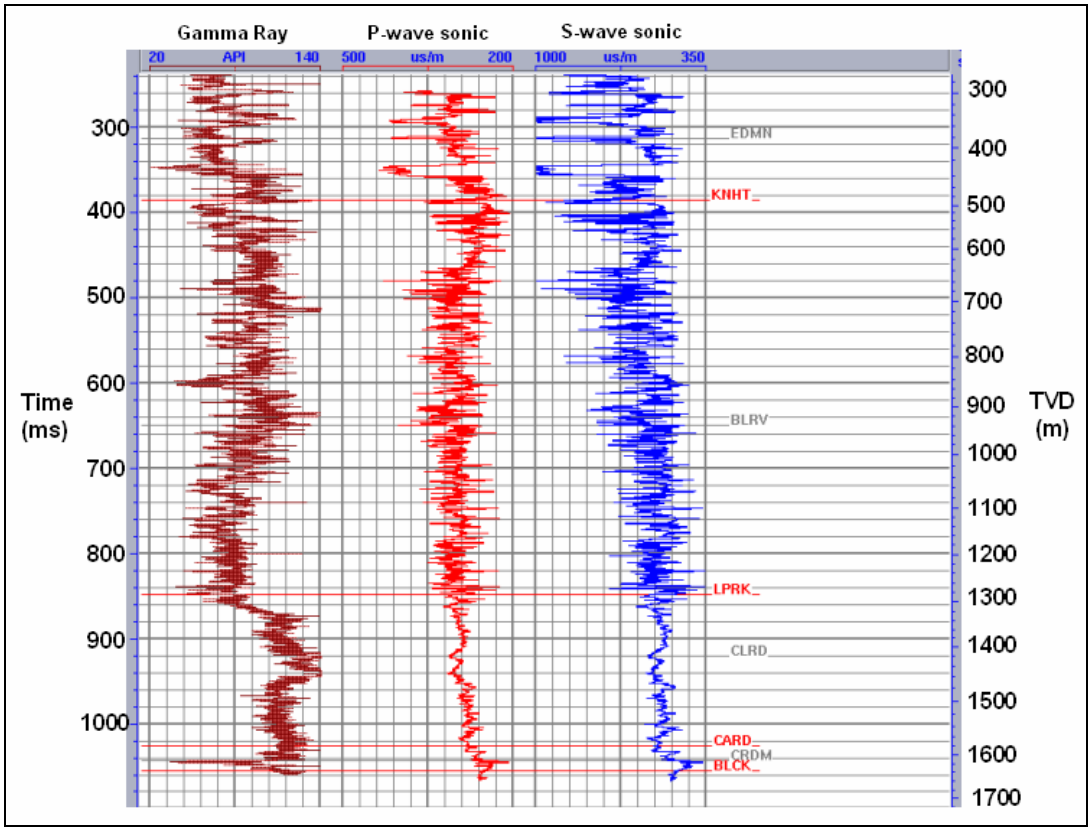


Figure 2.2 Logs of the well 102/07-11-48-9W5

There is no S-wave velocity log available for well 102/08-14-48-9W5. Therefore, the S-wave velocity has to be derived by using empirical or statistical relationships with other logs such as density or P-wave velocity. Castagna et al. (1985) published an empirical relationship between $V_s$ and $V_p$ for water-saturated clastic silicate rocks:

$$V_s = 0.8621V_p - 1172 \text{ (m/s)} \qquad (2\text{-}10)$$

Castagna's method has been widely used in deriving S-wave velocities from P-wave velocities. The global equation (Equation 2-10), however, cannot be used directly

to a local area. A specific correlation between P-wave velocities and S-wave velocities at the Violet Grove area was derived from the well 102/07-11-48-9W5, which has a S-wave log but no density log (Figure 2.2 and 2.3). In Figure 2.3, the red line is the best-fit linear regression line between $V_s$ and $V_p$ derived from the $V_s$ and $V_p$ data of well 102/07-11-48-9W5; the green line is the global Castagna's equation. The green line will underestimate $V_s$ values of shales in this area. The red line gives a good estimation of $V_s$ values of shales, but it will underestimate the $V_s$ values of the Cardium sand (points in the red circle) by about 13%. This is because the S-wave velocities of the Cardium sand are higher than the shales at the Violet Grove area.

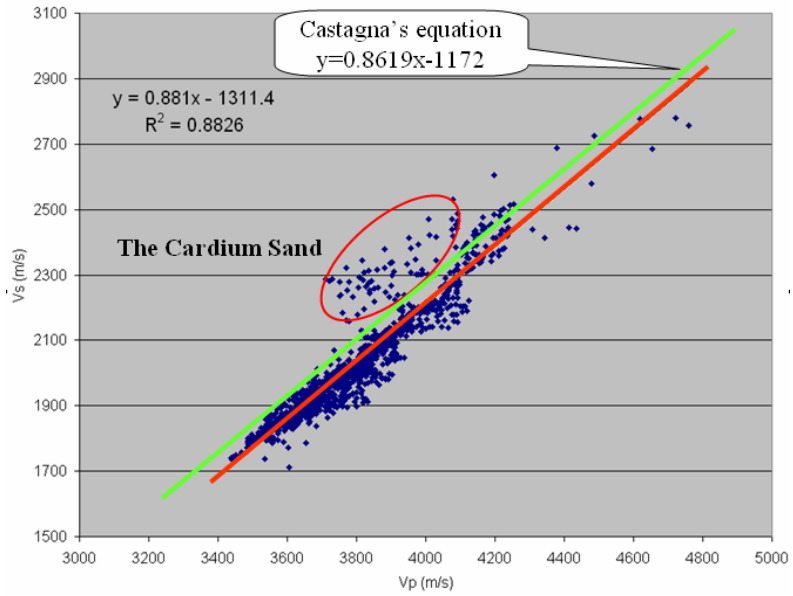


Figure 2.3: $V_s$ versus $V_p$ (well 102/07-11-48-9W5, interval 1500-1665m).

In order to improve the correlation between $V_s$ and $V_p$, the Cardium sand was separated from the overlying and underlying shales (Figures 2.4, 2.5, and 2.6). The

difference between calculated and measured $V_s$ values of the Cardium sand is about 1.8%. The difference between calculated and measured $V_s$ values of shales is about 1%. The S-wave sonic log of well 102/08-14-48-9W5 was derived from its P-wave sonic log by using the three correlation equations.

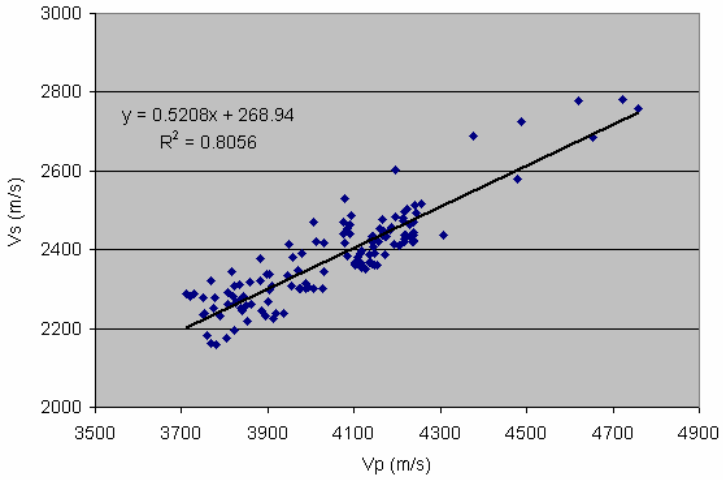


Figure 2.4 $V_s$ versus $V_p$ of the Cardium sand (well 102/07-11-48-9W5, interval 1619-1637m).

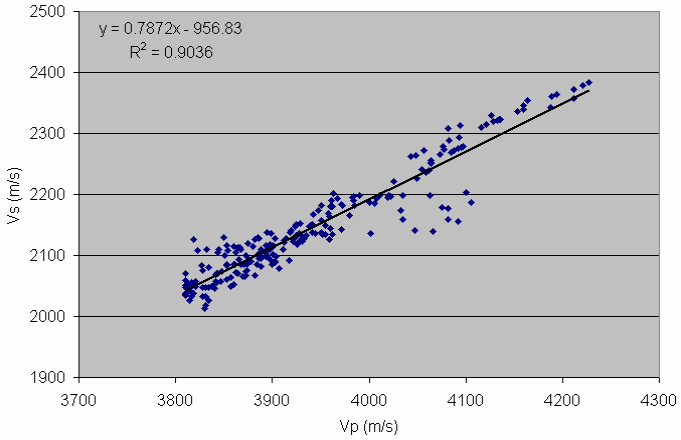


Figure 2.5 $V_s$ versus $V_p$ of shales below the Cardium sand (well 102/07-11-48-9W5, interval 1637-1665m).

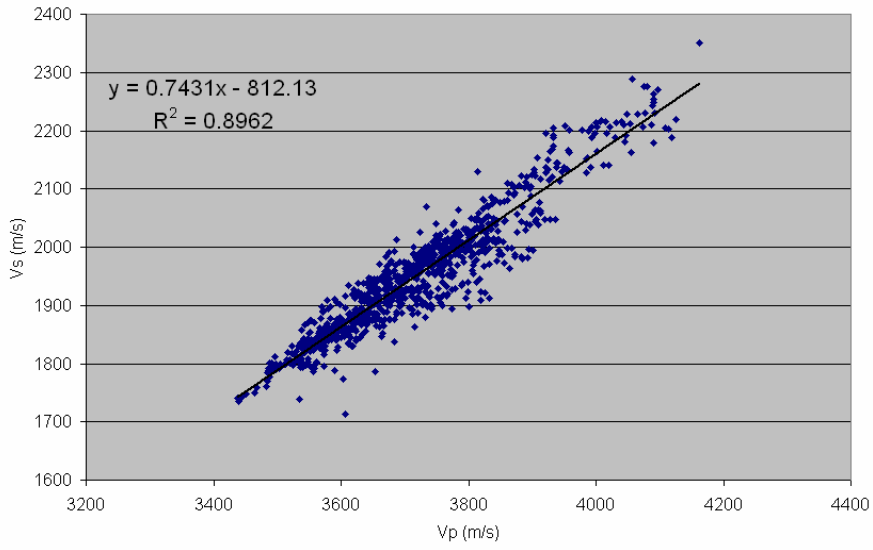


Figure 2.6 $V_s$ versus $V_p$ of shales above the Cardium sand (well 102/07-11-48-9W5, interval 1500-1619m).

*2.2.2 Pore fluid properties ($K_{fl}$, $\rho_{fl}$)*

Pore fluids strongly influence the seismic properties of rocks. The primary properties of pore fluids such as density and bulk modulus vary substantially, but systematically, with fluid composition, pressure, and temperature. Batzle and Wang (1992) summarized seismic properties of commonly encountered pore fluids based on their own data as well as other published studies and presented a set of empirical equations for calculating the bulk moduli and densities of pore fluids as functions of pressure and temperature. In their procedure, the bulk modulus and density of a pore-fluid component are expressed in terms of pore temperature, pressure, salinity, gas oil ratio (GOR), oil gravity (API), and specific gas gravity (API).

**Carbon dioxide ($CO_2$)**

Carbon dioxide ($CO_2$) is a slightly toxic, odourless, colorless gas with a slightly pungent, acid taste. Its typical concentration in the air is about 0.038%. The molecular weight of $CO_2$ is 44.01 g/mol, approximately 1.5 times as heavy as air. $CO_2$ can present gas, liquid, solid, and supercritical phases under different temperature and pressure conditions (Figure 2.7). Considering the in-situ conditions of the Cardium Formation (50 ˚C and 19 MPa), a supercritical phase is expected for the injected $CO_2$, which behaves like a gas, but has a 'liquid' density (Xue, 2004). The density and modulus of $CO_2$ under reservoir conditions are approximately 509 kg/m$^3$ and 0.326 GPa, respectively, which were calculated using Batzle and Wang's equations.

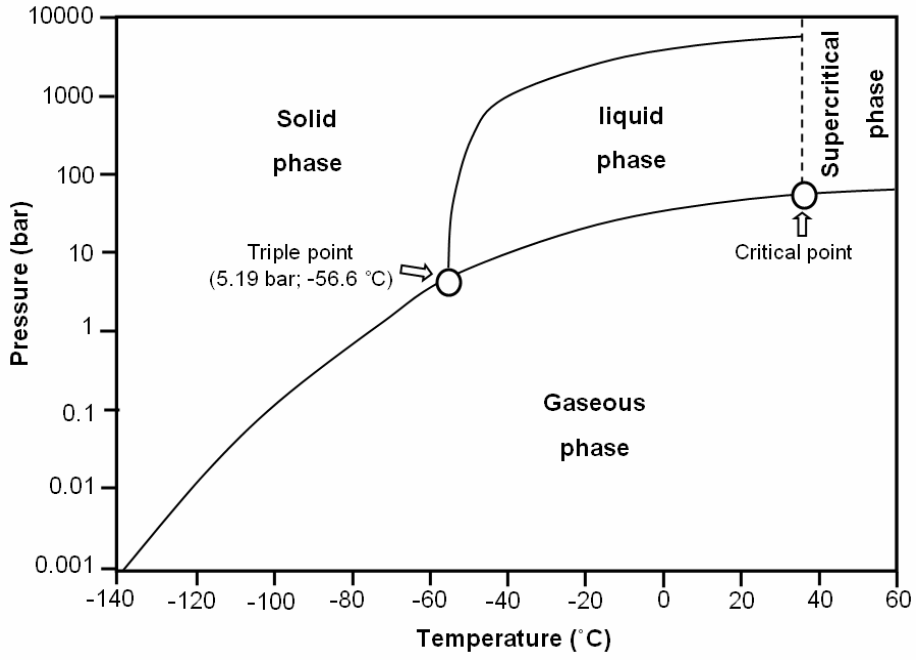


Figure 2.7 Phase diagram for $CO_2$ (from: http://www.acpco2.com, 1MPa=10 bar).

**Hydrocarbon and water**

The original pore fluids at the Violet Grove $CO_2$ injection site include conventional oil with solution gas, and brine (Krause and Collins, 1984). The oil gravity is approximately 40˚ API. The specific gravity of the solution gas (the ratio of the gas density to air density at 15.6 ˚C and atmospheric pressure) is approximately 0.894. The gas-oil-ratio (GOR) is approximately 100, which is estimated from the production data of the adjacent wells. The in-situ bulk density and modulus of oil with dissolved gas are 732 kg/m$^3$ and 0.8104 GPa, respectively. After decades of production and water flooding, the original brine has been diluted by fresh water and now the exact salinity of the formation water is unknown. Therefore, different salinity values were tested during the modeling procedure, and it was proven that this parameter is relatively insensitive to the final results. Thus, a salinity of 40,000 mg/l was used in the fluid substitution analysis. The in-situ density and modulus of the water are 1023 kg/m$^3$ and 2.6582 GPa, respectively, which were calculated by using Batzle and Wang equations.

**Fluid mixture properties**

After the bulk moduli of the pore-fluid components are determined, the effective bulk modulus of a fluid mixture can be calculated by using Wood's (1941) equation:

$$\frac{1}{K_{fl}} = \frac{S_w}{K_w} + \frac{1 - S_w}{K_{hc}}, \qquad (2\text{-}11)$$

where

$S_w$ is water saturation,

$K_w$ is bulk modulus of water,

$K_{hc}$ is bulk modulus of hydrocarbon or $CO_2$.

A simple volumetric mix of the end-member components is used to calculate the density of the fluid mixture:

$$\rho_{fl} = S_w \rho_w + (1 - S_w)\rho_{hc} \ , \qquad (2\text{-}12)$$

where

$\rho_w$ is density of water,

$\rho_{hc}$ is density of hydrocarbon or $CO_2$.

*2.2.3 Shale content and porosity*

Clay is one of the main constituents of the rock matrix of the Cardium sand. Assuming radioactive minerals other than clay are absent, quantitative evaluation of shale content can be derived using gamma ray data:

$$v_{sh} = \frac{GR - GR_{cn}}{GR_{sh} - GR_{cn}} \ , \qquad (2\text{-}13)$$

where

GR is log response in zone of interest (API units),

$GR_{cn}$ is log response of the clean sand (22.5 API, which is determined from the gamma ray log of clean sand of well 102/08-14-48-9W5),

$GR_{sh}$ is log response of the pure shale near the Cardium zone (115 API, which is determined from the gamma ray log of pure shale of well 102/08-14-48-9W5).

Porosity can be derived from the density log. The main mineral constituents of the Cardium sand are quartz, clay, and chert. The statistical ratio of quartz over chert, which is based on core analysis (Krause, 1984), is about 5:1. The exact density and bulk modulus of chert are unknown. In order to make the model simple, the two mineral end members of the Cardium sand were assumed to be quartz and clay. Then the bulk density of the Cardium sand was described by the following equation and the porosity was solved by rewriting it:

$$\rho_B = \rho_{quartz}(1-\phi-v_{shale}) + \rho_{shale}v_{shale} + \rho_{fluid}\phi \quad , \qquad (2\text{-}14)$$

where

$\rho_B$ is bulk density of rock,

$\rho_{quartz}$ is the density of quartz, which equals 2.65 g/cc,

$\rho_{shale}$ is the density of wet shale, which is determined from the density log of pure shale and equals 2590 kg/m$^3$,

$\Phi$ is rock porosity,

$v_{shale}$ is shale content.

*2.2.4 The rock matrix properties*

The bulk modulus of quartz is approximately 40 GPa (Hilterman, 2001). The bulk modulus of wet shale is about 23 GPa, which is calculated from the S-wave sonic and density logs of the pure shale. The bulk modulus of the mineral matrix, $K_o$, is calculated via application of Voigt-Reuss-Hill (VRH) averaging of the mineral constituents (Figure 2.8):

$$K_{\mathrm{Re}uss} = \left[ \frac{F_{sand}}{K_{sand}} + \frac{F_{shale}}{K_{shale}} \right]^{-1} \quad , \quad (2\text{-}15)$$

$$K_{Voigt} = \left[ F_{sand} K_{sand} + F_{shale} K_{shale} \right] \quad , \quad (2\text{-}16)$$

$$K_{vrh} = \frac{1}{2} \left[ K_{Voigt} + K_{\mathrm{Re}uss} \right] \quad , \quad (2\text{-}17)$$

where

$F_{sand}$ and $F_{shale}$ are the volumetric fractions of sand and shale, respectively,

$K_{sand}$ and $K_{shale}$ are the bulk moduli of sand and shale, respectively.

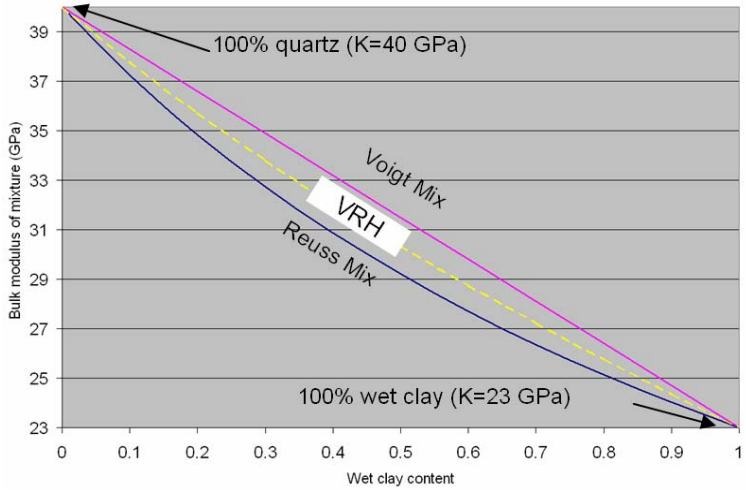


Figure 2.8 Bulk modulus of rock matrix calculated using VRH-average.

## 2.3 Modeling results and discussions

Fluid substitution calculations were carried out in the Cardium sand (from 1605 to 1623 m) of well 102/08-14-48-9W5 by hand. Some of the calculated parameters before fluid substitution are shown in Table 2.1. The fluid substitution was composed of two steps: first, the original pore fluids were replaced by 100% water; then the fluid mixture (90% $CO_2$ and 10% water) replaced the 100% water. The results are shown in Table 2.2, in which we can see that subtle differences are observed in the density, P-wave velocity, and S-wave velocity between $CO_2$ and brine models. The average rock density changed from 2440 kg/m$^3$ to 2380 kg/m$^3$ (about 2.5% decrease) after $CO_2$ replacement; the average P-wave velocity decreases by about 4.62% from 3890 m/s to 3710 m/s; the average S-wave velocity increases by about 1.19% from 2229 m/s to 2255 m/s; the $V_p/V_s$ decreases about 5.66% from 1.745 to 1.645; the P-wave impedance decreases about 5-6%.

The anticipated two-way time shift caused by $CO_2$ injection can be calculated by using the following equation:

$$\Delta t = t_2 - t_1 = \frac{2h}{V_2} - \frac{2h}{V_1} \quad , \qquad (2\text{-}18)$$

where,

$\Delta t$ is the anticipated two-way time shift caused by $CO_2$ injection, h is the net thickness of the Cardium reservoir,

$V_1$ and $V_2$ are the average P-wave velocities of the Cardium reservoir before and after $CO_2$ substitution, respectively,

$t_2$ and $t_1$ are the two-way P-wave travel times of the Cardium reservoir, respectively.

The net thickness (h) of the Cardium reservoir is about 6m. The anticipated two-way P-wave time shift caused by $CO_2$ substitution is about 0.15 ms.

The relationships between velocity change and $CO_2$ saturation under different porosity conditions were studied in more detail (Figures 2.9 and 2.10). In Figure 2.9, a distinct P-wave velocity decrease occurs from 0% $CO_2$ saturation to 50% $CO_2$ saturation. From 50% to 90% $CO_2$ saturation, the P-wave velocity decreases slowly, and from 90% to 100% $CO_2$ saturation, the P-wave velocity increases slightly rather than decreases.

In Figure 2.10, it shows that the S-wave velocity increases almost linearly as the $CO_2$ saturation increases. It is easy to be understood because in the equation: $V_s^{new} = \sqrt{\frac{\mu_{sat}}{\rho_B^{new}}}$, the shear modulus $\mu_{sat}$ doesn't change during the fluid substitution process, while the bulk density decreases gradually as the $CO_2$ saturation increases. However, at the point of 5% $CO_2$ saturation, the S-wave velocity of the 13% porosity sample decreases; from 0 to about 32% $CO_2$ saturation, the S-wave velocity change for 13% porosity is smaller than that for 9% porosity, and possibly is an error caused by assumptions and estimations during the fluid substitution process.

The synthetic seismograms of original fluid, wet, and $CO_2$ models were created in the H-R software package called "AVO" by using the zero-offset ray-tracing method (Figure 2.11). The P-wave wavelet used for the synthetic seismograms is extracted from the baseline P-wave 3D survey and as same as the P-wave wavelet shown in Figure 3.1. Comparing the synthetic seismogram of the $CO_2$ model with that of the wet model, there is almost no change except the reflections around the Cardium sand, where there is a subtle change of the reflections such as the trough between the Cardium Zone and the top of the Cardium sand, which becomes more obvious for the $CO_2$ model than the wet model.

The amplitude differences between the synthetic seismograms for the $CO_2$ and wet models were calculated (Figure 2.12). Around the Cardium sand, there is a relatively strong amplitude difference between the synthetic seismograms. Away from the Cardium sand, the amplitude difference becomes weak. There is almost no obvious amplitude difference between the synthetic seismograms above 1010 ms and below 1110 ms.

| Depth m | Gamma ray API | Before fluid substitution (50% oil, 50% water) | | | | | | | | |
|---|---|---|---|---|---|---|---|---|---|---|
| | | Rock density g/cm$^3$ | $V_p$ m/s | $V_s$ m/s | Clay content % | Density porosity % | $K_{sat}$ Gpa | μ Gpa | $K_o$ GPa | K* Gpa |
| 1611.2 | 31.1 | 2.42 | 3811 | 2254 | 9 | 12.5 | 18.78 | 12.30 | 37.92 | 15.84 |
| 1611.4 | 34.7 | 2.36 | 3724 | 2213 | 13 | 16.2 | 17.43 | 11.53 | 37.03 | 14.93 |
| 1611.6 | 56.5 | 2.39 | 3684 | 2188 | 37 | 13.5 | 17.19 | 11.44 | 31.80 | 14.83 |
| 1611.8 | 62.0 | 2.43 | 3674 | 2182 | 43 | 11.3 | 17.33 | 11.55 | 30.77 | 14.71 |
| 1612 | 61.5 | 2.44 | 3692 | 2192 | 42 | 10.6 | 17.62 | 11.71 | 30.91 | 14.89 |
| 1612.2 | 50.1 | 2.43 | 3734 | 2214 | 30 | 11.2 | 18.03 | 11.93 | 33.29 | 15.15 |
| 1612.4 | 43.6 | 2.42 | 3790 | 2243 | 23 | 12.3 | 18.52 | 12.17 | 34.75 | 15.86 |
| 1612.6 | 40.0 | 2.40 | 3817 | 2257 | 19 | 13.3 | 18.69 | 12.24 | 35.61 | 16.18 |
| 1612.8 | 42.9 | 2.42 | 3850 | 2274 | 22 | 12.3 | 19.17 | 12.50 | 34.91 | 16.71 |
| 1613 | 47.8 | 2.44 | 3885 | 2292 | 27 | 10.8 | 19.75 | 12.83 | 33.81 | 17.33 |
| 1613.2 | 53.6 | 2.46 | 3900 | 2300 | 34 | 9.4 | 20.09 | 13.03 | 32.61 | 17.67 |
| Average | 47.6 | 2.42 | 3778 | 2237 | 27 | 12.1 | 18.42 | 12.11 | 33.95 | 15.83 |

Table 2.1 Parameters before fluid substitution of well 102/08-14-48-9W5.

| Depth m | After fluid substitution (100% water) | | | | | | | After fluid substitution (10% water, 90% $CO_2$) | | | | | | |
|---|---|---|---|---|---|---|---|---|---|---|---|---|---|---|
| | Rock density g/cm$^3$ | $K_{sat}$ GPa | $V_p$ m/s | $V_s$ m/s | $V_p$ change % | $V_s$ change % | Vp/Vs change % | Rock density g/cm$^3$ | $K_{sat}$ GPa | $V_p$ m/s | $V_s$ m/s | $V_p$ change % | $V_s$ change % | Vp/Vs change % |
| 1611.2 | 2.44 | 21.46 | 3938 | 2245 | 3.35 | -0.38 | 3.75 | 2.38 | 16.76 | 3731 | 2273 | -5.26 | 1.25 | -6.10 |
| 1611.4 | 2.38 | 19.83 | 3847 | 2202 | 3.07 | -0.50 | 3.58 | 2.3 | 15.70 | 3673 | 2238 | -4.52 | 1.64 | -5.74 |
| 1611.6 | 2.41 | 19.34 | 3789 | 2179 | 2.84 | -0.41 | 3.26 | 2.35 | 15.57 | 3624 | 2208 | -4.35 | 1.34 | -5.62 |
| 1611.8 | 2.44 | 19.60 | 3786 | 2175 | 3.06 | -0.34 | 3.41 | 2.39 | 15.55 | 3599 | 2198 | -4.94 | 1.06 | -6.10 |
| 1612 | 2.45 | 19.95 | 3808 | 2185 | 3.12 | -0.31 | 3.45 | 2.4 | 15.76 | 3613 | 2207 | -5.12 | 1.01 | -6.21 |
| 1612.2 | 2.45 | 20.54 | 3857 | 2206 | 3.29 | -0.33 | 3.63 | 2.4 | 16.07 | 3651 | 2230 | -5.34 | 1.10 | -6.28 |
| 1612.4 | 2.44 | 20.92 | 3904 | 2234 | 3.02 | -0.37 | 3.40 | 2.38 | 16.69 | 3719 | 2261 | -4.74 | 1.21 | -5.72 |
| 1612.6 | 2.42 | 21.01 | 3926 | 2248 | 2.85 | -0.40 | 3.26 | 2.36 | 16.96 | 3755 | 2277 | -4.36 | 1.31 | -5.39 |
| 1612.8 | 2.44 | 21.42 | 3954 | 2265 | 2.71 | -0.37 | 3.09 | 2.38 | 17.48 | 3789 | 2292 | -4.17 | 1.19 | -5.18 |
| 1613 | 2.46 | 21.92 | 3985 | 2285 | 2.56 | -0.32 | 2.89 | 2.41 | 18.10 | 3824 | 2309 | -4.04 | 1.05 | -5.00 |
| 1613.2 | 2.48 | 22.19 | 3996 | 2294 | 2.47 | -0.28 | 2.76 | 2.43 | 18.44 | 3836 | 2314 | -4.00 | 0.88 | -4.94 |
| Average | 2.44 | 20.74 | 3890 | 2229 | 2.94 | -0.36 | 3.32 | 2.38 | 16.64 | 3710 | 2255 | -4.62 | 1.19 | -5.66 |

Table 2.2 Results after fluid substitution of well 102/08-14-48-9W5.

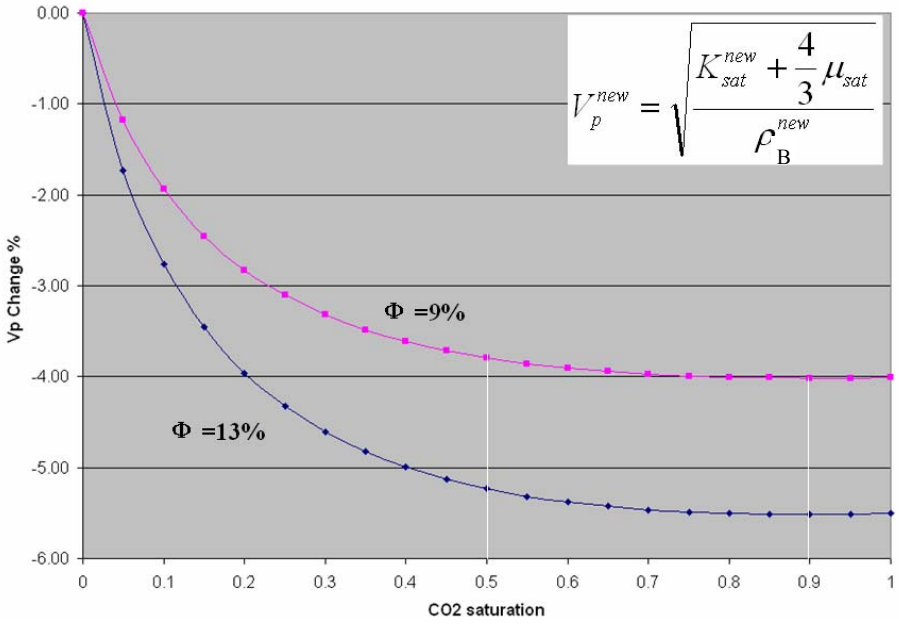


Figure 2.9 Change in Vp versus $CO_2$ saturation for a $CO_2$-water system (Φ is porosity).

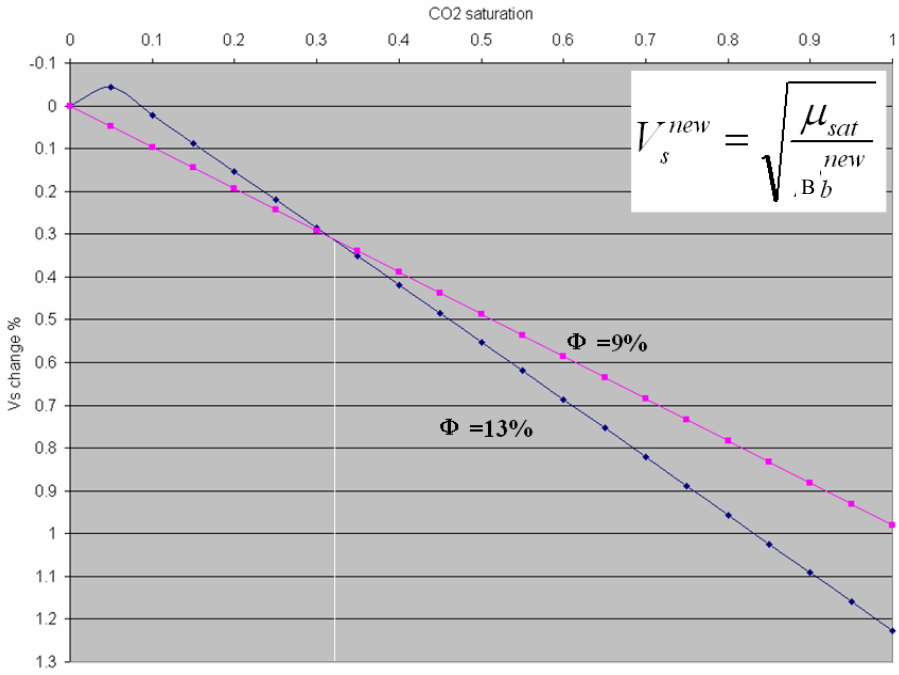


Figure 2.10 Change in $V_s$ versus $CO_2$ saturation for a $CO_2$-water system (Φ is porosity).

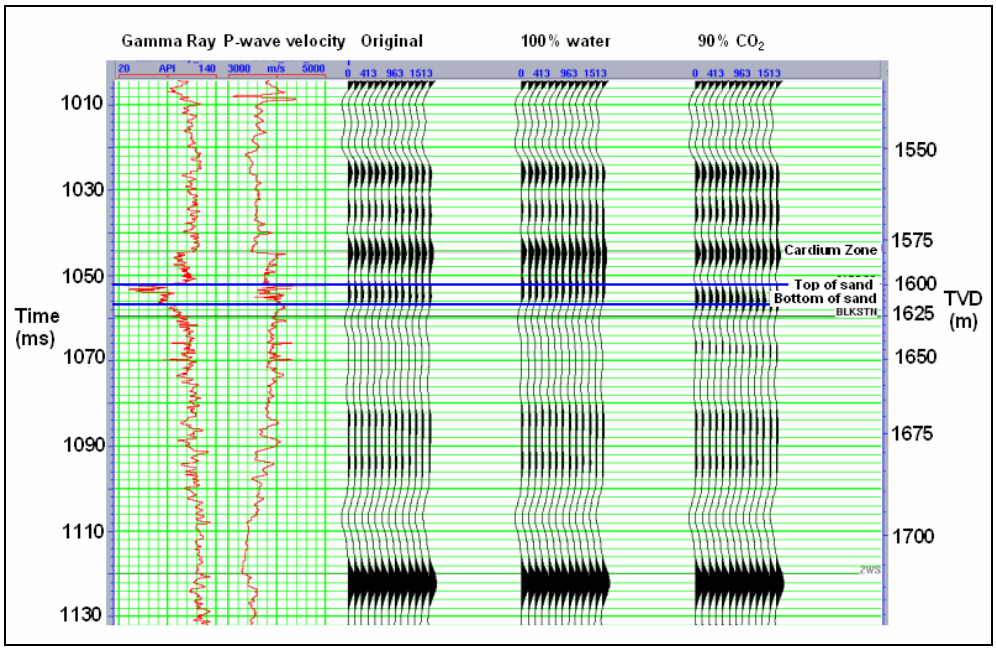


Figure 2.11 Synthetic seismograms before and after fluid substitutions of well 102/08-14-9W5.

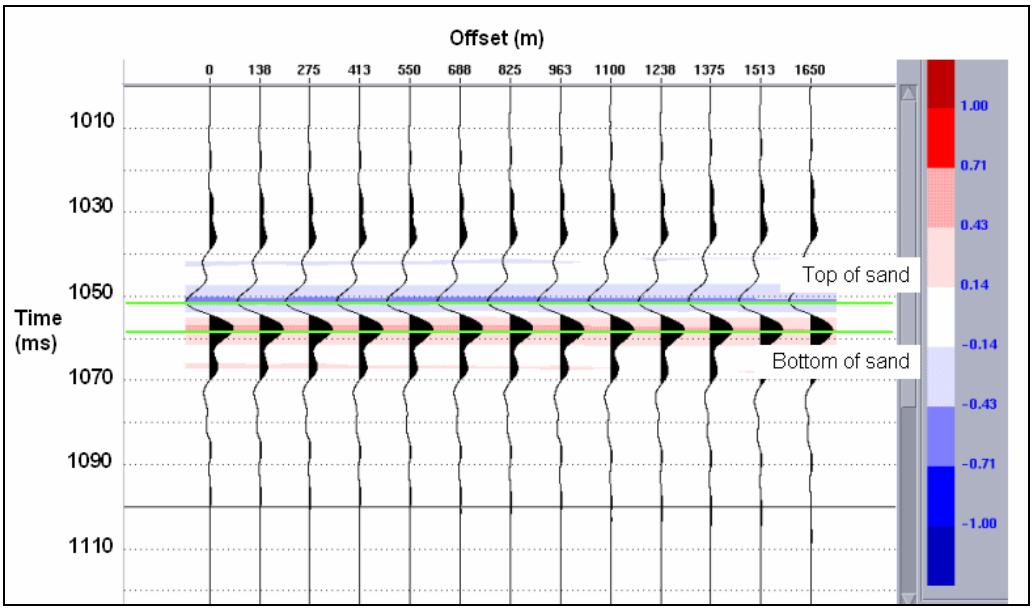


Figure 2.12 Amplitude differences between the synthetic seismograms for the $CO_2$ and wet models of well 102/08-14-48-9W5 (colours represent the normalized amplitude differences).

Assumptions and estimations were made during the fluid substitution processes that require some discussion. First, a direct result of using the Gassmann's equation is that the shear modulus for an isotropic material is independent of pore fluids, and therefore remains constant during the fluid substitution process (Smith, 2003). However, if the pores are disconnected or cracks exist in the reservoir, this assumption may be violated. Second, there exists some chert in the rock matrix in he Cardium reservoir, but the exact amount and properties of chert are unknown, and the error caused by neglecting it is also unknown. An equilibrium saturation model was used in the fluid substitution process; however, the equilibrium distribution of fluids may be disturbed during the $CO_2$ injection. Thus it might be more realistic to use a "patchy saturation" model than an "equilibrium saturation" model. Castagna and Hooper (2000) studied the difference between patchy and equilibrium saturation models and concluded that for low-porosity sand, the difference between patchy and equilibrium saturation is less than 5% (Smith, 2003). The effect of pressure and temperature changes in the reservoir was also not considered.

### 2.4 Chapter summary

Gassmann modeling is an effective method to model the 4D differences, which are caused by $CO_2$ injection. A distinct P-wave velocity decrease occurs from 0% to 50% $CO_2$ saturation; but from 50% to 90% $CO_2$ saturation, the P-wave velocity decreases only

slowly. The P-wave velocity decreases about 5% and the S-wave velocity increases about 1% after 90% $CO_2$ substitution, and the total time-shift caused by the injected $CO_2$ for PP seismic is less than 1 ms. Assuming that the P-wave impedance of shales above and below the Cardium reservoir does not change, a modest amplitude change (around 30% decrease) will be generated around the Cardium reservoir by the $CO_2$ injection.

# CHAPTER 3: SEISMIC INTERPRETATION

## 3.1 Synthetic seismograms

A dipole sonic log was available from well 102/07-11-48-9W5 (Figure 1.8), which penetrated the top of the Blackstone Formation underlying the Cardium Formation. The PP and PS wavelets were extracted from the baseline PP and PS 3D seismic data for the interval between Ardley and Viking events, using both the available well and seismic data, which has the ability to extract the actual wavelet phase, in ProMC of H-R software package (Figure 3.1); both the PP and PS wavelets have a zero phase, and their dominant frequencies are about 26-36 Hz and 18-28 Hz, respectively. PP and PS synthetic seismograms at well 102/07-11-48-9W5 were generated (Figure 3.2). The synthetic seismograms match the surface seismic data quite well. The top of the Cardium sand correlates to a weak peak at approximately 1043 ms and 1690 ms in the PP and PS survey, respectively; the top of Blackstone Formation correlates to a weak trough at approximately 1060ms and 1714 ms in the PP and PS survey, respectively. In order to correlate the PP and PS data well, the strong peak at 360ms and 685ms in PP and PS data, respectively, which correlates to the depth at approximately 440m at the well location, was picked. This reflection is from the Ardley Coal Zone.

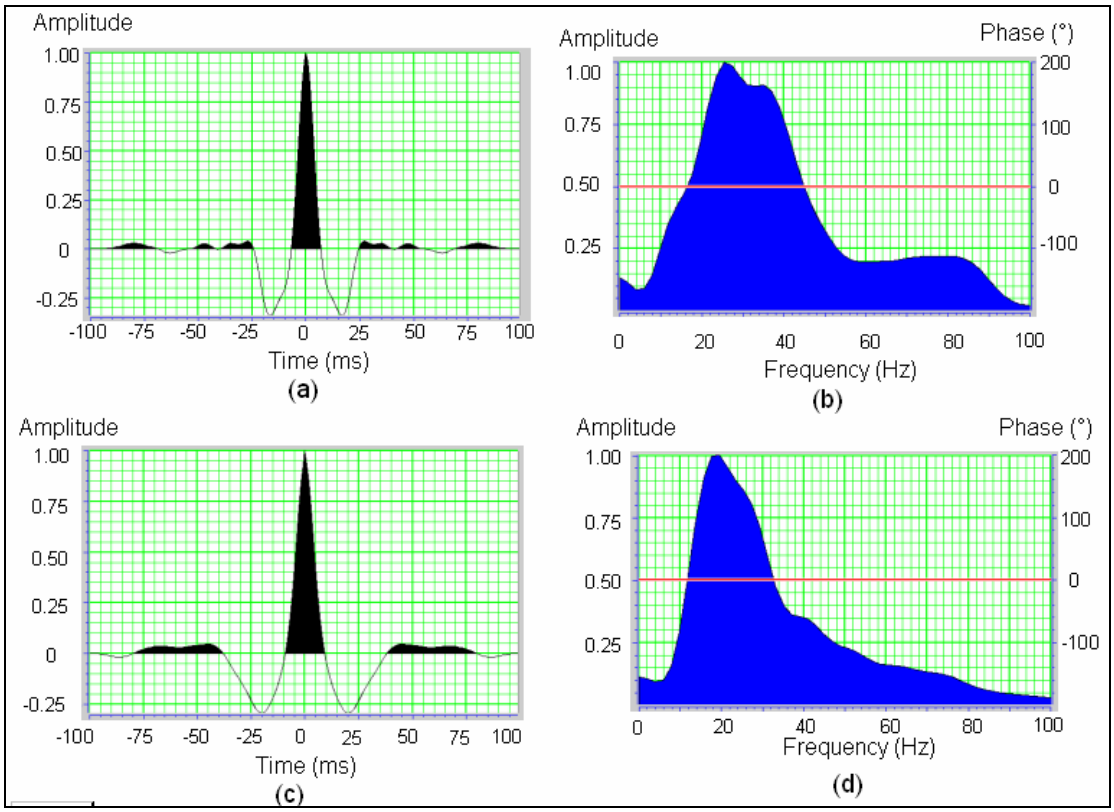


Figure 3.1 (a) PP wavelet in time domain; (b) PP wavelet in frequency domain; (c) PS wavelet in time domain; (d) PS wavelet in frequency domain.

In order to correlate the deep formations with the seismic events, well 102/08-14-48-9W5, which has P-wave sonic log and penetrates the top of Paleozoic Banff Formation, was projected into the 3D survey. The synthetic seismogram ties the seismic data very well, and the horizons of the Cardium and Blackstone picks defined by the synthetic seismogram of this well match very well with the horizons identified from well 102/07-11-48-9W5 (Figure 3.3). The top of the Viking Formation correlates to a strong peak at approximately 1232 ms in PP data; for PS data, the top of the Viking Formation also correlates to a strong peak at approximately 1950 ms, which was defined by

comparing the reflection character of the PP and PS data. Figure 3.4 shows the un-stretched, un-squeezed PP seismic and synthetic seismogram and the squeezed PS seismic and synthetic seismogram used to correlate the PP and PS datasets.

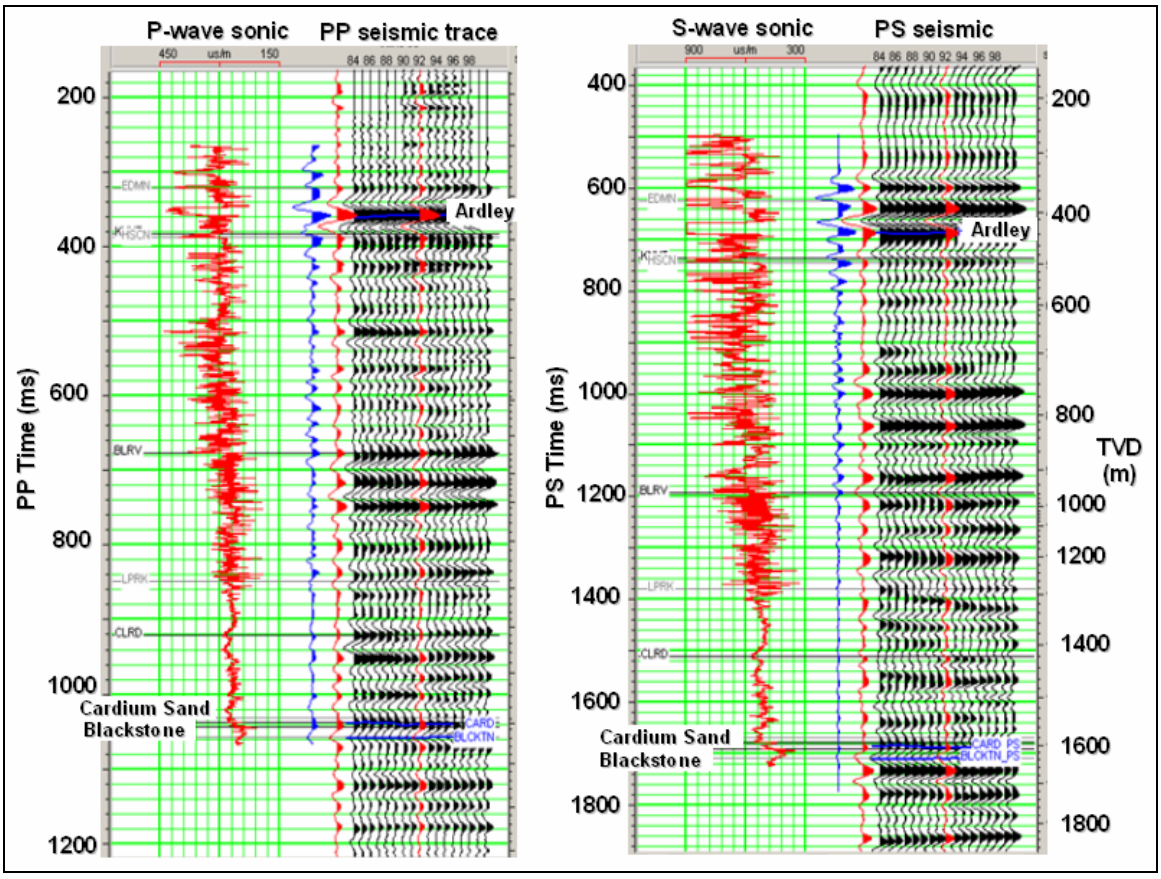


Figure 3.2 PP (left) and PS (right) seismic correlations at well 102/07-11-48-9W5. The blue trace is synthetic seismogram, the red trace is the seismic trace extracted from the seismic data at the well location.

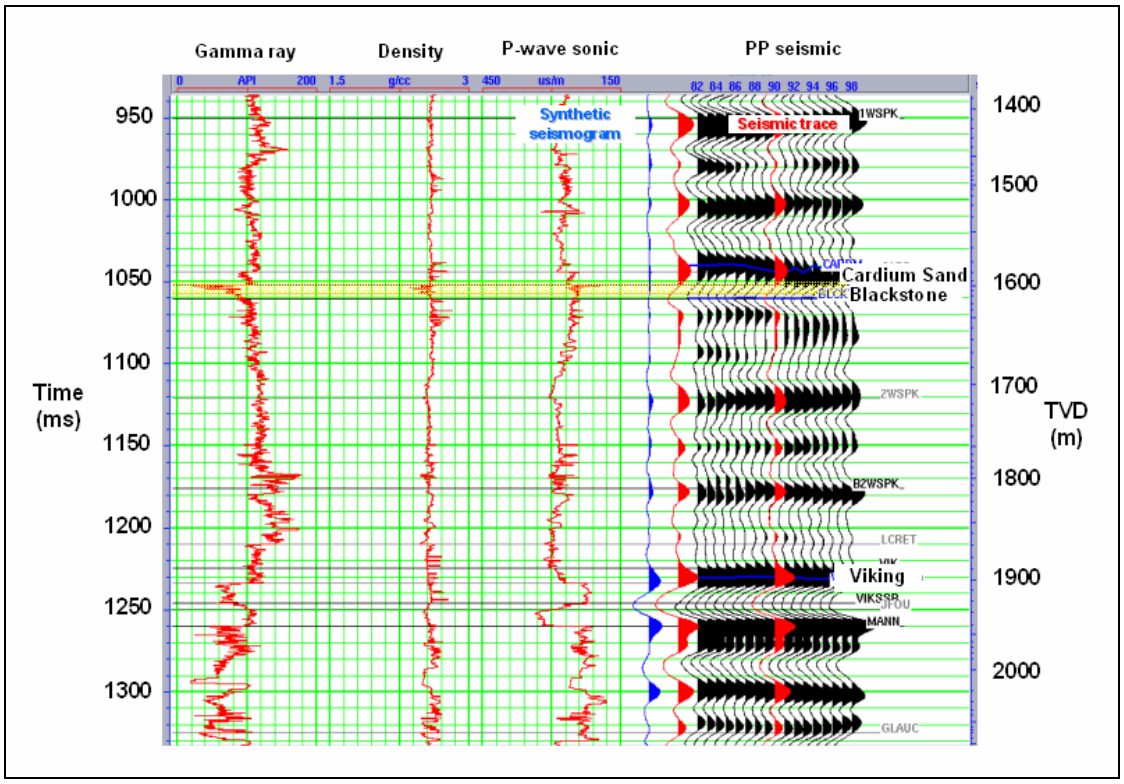


Figure 3.3 PP seismic correlation at well 102/08-14-48-9W5 with picked horizons. The blue trace is the synthetic seismogram; the red trace is the seismic trace extracted from the seismic data at the well location.

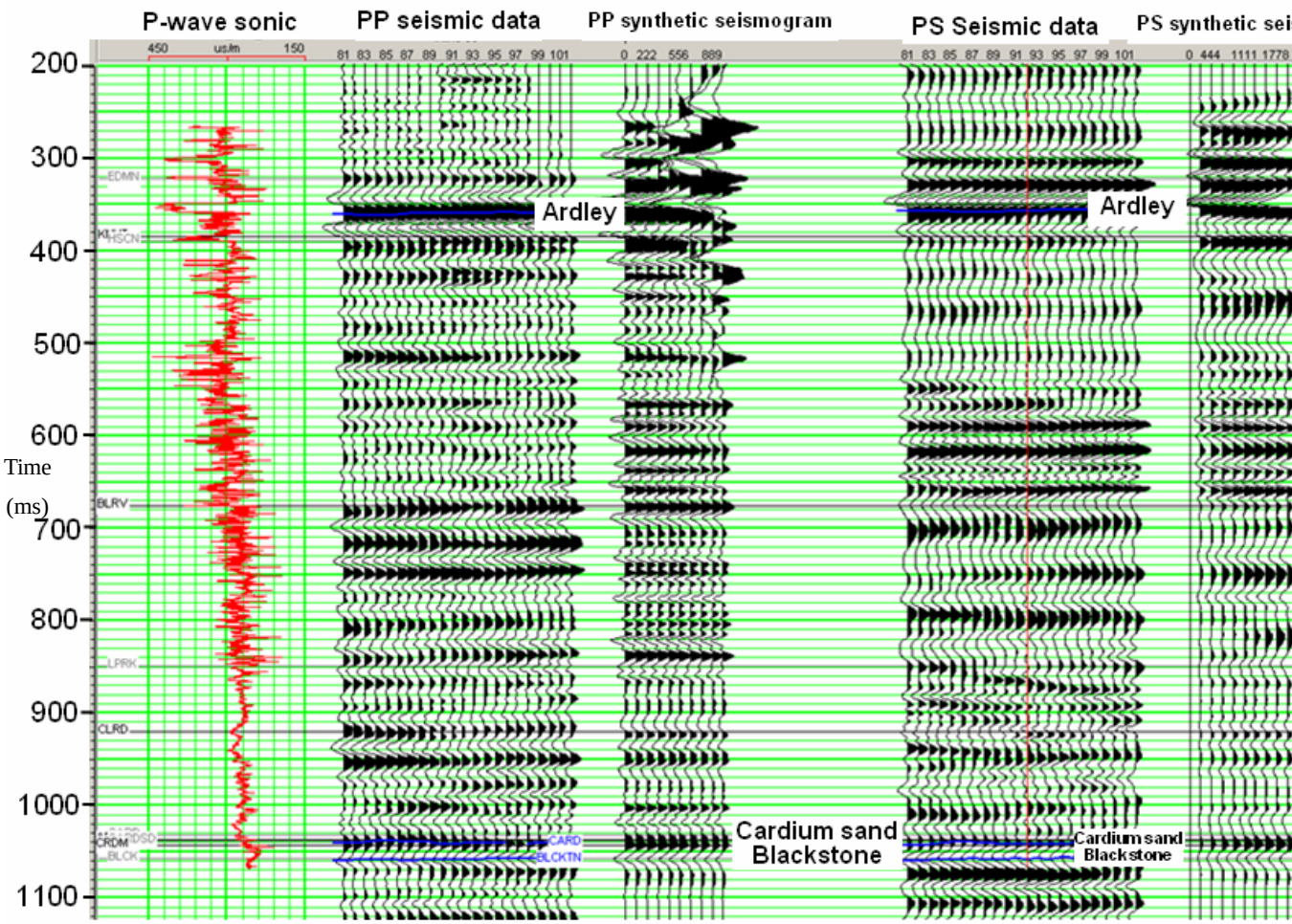


Figure 3.4 PP and PS seismic and synthetic seismograms of well 102/07-11-48-9W5 shown in PP time.

Several horizons such as Ardley, Cardium Sand, and Viking, were picked in the PP and PS baseline and monitor seismic surveys, respectively (Figures 3.5, 3.6, 3.7 and 3.8). The quality of PP data is good; the PS data is noisy and polluted by artifacts. All the horizons are flat in the PP and PS data, and there are no obvious faults in this area. The baseline PP and PS time structural maps of the Viking pick are shown in Figure 3.9 and Figure 3.10, respectively.

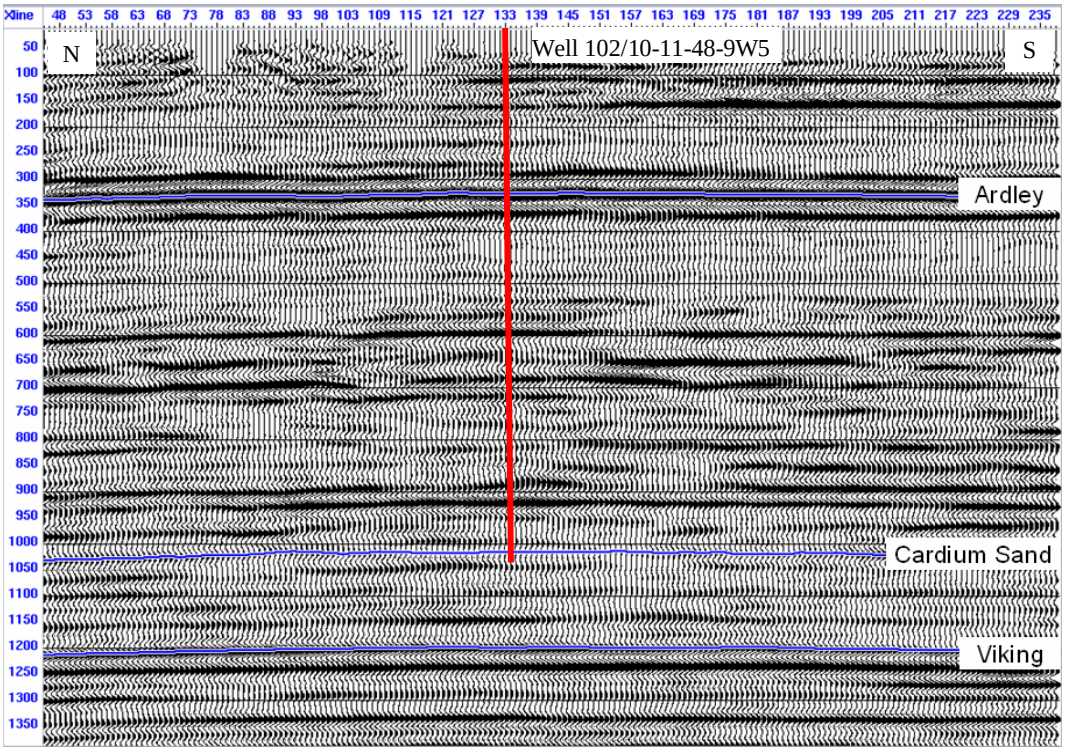


Figure 3.5 PP seismic section of line 1 (baseline survey).

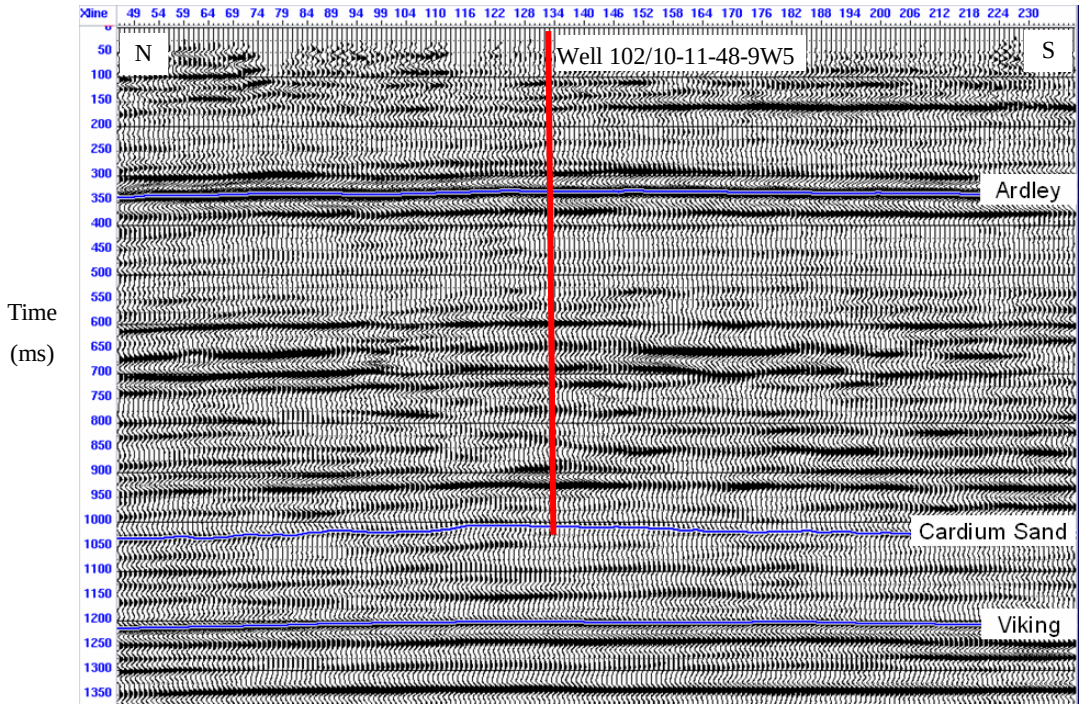


Figure 3.6 PP seismic section of line 1 (monitor survey).

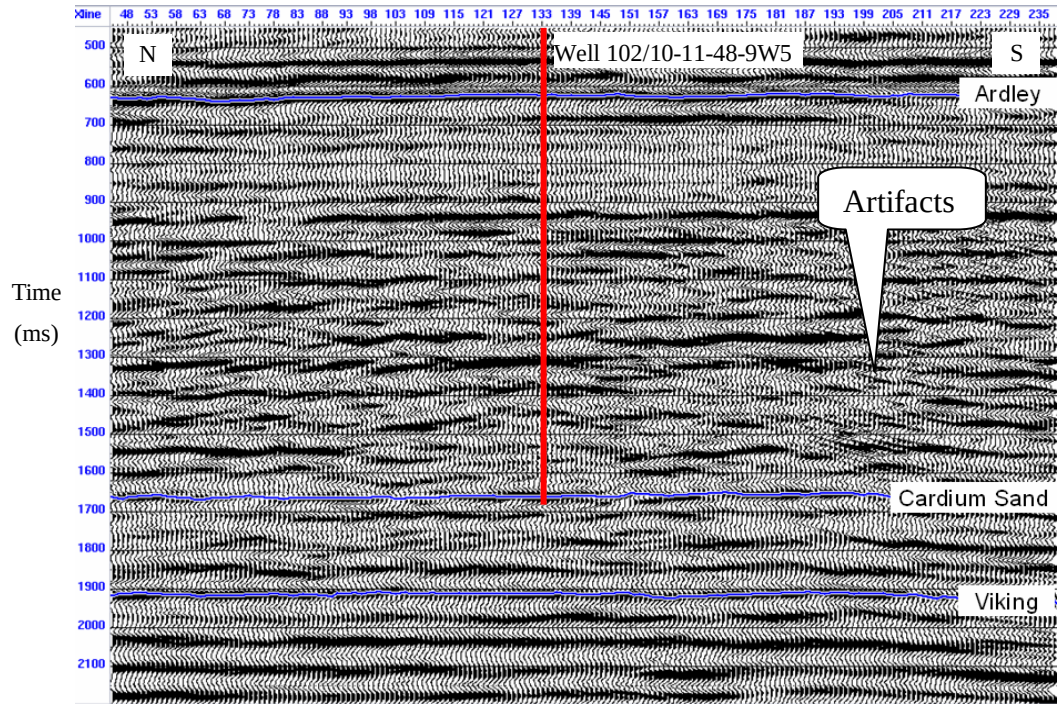


Figure 3.7 PS seismic section of line 1 (baseline survey).

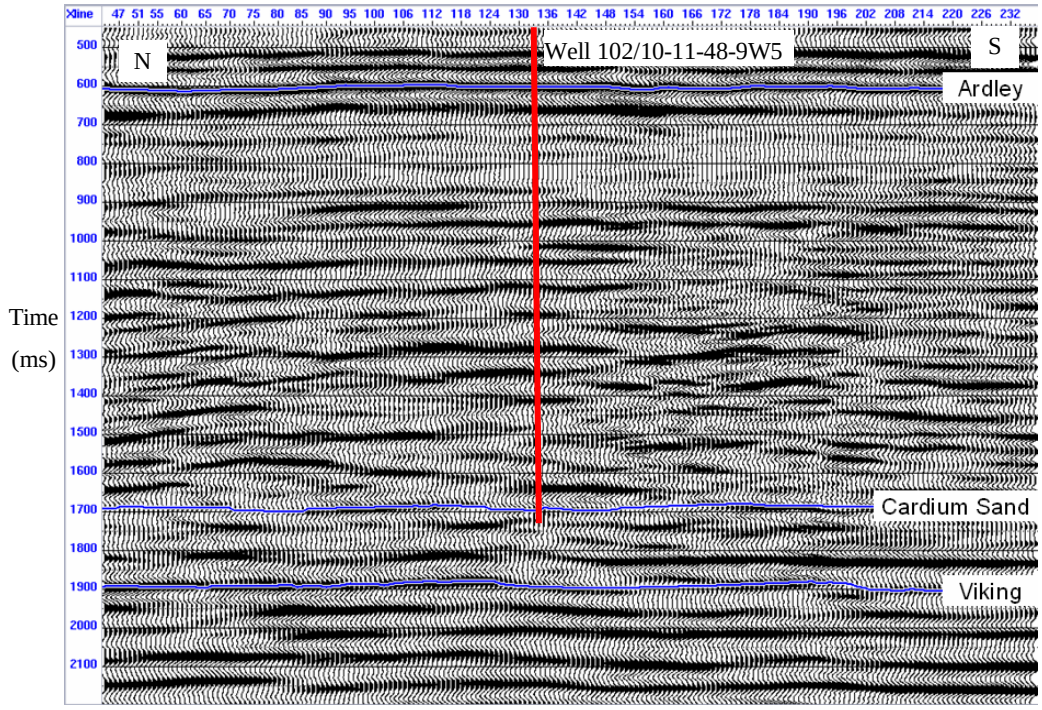


Figure 3.8 PS seismic section of line 1 (monitor survey).

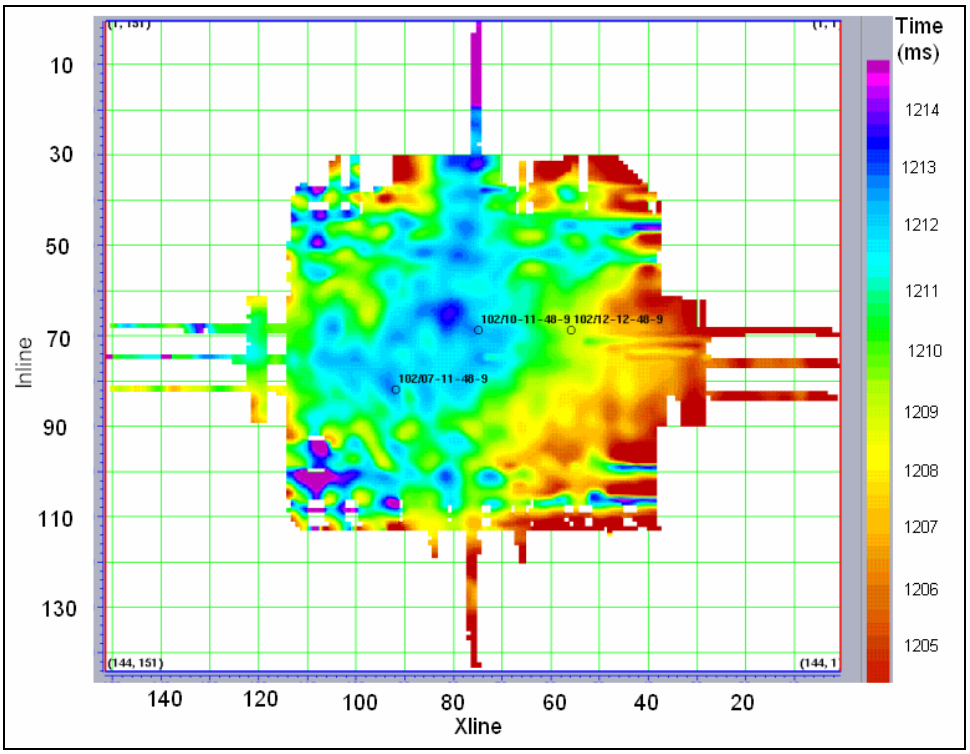


Figure 3.9 PP time structural map of Viking (baseline survey).

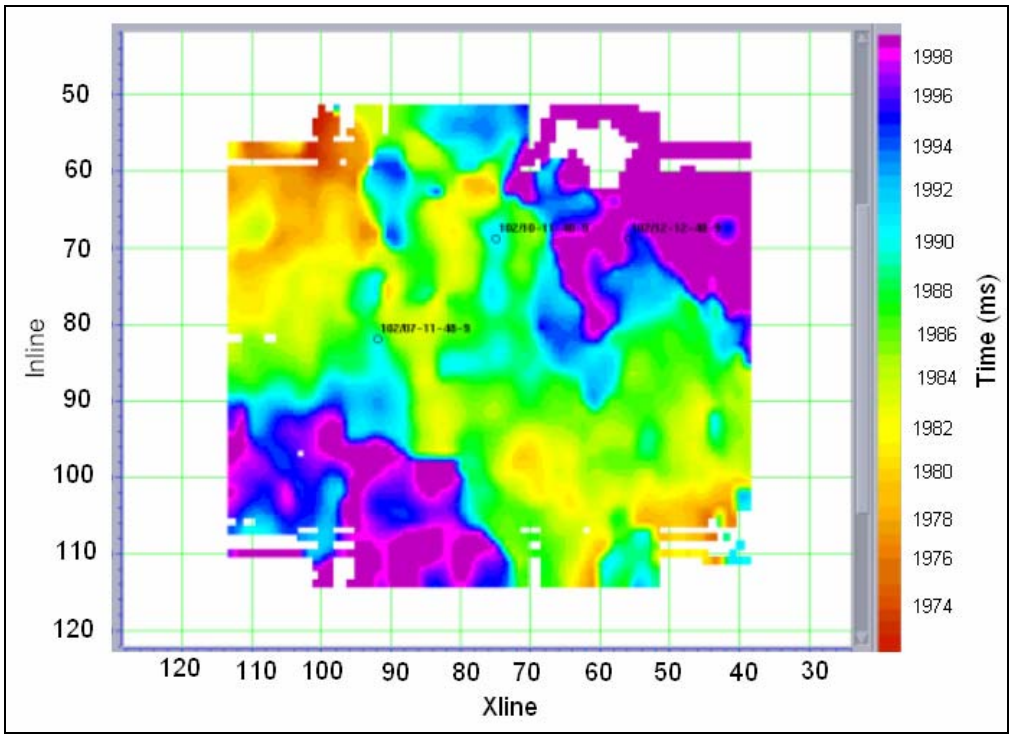


Figure 3.10 PS time structural map of Viking (baseline survey).

### 3.2 Seismic data calibration

The sensitivity and success of 4D monitoring depend on measuring small changes in the earth's response that result from $CO_2$ injection. Therefore, all other changes which are unrelated to $CO_2$ injection must be suppressed as much as possible. Even though the baseline and monitor datasets have the same acquisition geometry and are processed by using the same flows and parameters, there are still some systematic differences between them, which are unrelated with the $CO_2$ injection. For example, in Figure 3.11, we can see that significant difference energy (bright spots) occur in the data from line 1 before calibration.

In Hampson-Russell, one way to calculate the difference between two seismic sections or volumes (A-B) is to calculate a simple difference between the two volumes on a sample-by sample basis. The amplitude differences are usually shown in colours. The default colour range is "mean $\pm$2*standard_deviation" and within 5% of maximum range. For example, if the mean and deviation values of amplitude difference are –0.000412762 and 1.04645, respectively, then the default colour range of amplitude difference is from –2.0933 to 2.09248 (it is usually normalized from –1 to 1).

For the surveys, a cross correlation was run in a single window from 450ms to 950ms, assuming no $CO_2$-injection effect in this window, and a maximum allowable time shift was set at 5 ms. The correlation slice indicates that with no calibration of the monitor dataset, the correlation coefficients between the monitor and baseline surveys range from 0.23-0.96 (Figure 3.12). The correlation time shift slice shows that there is an average bulk shift of 4-5 ms between these two datasets, which is probably caused by changes in the weathering layer between the recorded times of baseline and monitor surveys, and is unrelated to the $CO_2$ injection (Figure 3.13). Therefore, calibration must be applied to the monitor survey prior to doing any 4D analysis.

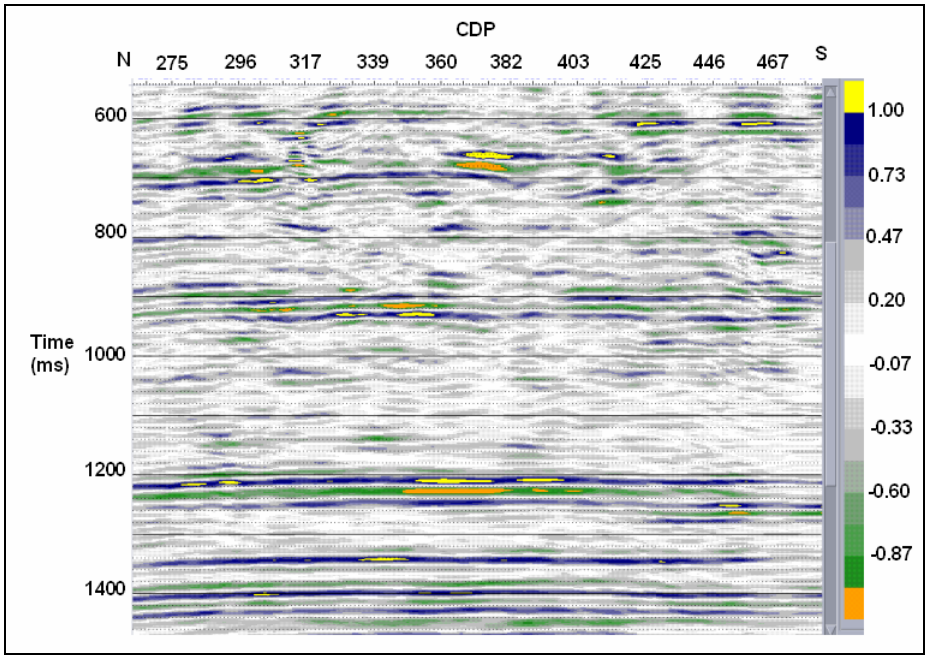


Figure 3.11 PP amplitude differences between monitor and baseline surveys before calibration of line 1 (monitor-baseline, the colours represent normalized amplitude differences).

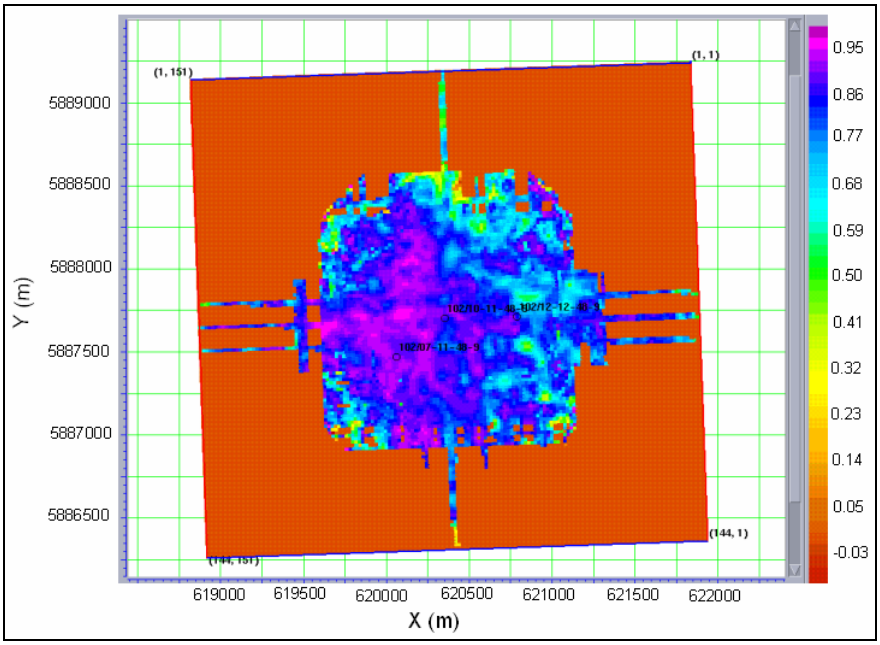


Figure 3.12 Maximum cross correlation between the PP monitor and baseline surveys (450-950ms, before calibration). The colors represent correlation coefficients.

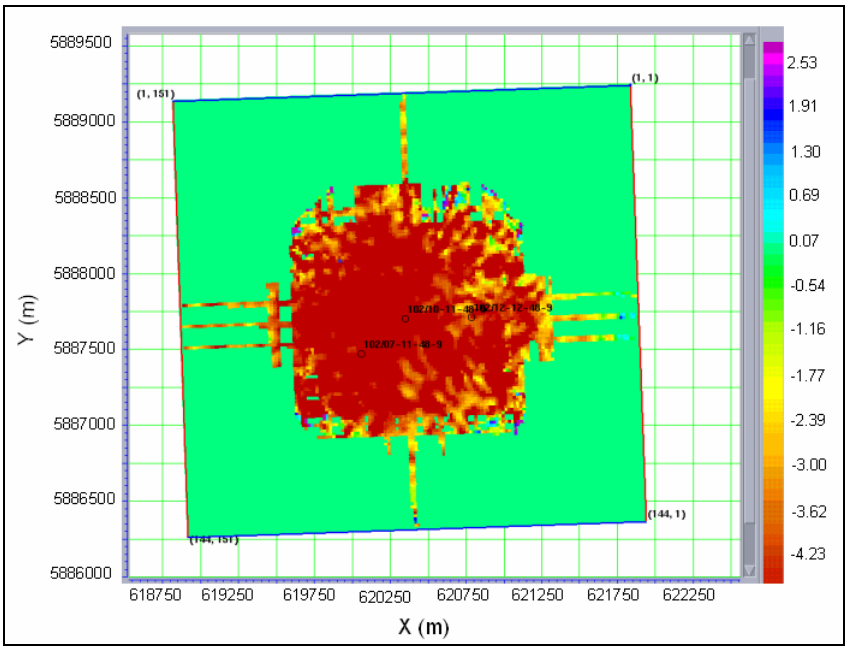


Figure 3.13 Cross correlation time shift between the PP monitor and baseline surveys (450-950ms, before calibration).

Three steps of calibration were applied to the monitor survey using Pro4D software. They are phase and time matching, application of a shaping filter, and cross normalization. The phase and time matching process computes the time and phase shifts between the baseline and monitor surveys and applies them to the monitor dataset. Then the shaping filter process shapes traces from the monitor volume to match the traces of the baseline volume using the Wiener-Levinson approach (Hampson-Russell, 2001). Finally, the cross normalization process compares the RMS amplitudes of traces in the two volumes, and then calculates and applies a gain factor to the monitor volume.

There are several critical parameters during the three steps of calibration processes: the reference volume, the calibration window location and length, and the

processing mode. Throughout the entire procedure of calibration, the baseline dataset is always set as the reference volume and does not change from beginning to the end; the monitor dataset is updated as the various processes are applied to the monitor data. It is important to leave the entire possible $CO_2$-affected zone out of the processing window during data calibration so that the $CO_2$-injection effects will not be affected in the final differencing. Our zone of interest is below 1000 ms so these times were left out of the calibration window. On the other hand, the shallow part of the datasets should also be excluded from the calibration window because there is too much noise in the shallow (early) part of the datasets. The calibration window length affects the shaping filter and a window length on the order of 0.5 sec is normally quite satisfactory (Robinson, 1972). Based on the above discussion, the calibration window was set from 450 ms to 950 ms. Three processing modes are available in Hampson-Russell: trace-by-trace, running average, and global average. The trace-by-trace processing mode was used during the entire procedure of calibration.

The calibration results for every calibration step for line 1 are shown in Figure 3.14. After phase and time matching and application of the shaping filter, most of the bright amplitude areas have disappeared on the difference section (Figure 3.14b and Figure 3.14c), which means the monitor survey matches the baseline survey better than without calibration; there is almost no more obvious improvement after cross

normalization (Figure 3.14d). For the 3D survey volume, the significant improvement in correlation is also obvious after calibration: the range of the correlation coefficients of the data window is from about 0.66 to 0.99 (Figure 3.15). The correlation time shift slice shows that, after calibration, there is only ±0.13-0.15 ms bulk shift left between the monitor and baseline datasets in the window from 450ms to 950ms (Figure 3.16). The monitor dataset after calibration was used to do all the subsequent 4D analysis.

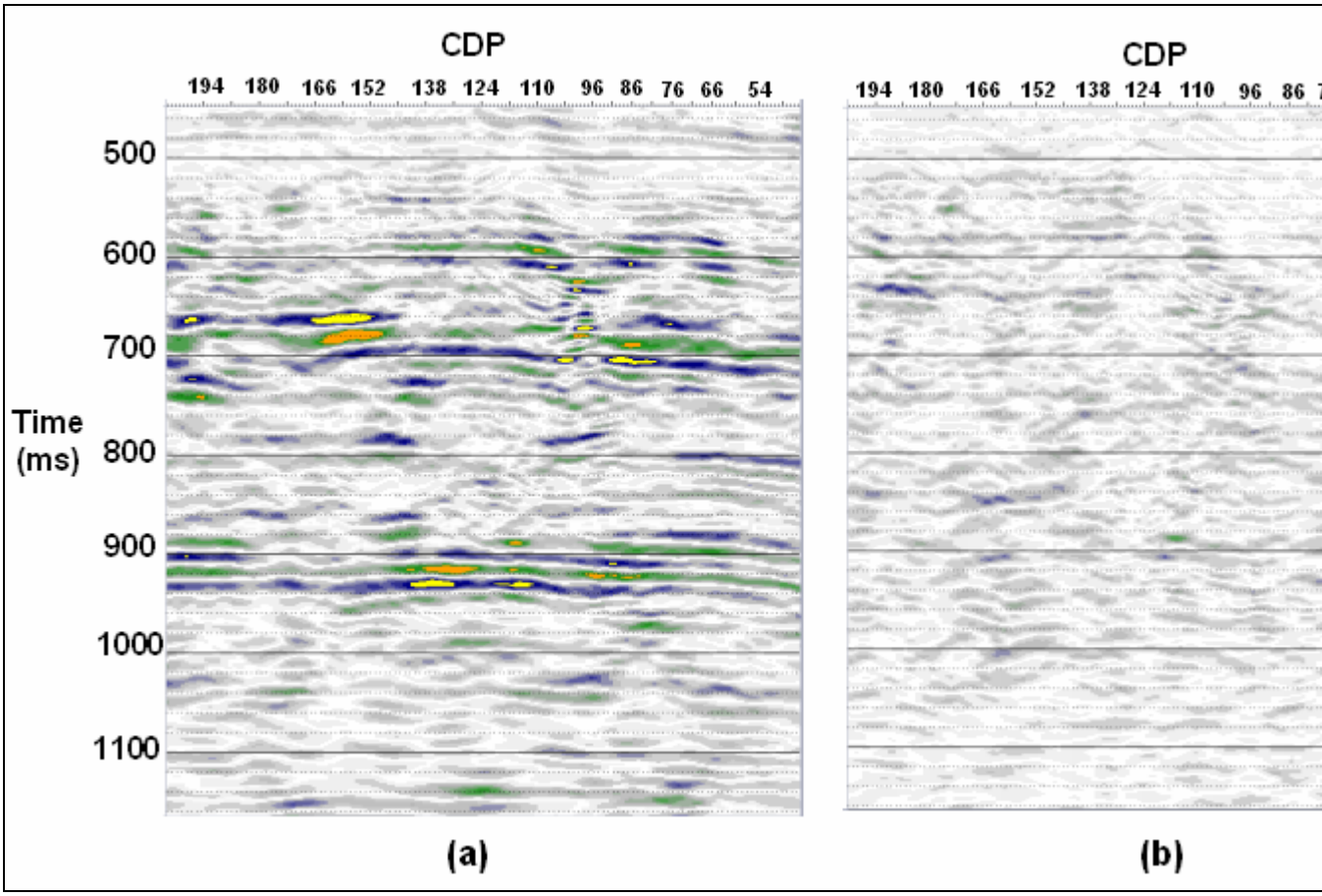


Figure 3.14 PP amplitude differences between monitor and baseline surveys of Line 1 (monitor-baseline): (a) difference before any calibration; (b) difference after phase and time matching. The colours represent normalized amplitude differences

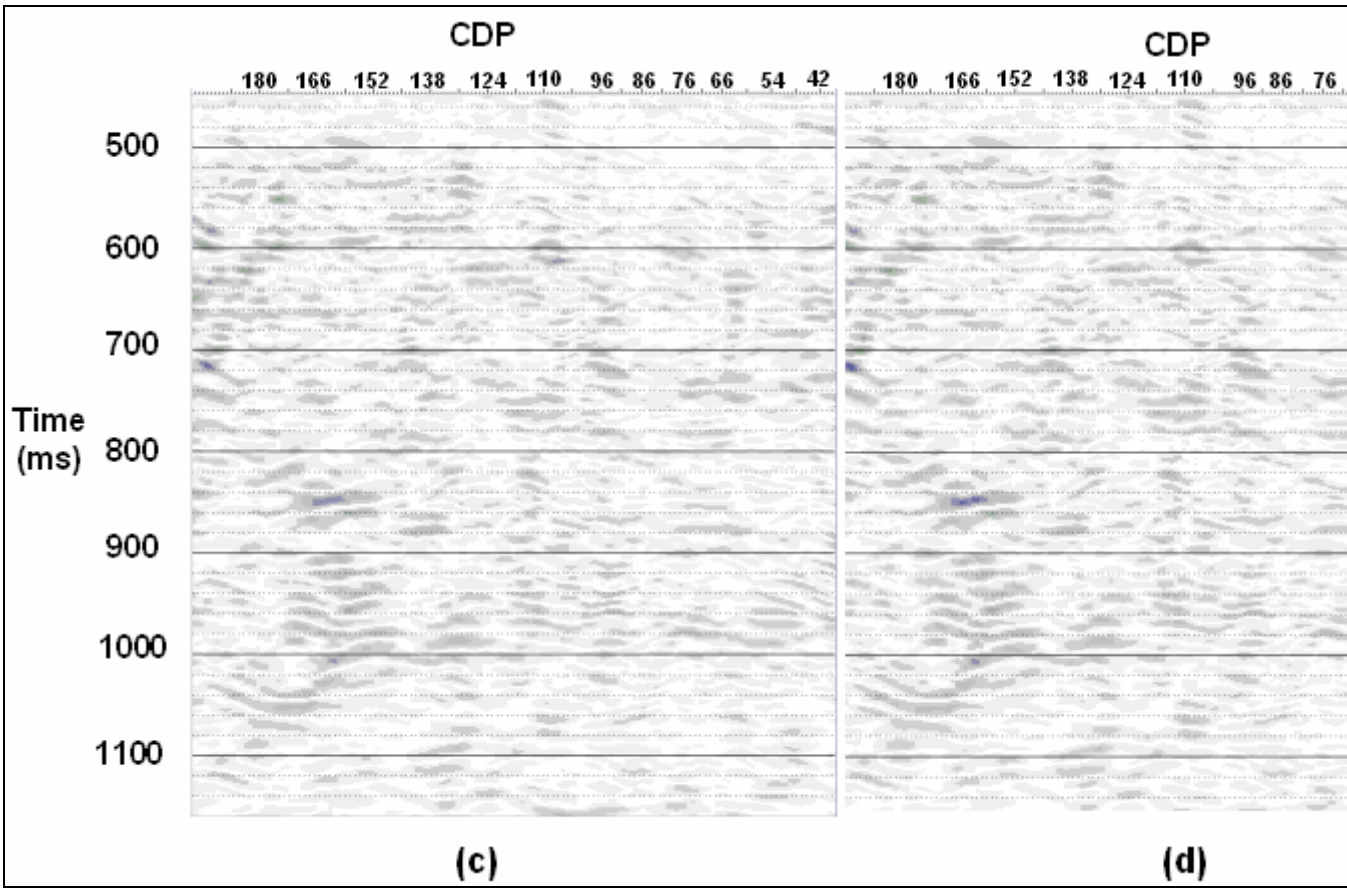


Figure 3.14 PP amplitude differences between monitor and baseline surveys of Line 1 (monitor-baseline): (c) difference after phase & time matching and shaping filter; (d) difference after phase & time matching, shaping filter, and cross normalization. The colours represent normalized amplitude differences

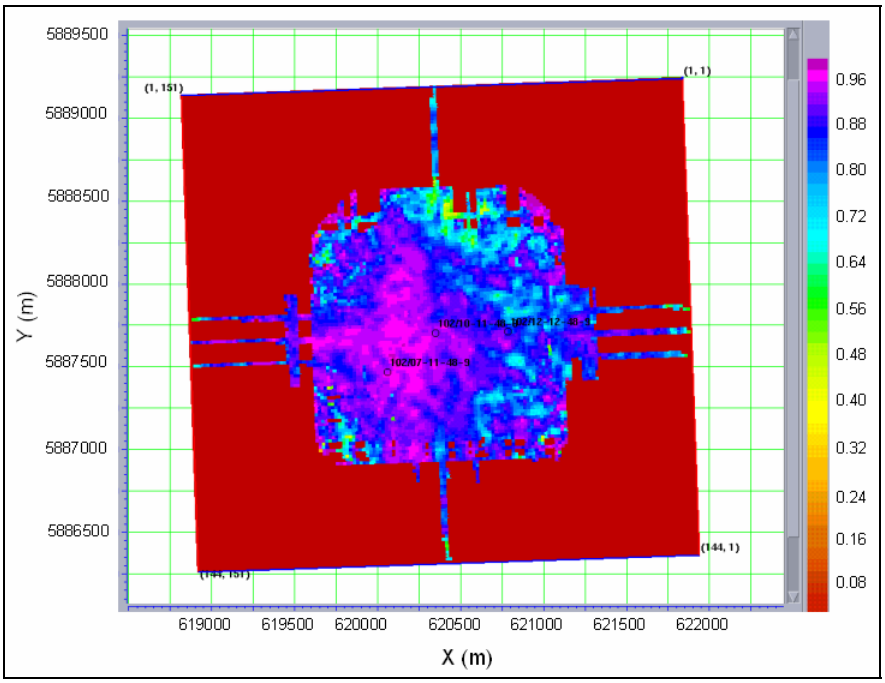


Figure 3.15 Maximum cross correlation between the PP monitor and baseline surveys (450-950ms, after calibration). The colours represent correlation coefficients.

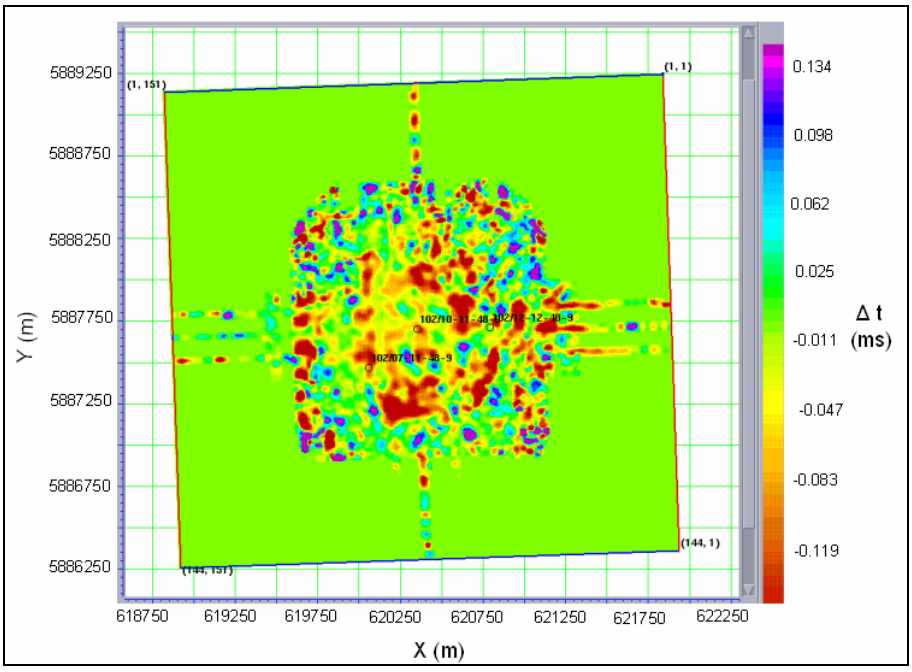


Figure 3.16 Cross correlation time shift between the PP monitor and baseline surveys (450-950ms, after calibration).

## 3.3 PP and PS data interpretation

### *3.3.1 Time shift*

Based on the fluid substitution model, the P-wave velocity of the Cardium sand should decrease approximately 4-5% after $CO_2$ injection, which means there would be approximately 0.15 ms time shift between the baseline and monitor surveys that is corresponding to $CO_2$ effect (the time shift is estimated based on the thickness of good Cardium sand is approximately 6 m). Therefore, time shift may be a possible $CO_2$ indicator. The time shifts at the Cardium reservoir (1030-1060ms) and at the Viking level (1200-1230ms) were measured after calibration (Figure 3.17 and Figure 3.18). The time shift does not need to be an integral number of samples, because the time shift is performed in the frequency domain. The time shifts around the observation well and the $CO_2$ injection wells are very small and there are no time-shift anomalies could be detected. However, around the edge parts of the survey, the time shifts are as much as more than 2 ms, which are caused by low fold rather than by changes in the reservoir. In conclusion, time shift is not an effective $CO_2$ indicator for the first monitor survey at the Violet Grove area.

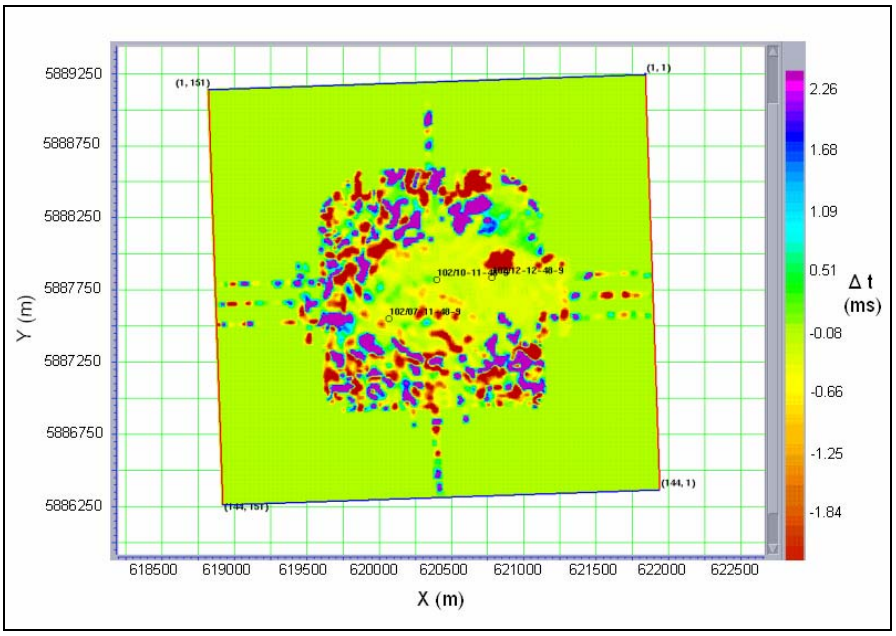


Figure 3.17 Time shift between the PP monitor and baseline surveys (1030-1060ms, after calibration).

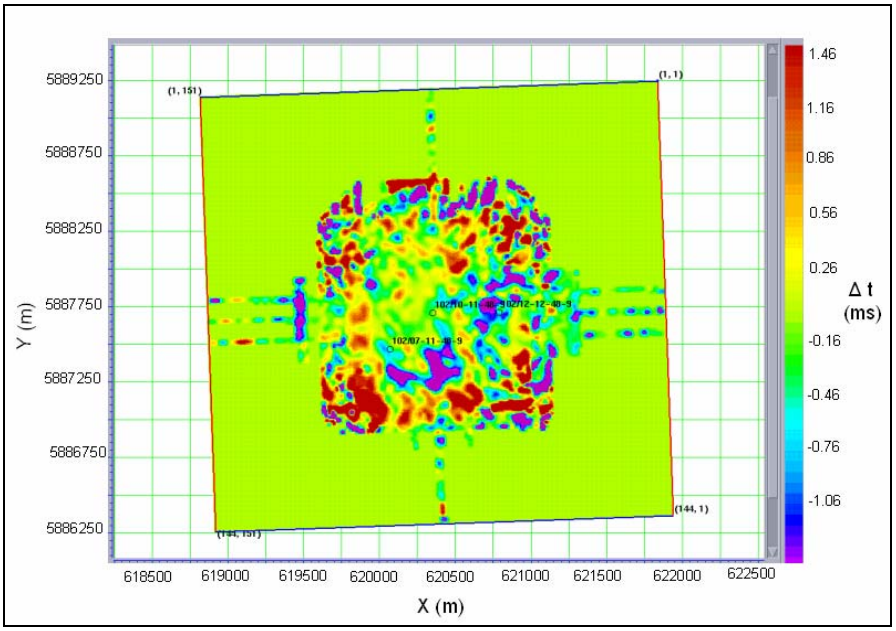


Figure 3.18 Time shift between the PP monitor and baseline surveys (1200-1230ms, after calibration).

*3.3.2 Amplitude changes*

Amplitude changes of the Cardium reflection between the baseline and monitor surveys is another possible indicator to highlight the reflectivity changes caused by the $CO_2$ injection. However, there is no identifiable amplitude anomaly around the $CO_2$ injection points after calibration between baseline and monitor surveys for Line 1 (Figure 3.19). For Line 2 and 3, there are some amplitude differences between monitor and baseline surveys, but it seems that these differences were caused by noise rather than $CO_2$ injection (Figures 3.20 and 3.21). For the 3D survey, the RMS amplitude differences around the Cardium and Viking between the monitor and baseline surveys were extracted (Figure 3.22 and Figure 3.23). The character of the amplitude changes is similar to the time shift map: there are no obvious amplitude changes around the $CO_2$ injection wells. In conclusion, the amplitude changes caused by $CO_2$ injection cannot be separated from the background differences.

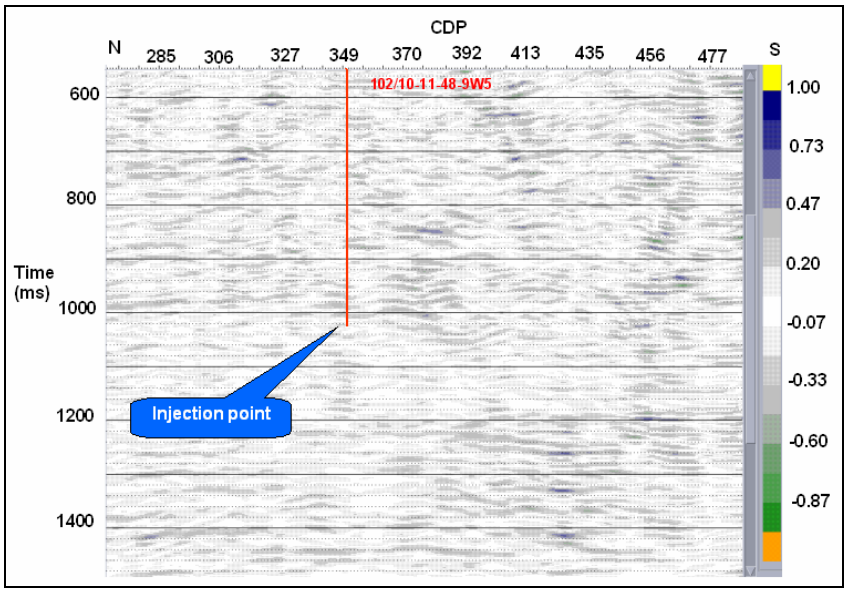


Figure 3.19 PP amplitude differences between monitor and baseline surveys after calibration of line 1 (monitor-baseline, the colours represent normalized amplitude differences).

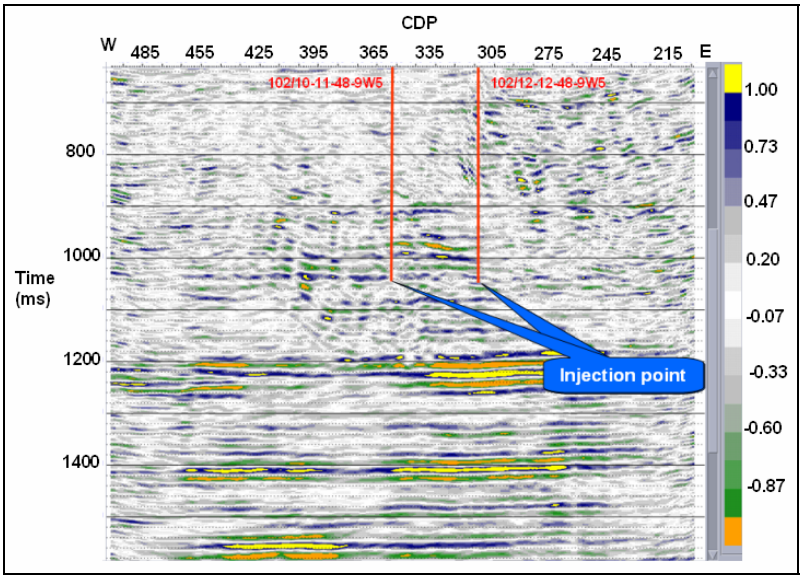


Figure 3.20 PP amplitude differences between monitor and baseline surveys after calibration of line 2 (monitor-baseline, the colours represent normalized amplitude differences).

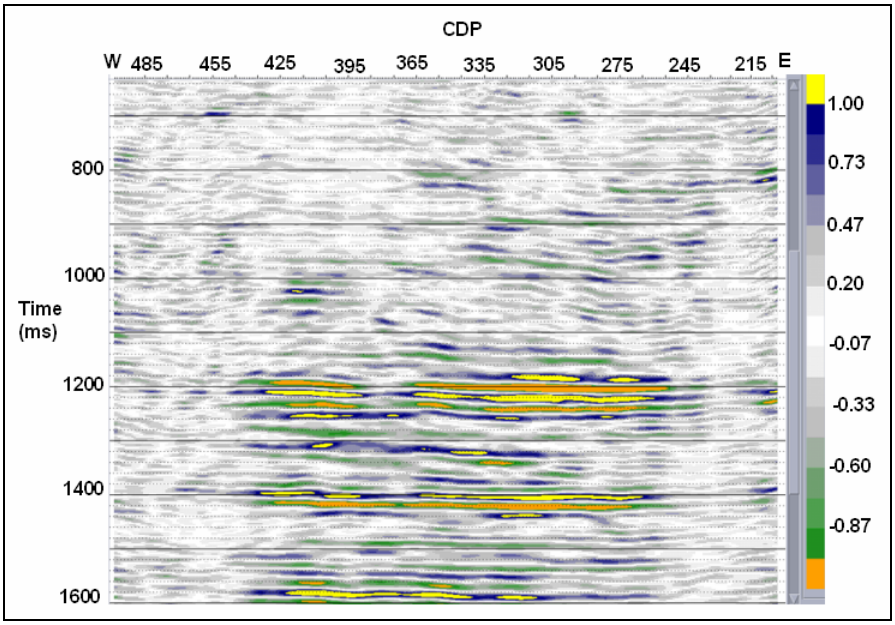


Figure 3.21 PP amplitude differences between monitor and baseline surveys after calibration of line 3 (monitor-baseline, the colours represent normalized amplitude differences).

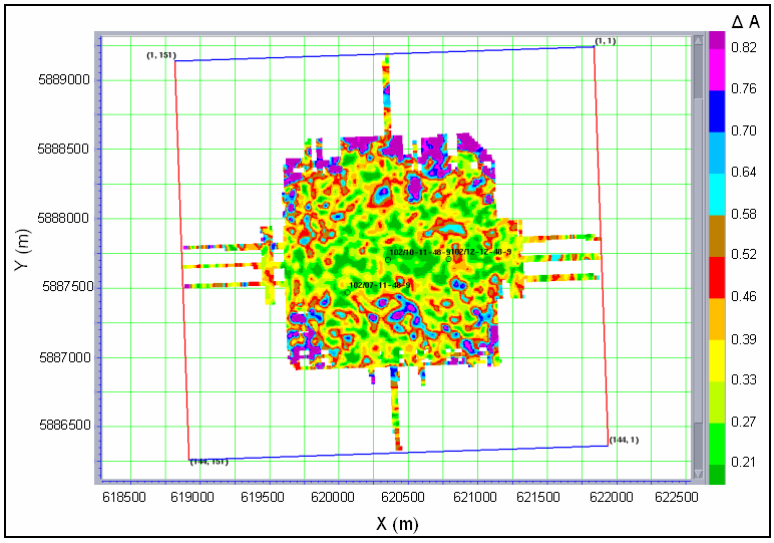


Figure 3.22 RMS amplitude differences of the Cardium reservoir between the monitor and baseline surveys (PP data, monitor-baseline, 1030-1060ms).

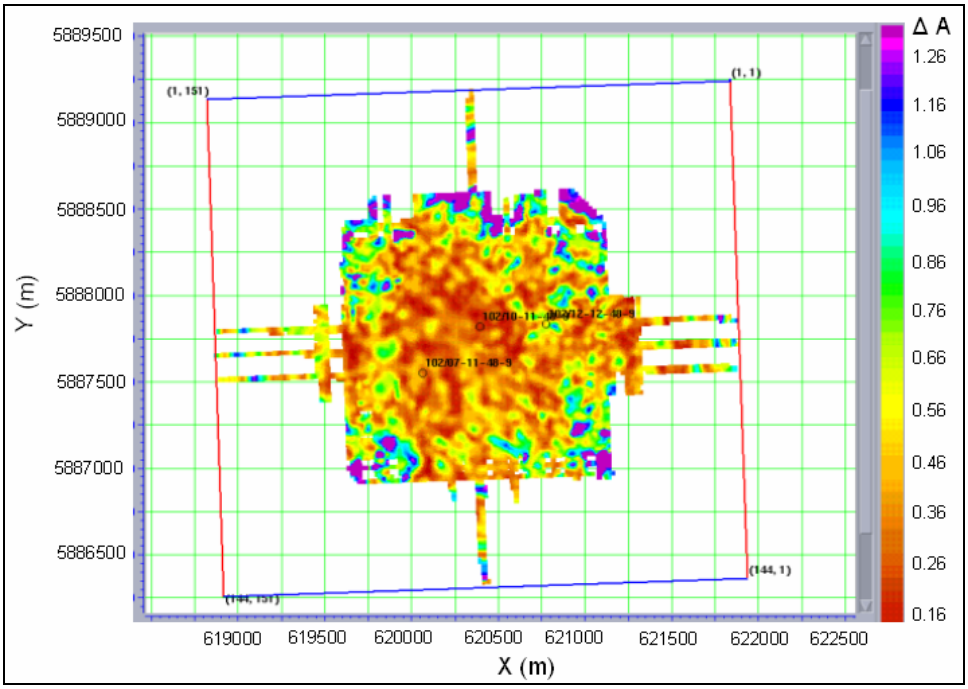


Figure 3.23 RMS amplitude differences around the Viking event between the monitor and baseline surveys (PP data, monitor-baseline, 1200-1230ms).

*3.3.3 Changes in $V_p/V_s$*

Variation in $V_p/V_s$ has been used successfully for direct hydrocarbon detection in some areas (Wang, 2001). Based on the equation: $V_S = \sqrt{\frac{\mu_{sat}}{\rho_B}}$, the shear modulus $\mu_{sat}$ of the rock does not change and the bulk density of the rock decreases after $CO_2$ saturation, therefore shear wave velocities of rocks should increase with $CO_2$ saturation, whereas the compressional wave velocities of rocks will decrease rather than increase after $CO_2$ saturation. As a result, $CO_2$ substitution will result in a decrease in $V_p/V_s$ of rocks. The fluid substitution model also shows that $V_p/V_s$ should decrease approximately 5-6% for the good Cardium reservoir after $CO_2$ injection. However, a limitation of $V_p/V_s$

calculation is that there must be a suitable interval over which to perform the analysis (Miller, 1996). If the interval is much larger than the zone of interest, changes within the target zone may not be detectable. Conversely, if the bounding horizons are too close to the zone of interest, there may be wavelet interference effects which introduce picking errors. In this case, there are no pickable horizons bounding the Cardium sand to perform $V_p/V_s$ analysis for the Cardium Formation. Thus, this method is not suitable for measuring the fluid change in the Cardium reservoir. However, the $V_p/V_s$ values derived from a large interval which contained the Cardium sand were tested to assess possible $CO_2$ leakage and effective stress variations caused by $CO_2$ injection.

Horizon 1, which is a continuous peak at about 600 ms for PP data, and the Viking event were both tracked over the entire 3D volume (Figure 3.24). These two horizons were used to match event times between the PP and PS seismic data and determine the spatial changes in $V_p/V_s$. An automatic picking mode was used to pick the horizons, followed by manual editing. The interval $V_p/V_s$ maps of the baseline and monitor surveys were computed from the PP and PS travel times of the interval between Horizon 1 and Viking by using the following equation (Xu, 2004):

$$V_p/V_s = \frac{2 * \Delta T_{ps}}{\Delta T_{pp}} - 1 \qquad (3\text{-}1)$$

In Figure 3.25 and Figure 3.26, we can see that $V_p/V_s$ between Horizon 1 and the Viking event ranges from 1.85 to 1.95, which means the lithology within this interval is

quite constant laterally in the 3D survey. The $V_p/V_s$ difference map (Figure 3.27) between the monitor and baseline surveys was computed from the data shown in Figures 3.25 and 3.26. The $V_p/V_s$ differences between the monitor and baseline surveys range from -0.02 to 0.02. There is no identifiable $V_p/V_s$ decrease around the $CO_2$ injection wells.

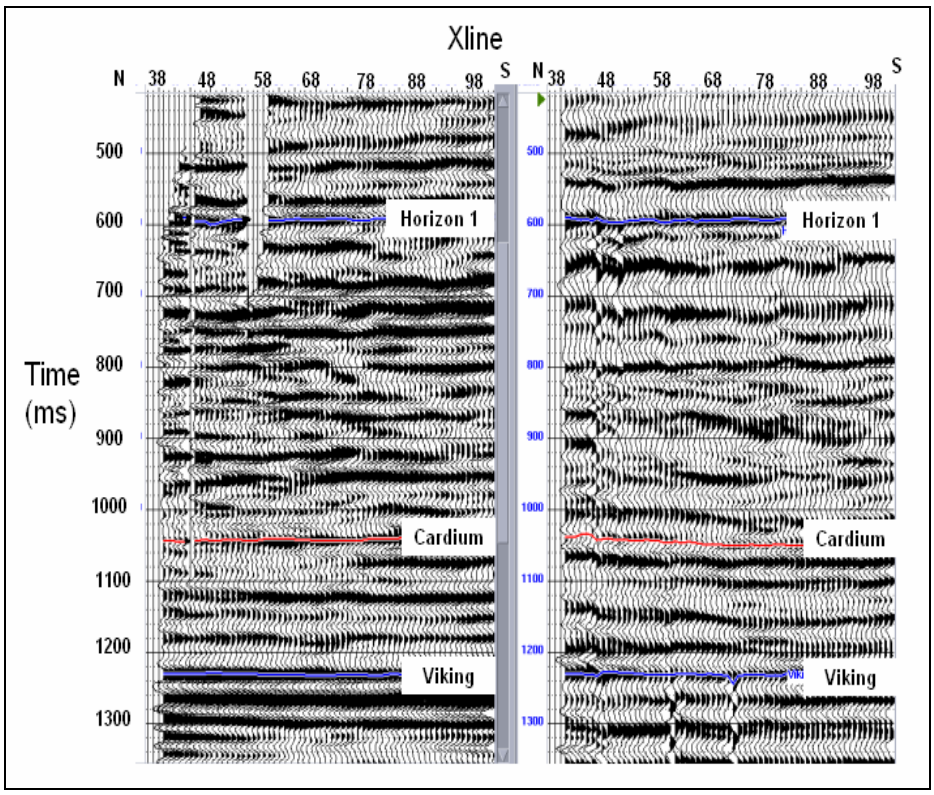


Figure 3.24 Inline 81 with horizons used for $V_p/V_s$ interpretation (PP data, left; PS data shown in PP domain, right).

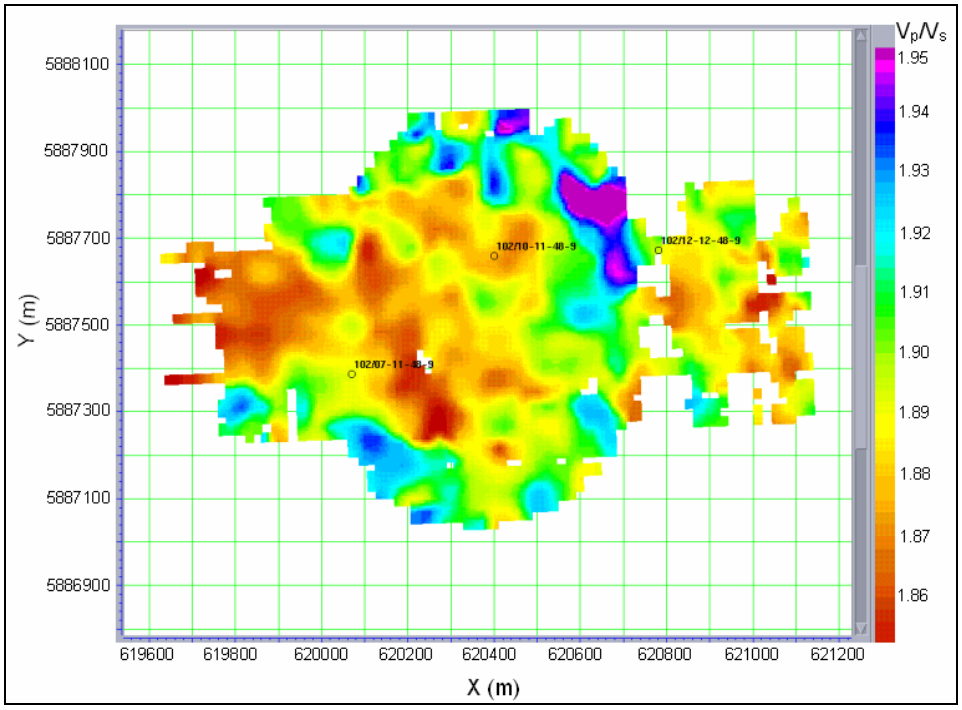


Figure 3.25 Interval $V_p/V_s$ map between Horizon 1 and Viking (baseline).

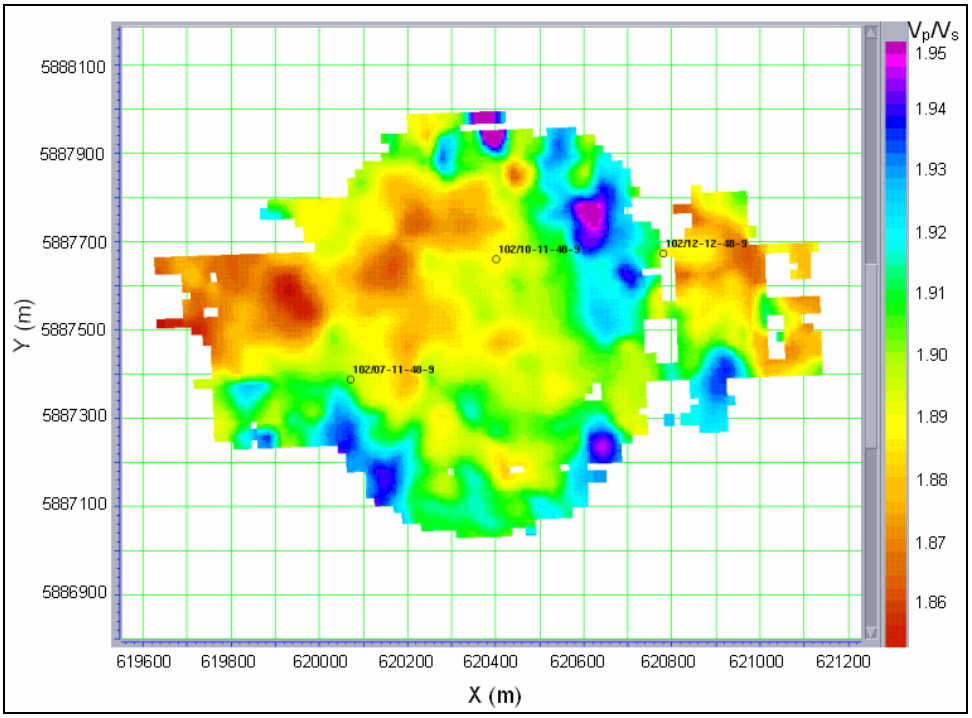


Figure 3.26 Interval $V_p/V_s$ map between Horizon 1 and Viking (monitor survey).

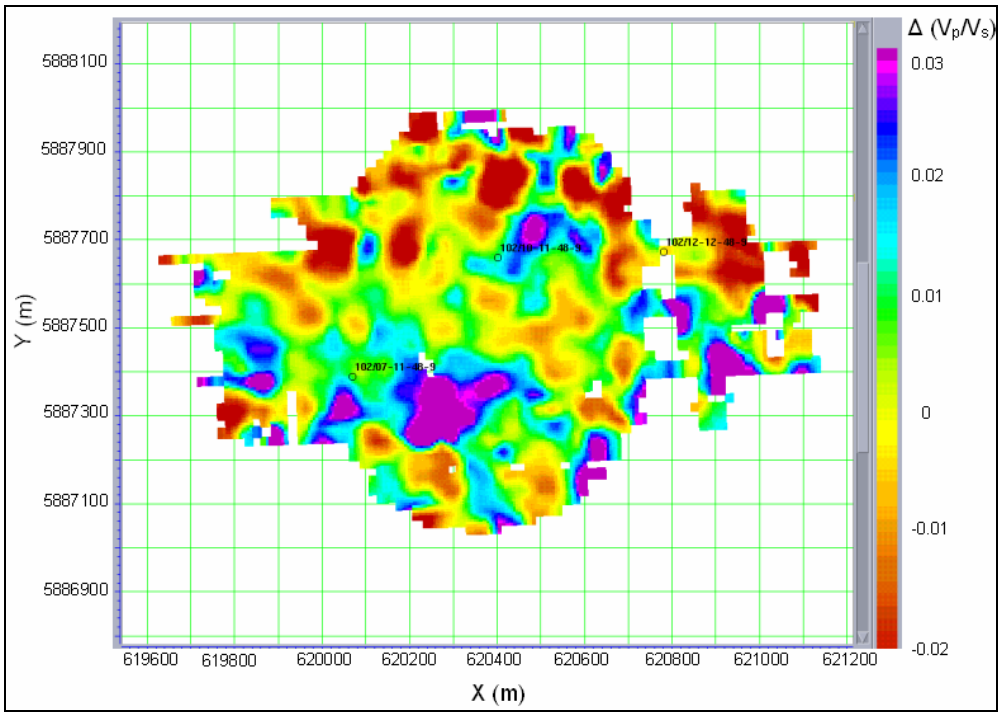


Figure 3.27 $V_p/V_s$ differences between Horizon1 and Viking (monitor-baseline).

*3.3.4 Discrimination between effective stress and fluid saturation changes*

Petrophysical experiments have shown that the combined effects of pore pressure build-up and fluid substitution caused by $CO_2$ flooding should make it feasible to monitor the $CO_2$ flood process with time-lapse PP data (Wang, 1998). However, $V_p$ is sensitive to both the $CO_2$ saturation and increase of pore pressure. However, when pore pressure changes and fluid saturation changes are both present, it is impossible to discriminate between the two from PP data only (Landrø, 2003). $V_s$ is insensitive to fluid changes. The fluid substitution modeling in Chapter 2 also shows that $CO_2$ substitution causes a small increase (instead of decrease) in $V_s$ because of the small decrease of density after $CO_2$ substitution. However, $V_s$ is particularly sensitive to the pore pressure change (Wang,

1998). If the pore pressure ($P_p$) increases and the confining pressure ($P_c$) does not change, then the differential pressure ($P_d$, $P_d=P_c-P_p$) between the confining and pore pressure decreases. Christensen and Wang (1985) showed that a decrease of differential pressure results in a decrease in $V_s$ (Figure 3.28). Therefore, multi-component data may be useful together to separate pressure effects from $CO_2$ saturation effects.

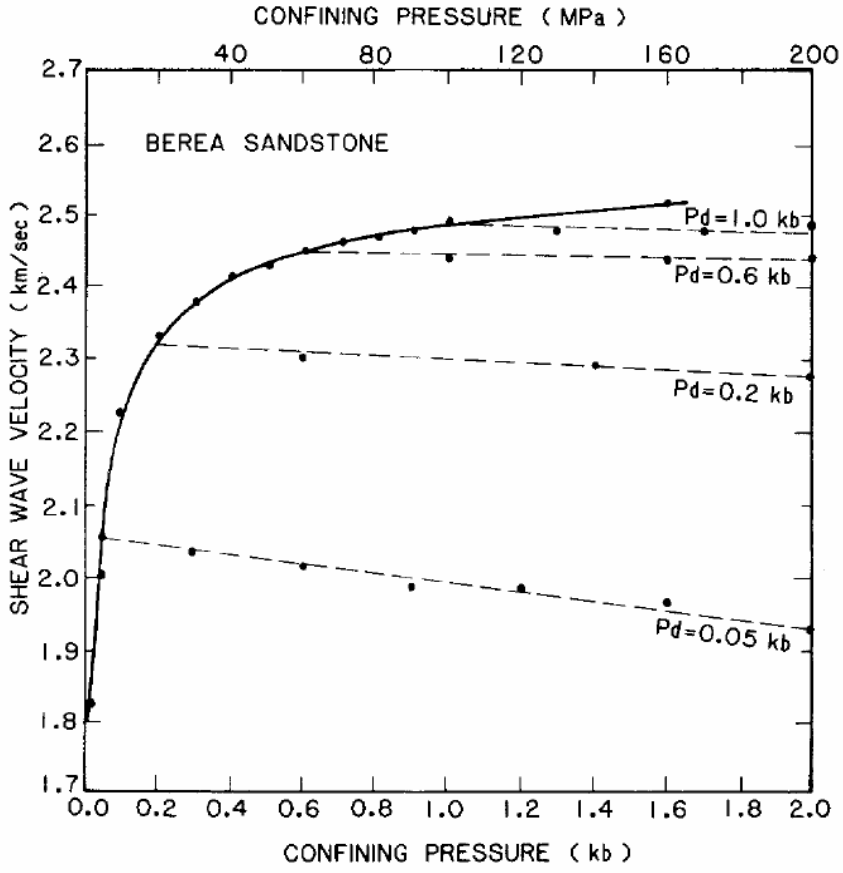


Figure 3.28 Shear-wave velocities as functions of confining pressure and differential pressure ($P_d$) (Christensen and Wang, 1985).

The PS amplitude difference between the monitor and baseline surveys of line 1 is shown in Figure 3.29. We can see that there are several anomalous zones below the

Cardium event. It is uncertain if these anomalies are due to noise, $CO_2$ injection, or changes in effective stress, but it is recommended that follow-up research on these anomalies be undertaken.

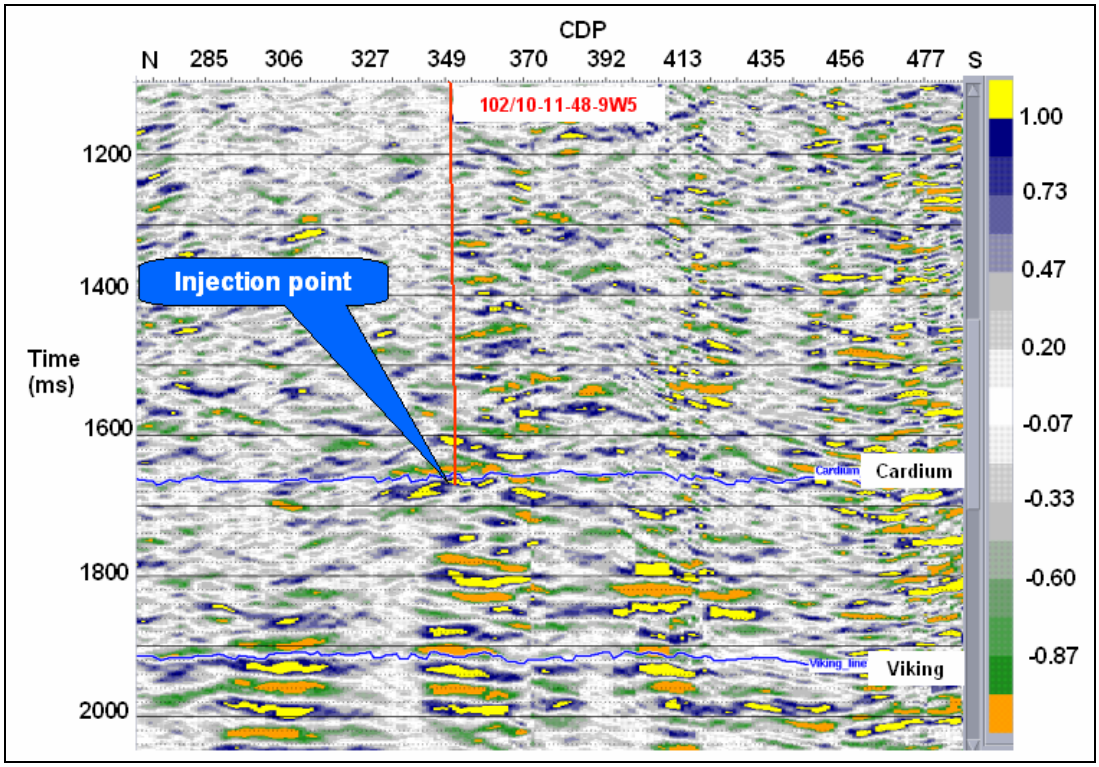


Figure 3.29 PS amplitude differences between the monitor and baseline surveys of line 1 (monitor-baseline, the colours represent normalized amplitude differences after calibration).

### 3.4 Chapter summary

Synthetic seismograms were made from two wells at the Violet Grove $CO_2$ injection site and the synthetic seismograms match the surface seismic data very well. The top of the Cardium sand correlates to a weak peak at approximately 1043 ms and

1690 ms in the PP and PS survey, respectively. Three steps of calibration, which are phase and time matching, application of a shaping filter, and cross normalization, were applied to the monitor survey prior to 4D seismic interpretation. Several methods, including time shift, amplitude difference, and $V_p/V_s$, were tested but were found to be not effective to identify the $CO_2$ distribution because of the subtleness of the anomaly related to $CO_2$ injection.

# CHAPTER 4: POST-STACK IMPEDANCE INVERSION

## 4.1 Introduction

Seismic inversion is the calculation of the earth's structure and physical parameters from some set of observed seismic data (Cooke and Schneider, 1983). Post-stack impedance inversion attempts to recover a broadband pseudo-acoustic impedance log from a band-limited post-stack seismic trace (Russell, 1988). The input data for this process consists of the following elements: one or more wells with density and sonic logs, a seismic volume, either 2D or 3D, and a set of picked horizons. The output data is a volume of derived acoustic impedance (Russell, 2001). In this study, after $CO_2$ injection, both the density and P-wave velocity of the reservoir will decrease. The P-wave impedance, therefore, will also decrease. As a result, post-stack impedance inversion is potentially a useful tool to identify the $CO_2$-flooded area.

There are several different inversion methods available in the software used for the analysis (H-R Strata): bandlimited, sparse spike, model based, and neural network inversions.

Bandlimited inversion is the classical recursive inversion algorithm which is based on the following well-known formula giving a reflection coefficient in terms of the adjacent acoustic impedances:

$$RC_n = \frac{(\rho V)_{n+1} - (\rho V)_n}{(\rho V)_{n+1} + (\rho V)_n}, \qquad (4\text{-}1)$$

where:

$RC_n$ is the reflection coefficient of the nth interface,

$(\rho V)_n$ is the product of the density and velocity (the impedance) on the nth interval.

If one views a seismic trace as a reflection coefficient series and $(\rho V)_0$ is known, then the seismic trace can be transformed to impedances by rewriting Equation 4-1 (Cooke, 1983). The advantage of this method is its simplicity, short computation time, and robustness in the presence of noise. The disadvantage is that ignoring the wavelet, the output is in wiggle trace format similar to seismic data (Russell, 2001).

Sparse spike inversion is based on the theory of maximum-likelihood deconvolution, which assumes that the earth's reflectivity is composed of a series of large events superimposed on a Gaussian background of smaller events. The advantage of this method is that the low frequency information is included mathematically in the solution, and a geological looking inversion is produced. The disadvantage of it is that final output lacks fine detail and is subject to noise.

Model-based inversion builds a geological model first and calculates the synthetic seismograms using the initial guess impedance and the known wavelet, and then the initial model is updated gradually until the resulting synthetic traces match the real seismic data within some tolerance level (Russell, 2001). The advantage of this method is that errors are distributed through the solution. The disadvantage of it is of non-uniqueness.

Neural network inversion is a mathematical algorithm which encodes the relationship between the following two data sets: (1) a single composite trace at each well location, calculated by averaging along the borehole trajectory; (2) the known acoustic

impedance from the well at that location. Using a neural network consists of two steps: training the network and finding the relationship between the two data sets, and applying the trained neural network to a larger volume of data on which we wish to use the relationship (Hampson-Russell, 2001). Theoretically, the neural network inversion can obtain high resolution, but it is time-consuming, and the resolution depends on the number of training samples.

### 4.2 Inversion analysis

Prior to doing the final inversion, inversion analysis at selected traces was undertaken to test different inversion methods and parameters (e.g. Figures 4.1 through 4.4). The correlation coefficients between the synthetic trace and the real seismic trace by using different inversion methods and parameters were compared. Based on this inversion analysis, model-based inversion method was preferred and was used to perform the final analysis. Parameters used in the final model-based inversion are shown in Table 4.1.

| Inversion option | Constrained |
|---|---|
| Maximum impedance change (hard constraints) | Single value: lower 25%, and upper 25% |
| Average block size | 2 ms |
| Prewhitening | 1% |
| Number of iterations | 7 times |

Table 4.1 Parameters used in the final model-based inversion.

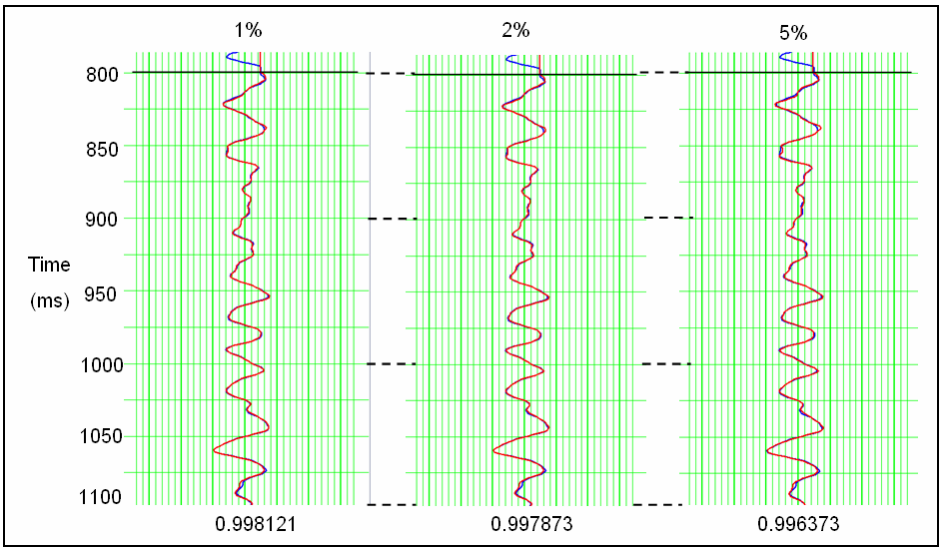


Figure 4.1 Correlation results between the seismic trace and the synthetic trace of well 102/07-11-48-9W5 with different pre-whiting parameters for model-based inversion. Red curve is synthetic trace; blue curve is seismic trace at the well location; the pre-whiting parameters are shown at the top of each trace; the correlation coefficients are shown at the bottom of each trace.

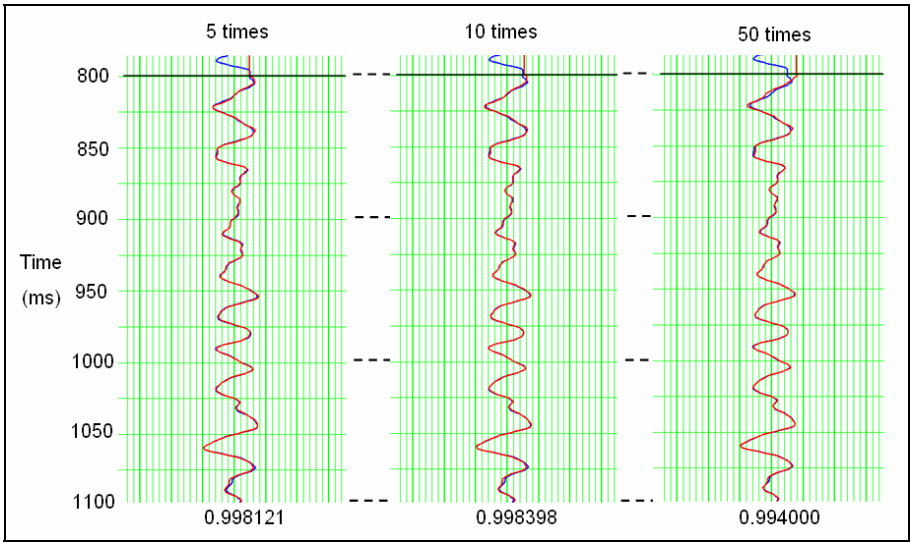


Figure 4.2 Correlation results between the seismic trace and the synthetic trace of well 102/07-11-48-9W5 with different iteration times for model-based inversion. Red curve is synthetic trace; blue curve is seismic trace at the well location; the correlation coefficients are shown at the bottom of each trace.

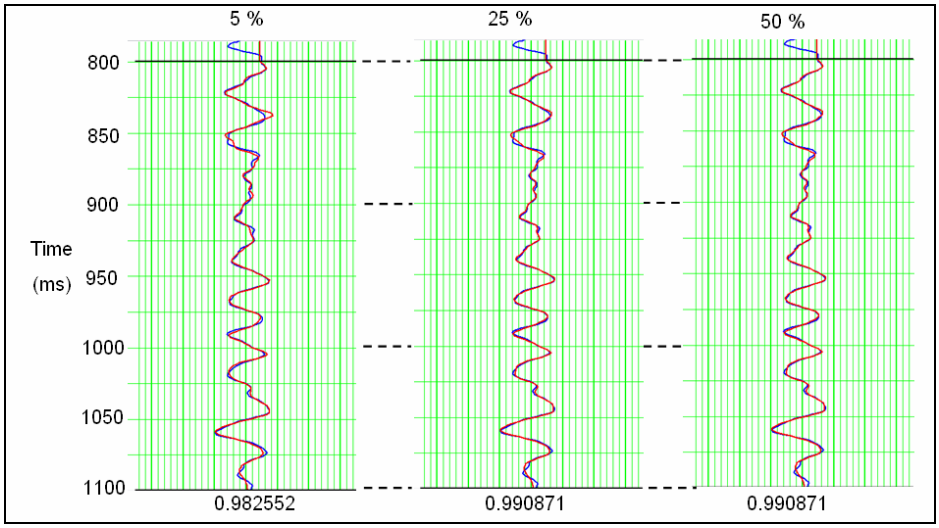


Figure 4.3 Correlation results between the seismic trace and the synthetic trace of well 102/07-11-48-9W5 with different impedance constraint parameters for model-based inversion. Red curve is synthetic trace; blue curve is seismic trace at the well location; the correlation coefficients are shown at the bottom of each trace.

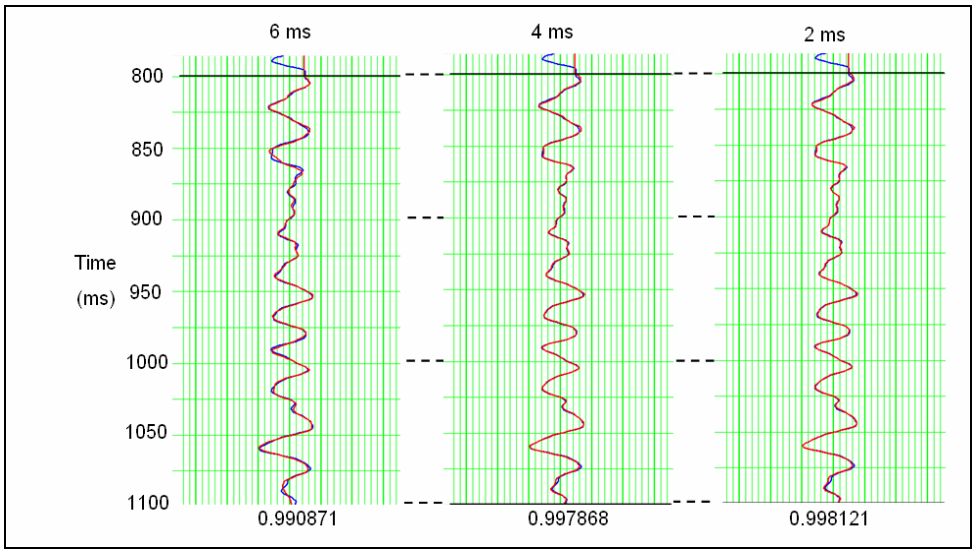


Figure 4.4 Correlation results between the seismic trace and the synthetic trace of well 102/07-11-48-9W5 with different average block sizes for model-based inversion. Red curve is synthetic trace; blue curve is seismic trace at the well location; the correlation coefficients are shown at the bottom of each trace.

### 4.3 Inversion results

Model-based inversion was used to perform the final impedance inversion. An initial model was created for each of the baseline and monitor survey of Line 1 based on horizon interpretations (e.g. Figure 4.5). Well 102/08-14-48-9W5 was projected to the $CO_2$ injection location and used as the control well for the initial models. The density and P-wave velocity logs of wet model, which were generated from the fluid substitution process, were used into the baseline survey inversion model; the density and P-wave velocity logs of the $CO_2$ model were then used into the monitor survey inversion model. The final inversion results of the baseline and monitor surveys are shown in Figure 4.6 and Figure 4.7, respectively. The impedance difference map between the monitor and baseline surveys of Line 1 was generated from these data (Figure 4.8). There is a small impedance anomaly in and above the Cardium Formation around the $CO_2$ injection zone, which may be meaningful and generated by $CO_2$ injection. However, when we check the impedance inversion results of line 2 (Figures 4.9, 4.10) and the impedance difference map from it (Figure 4.11), there appear to be no meaningful anomalies, which match the $CO_2$ injection locations. As a result, it remains uncertain if the $CO_2$ flooding zone can be reliably identified by post stack impedance inversion at the time of first monitor survey.

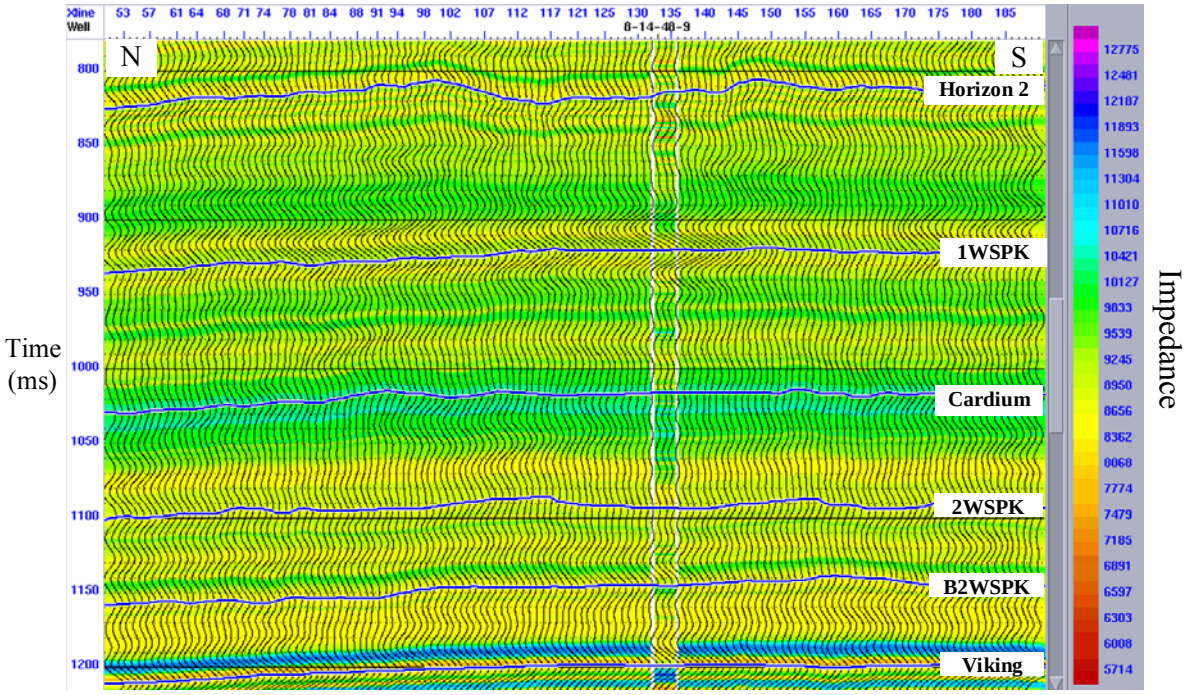


Figure 4.5 The initial model of Line 1 (monitor survey). The computed P-wave impedance is displayed as variable density colors ((g/cm$^3$)(m/s)).

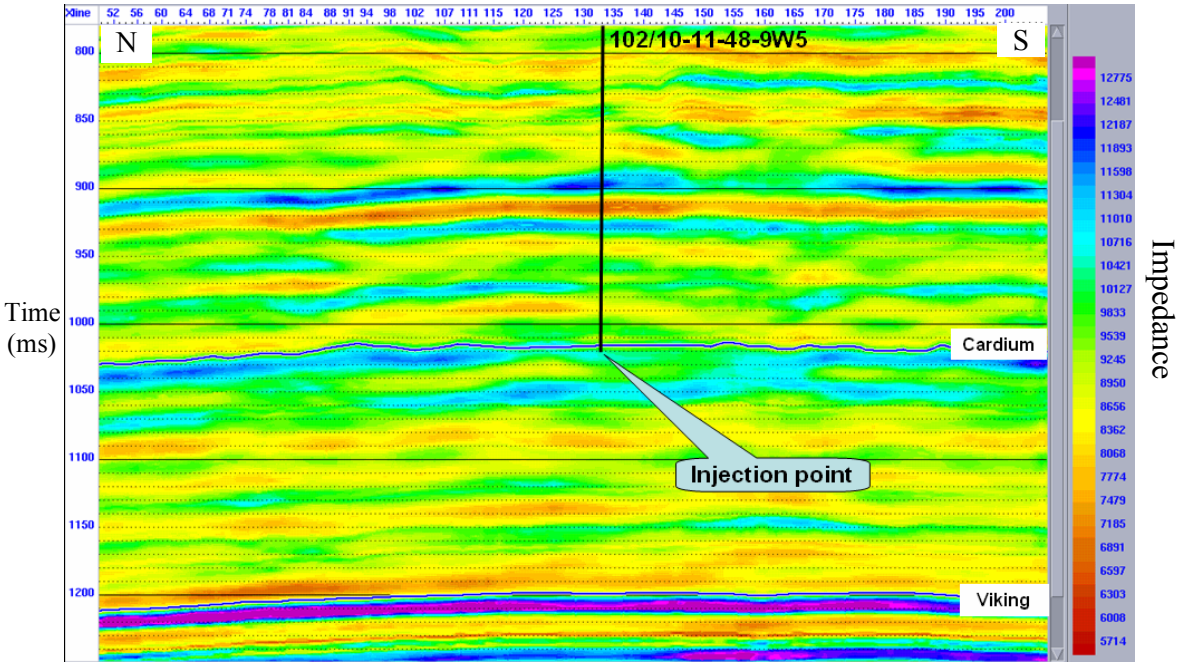


Figure 4.6 Post-stack PP impedance inversion of Line 1(baseline survey). The P-wave impedance is displayed as variable density colors ((g/cm$^3$)(m/s)).

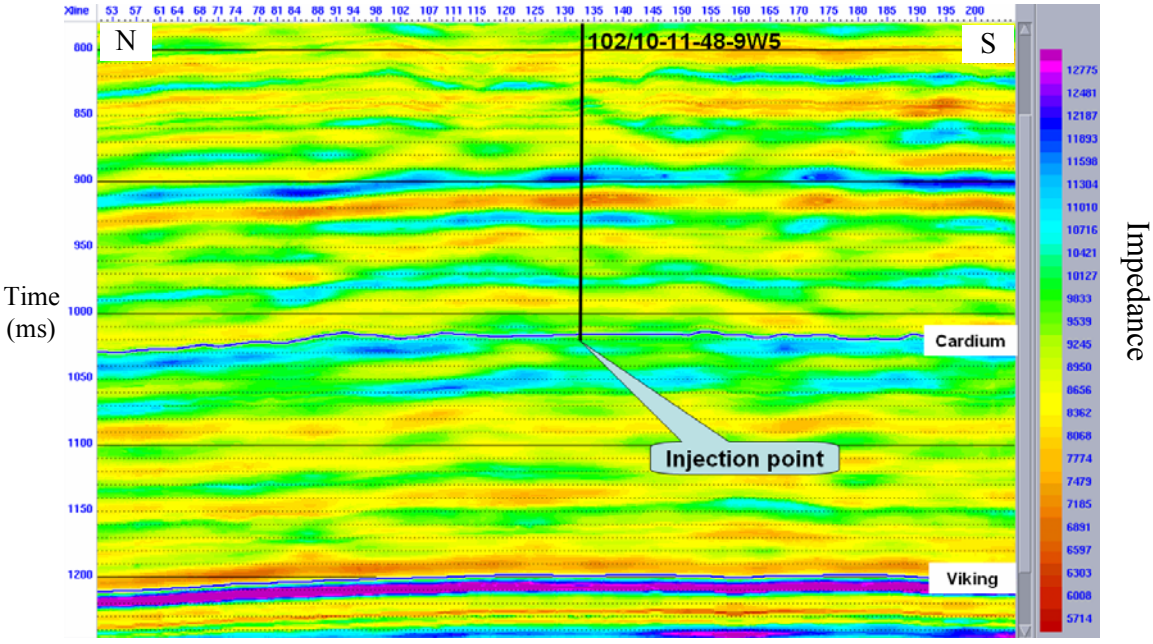


Figure 4.7 Post-stack PP impedance inversion of Line 1(monitor survey). The P-wave impedance is displayed as variable density colors ((g/cm$^3$)(m/s)).

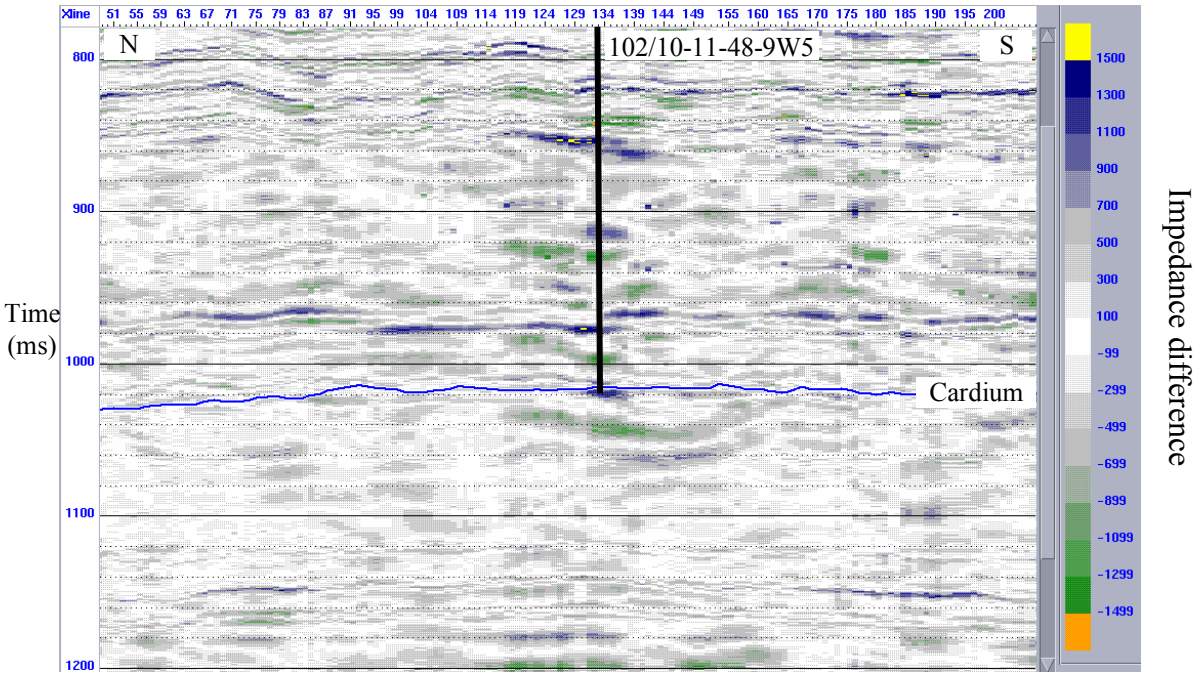


Figure 4.8 Post-stack PP impedance differences between the baseline and monitor surveys of Line 1(monitor-baseline, different colors represent impedance differences in (g/cm$^3$)(m/s)).

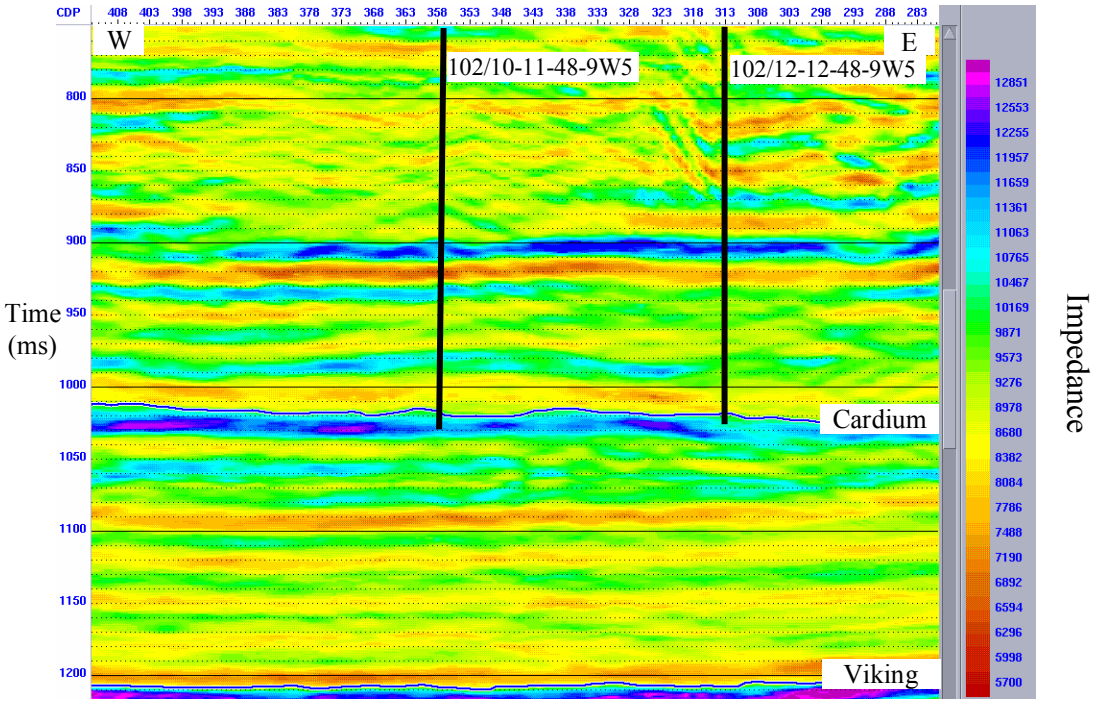


Figure 4.9 Post-stack PP impedance inversion of Line 2 (baseline survey). The P-wave impedance is displayed as variable density colors ((g/cm$^3$)(m/s)).

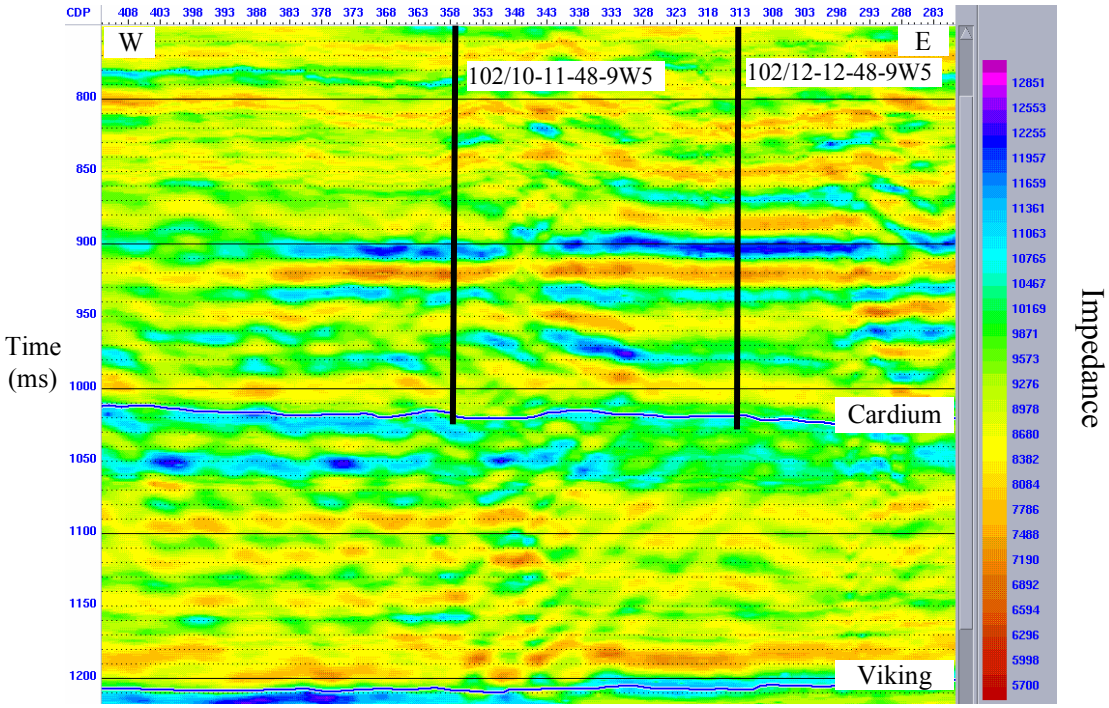


Figure 4.10 Post-stack PP impedance inversion of Line 2 (monitor survey). The P-wave impedance is displayed as variable density colors ((g/cm$^3$)(m/s)).

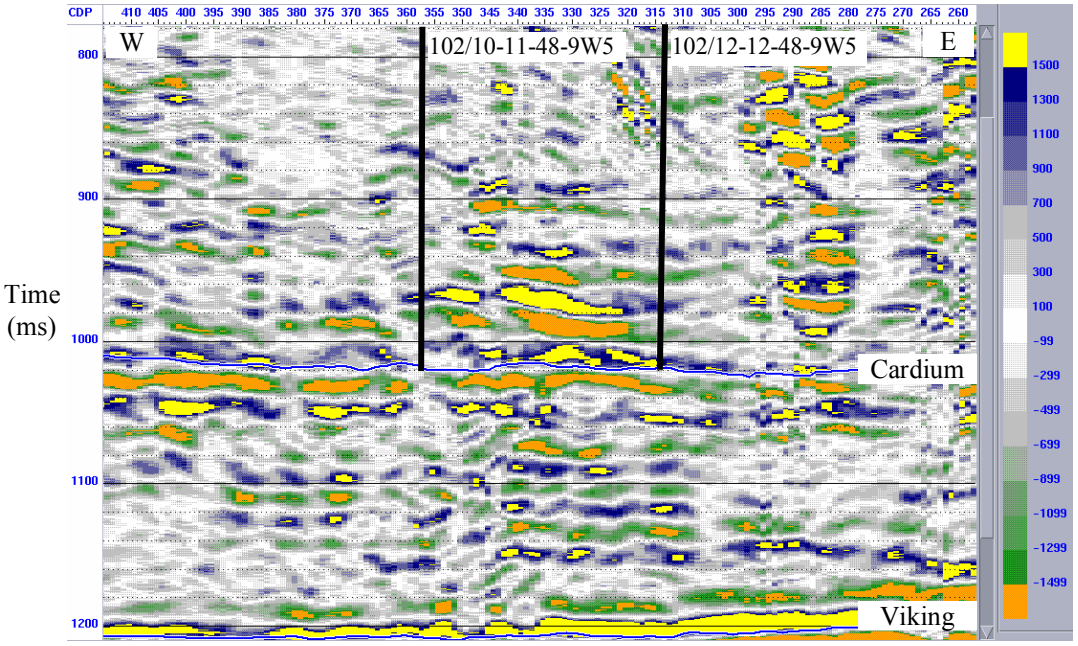


Figure 4.11 Post-stack PP impedance differences between the baseline and monitor surveys of Line 2 (monitor-baseline, different colors represent impedance differences in $(g/cm^3)(m/s)$).

# CHAPTER 5: AVO INVERSION OF THE TIME-LAPSE 2D DATA

## 5.1 Theory

For a normal incident compressional plane wave, the incident energy is both reflected and transmitted at the interface, and the reflection coefficient depends on the difference between the seismic impedances of the two layers (Figure 5.1):

$$R_0 = \frac{\rho_2 V_{p2} - \rho_1 V_{p1}}{\rho_2 V_{p2} + \rho_1 V_{p1}}, \qquad (5\text{-}1)$$

where:

$R_0$ is the normal incident reflection coefficient,

$\rho_1$ and $V_{p1}$ represent the density and P-wave velocity of layer 1, respectively,

$\rho_2$ and $V_{p2}$ represent the density and P-wave velocity of layer 2, respectively.

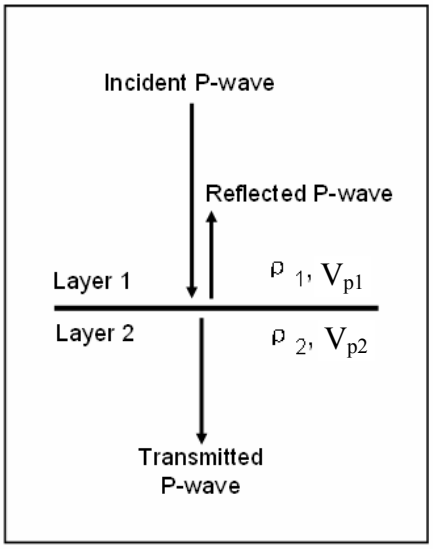


Figure 5.1 Schematic diagram of a normal incident P-wave.

For a non-normal incident compressional plane wave, the energy of the incident wave is partitioned at the impedance interface into four components: reflected

compressional, reflected shear, transmitted compressional, and transmitted shear waves (Figure 5.2). The reflection amplitudes vary with the angle of incidence (AVA), and therefore with source-receiver offset (AVO). The exact reflection coefficient is defined by the well-known Zoeppritz equations, which give the reflection coefficient for plane waves as a function of angle of incidence and six independent elastic parameters, three on each side of the reflecting interface (Shuey, 1985). The core objective of AVO inversion is to make inferences about the elastic properties of reservoir rocks from observation of reflection amplitude as a function of angle (offset), and relate this to a possible change in fluid saturation, especially gas, within the reservoir rocks.

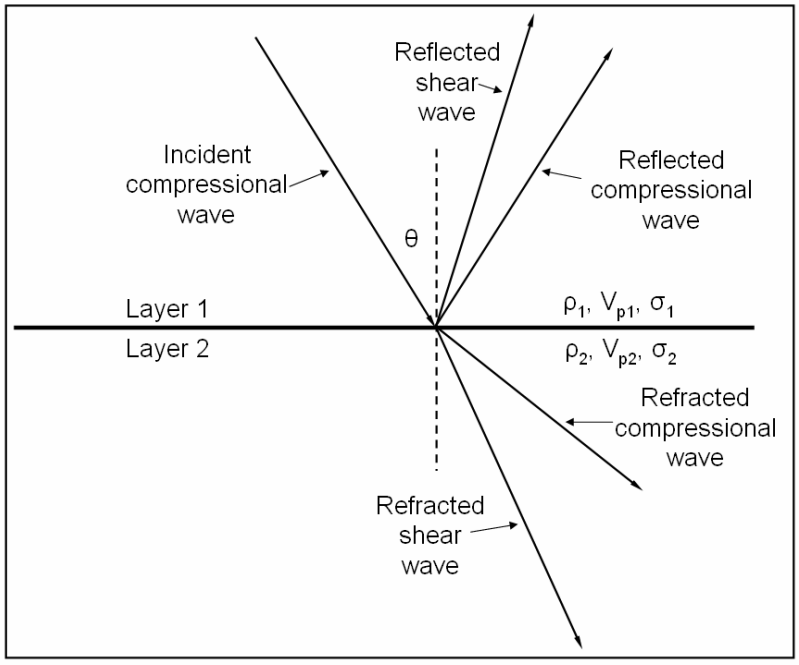


Figure 5.2 Partitioning of the incident P-wave energy into four components ($\rho$, $V_p$, and $\sigma$ represent density, P-wave velocity, and Poisson's ratio of each layer, respectively).

The exact solution for the PP reflection coefficient derived from the Zoeppritz equations is cumbersome and not intuitive in terms of its practical use for inferring petrophysical properties of reservoir rocks. Fortunately, for small change in the elastic properties across an interface and small angles of incidence (less than 30˚) commonly encountered in seismic reflection applications, the exact solution can be quite accurately approximated (e.g. Bortfeld, 1961; Aki and Richards, 1980; Shuey, 1985; Smith & Gidlow, 1987; Fatti et al., 1994). Following Shuey's two-term AVO equation (Shuey, 1985), the P-wave reflection coefficient as a function of angle of incidence can be expressed as:

$$R(\theta) \approx A + B\sin^2\theta, \qquad (5\text{-}2)$$

$$A = \frac{1}{2}\left(\frac{\Delta V_p}{V_p} + \frac{\Delta\rho}{\rho}\right), \qquad (5\text{-}3)$$

$$B = \frac{1}{2}\frac{\Delta V_p}{V_p} - 4\frac{V_s^{\,2}}{V_p^{\,2}}\frac{\Delta V_s}{V_s} - 2\frac{V_s^{\,2}}{V_p^{\,2}}\frac{\Delta\rho}{\rho}, \qquad (5\text{-}4)$$

where,

R (θ) is the reflection coefficient for PP-wave,

A is the normal incident reflection coefficient $R_0$, which is usually called AVO intercept,

B is usually called AVO gradient,

θ is the average of the incidence and transmission angles for the P-wave, which is similar to the incident angle for angles less than 30˚,

$V_p$ is the average P-wave velocity, which equals $(V_{p1}+V_{p2})/2$, and $\Delta V_p$ equals $(V_{p2}-V_{p1})$,

$V_s$ is the average S-wave velocity, which equals $(V_{s1}+V_{s2})/2$, and $\Delta V_s$ equals $(V_{s2}-V_{s1})$,

ρ is the average density, which equals $(\rho_1+\rho_2)/2$, and Δ ρ equals $(\rho_2-\rho_1)$,

Based on Equation 5-2, if $R(\theta)$ is plotted against $\sin^2\theta$, then a straight line should be obtained. The intercept (A) gives the normal incident reflection coefficient, and the slope of the line (B) is related to $V_p$, $V_s$ and density and may indicate the saturation in reservoir rocks (Yilmaz, 2001; Koefoed, 1955).

In practice, seismic reflections from gas sands exhibit a wide range of AVO characteristics. Based on the work of Rutherford and Williams (1989), Castagna et al. (1998) proposed a new classification of gas sands based on location in the A-B plane, rather than on normal incidence reflection coefficient, and the fourth AVO type of gas sands was added to the classification of Rutherford and Williams (Figure 5.3). For Class 1 AVO, the gas sands have higher impedance than the encasing shales; the tops of the gas sands have positive normal-incidence reflection coefficients, lie in quadrant IV, and decrease in amplitude magnitude with increasing offset faster than the background trend. For Class 2 AVO, the gas sands have nearly the same impedance as the encasing shales; the tops of the gas sands have near-zero $R_0$ values and characterized by a marked decrease in amplitudes with increasing offset; polarity reversals are common with this type of reflector, which can in either quadrants II, III, or IV (phase-reversal anomaly). For class 3 AVO, the gas sands have lower impedance than the encasing shales; the tops of the gas sands have a strongly negative normal-incidence reflection coefficient, which becomes more negative with increasing offset (bright-spot anomaly); these sands lie in quadrant III. Class IV gas sands also have a negative normal-incidence reflection coefficient, but lie in quadrant II and decease in amplitude magnitude with offset.

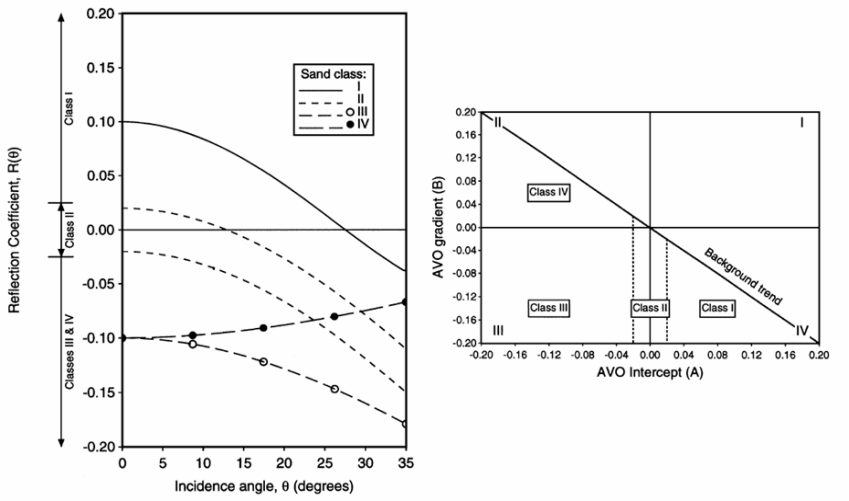


Figure 5.3 Plane-wave reflection coefficients at the top of each classification of gas sands (left) and AVO intercept (A) versus gradient (B) cross plot (right) (Rutherford and Williams, 1989; Castagna, et al., 1998).

Different AVO parameters, such as AVO intercepts (A), AVO gradients (B), A*B (AVO product), and the scaled Poisson's ratio change, are used as possible gas indicators. Some AVO indicators are sensitive only to specific AVO anomalies; therefore, selection of attributes is crucial for successful AVO analysis. AVO interpretation may be facilitated by cross plotting extracted seismic parameters. Under a variety of reasonable petro-physical assumptions, brine-saturated sandstones and shales follow a well-defined "background" trend in the A-B plane; deviations from the background trend may be indicative of hydrocarbons or lithologies with anomalous elastic properties. However, the interpretation of such A versus B cross plots is often complicated by scatter caused by poor seismic data quality, and non-petrophysical influences (Castagna, 1998).

## 5.2 AVO Modeling

AVO modeling is important to understand which AVO responses are indicative of $CO_2$ injection because it permits direct correlation of lithology and pore fluid measurements with observed seismic data by constructing non-normal incident synthetic seismograms from well logs.

The P-wave sonic and density logs of well 102/08-14-48-09W5 were used for AVO modeling. Fluid replacement of the in-situ pore fluids in the Cardium sand was performed using Hampson-Russell software (AVO). All the fluid and rock parameters used were as same as those in Chapter 2. The wavelet used for synthetic seismograms was extracted from the 3D baseline survey using statistical method, and offsets from 0 to 1650 m were modeled using Zeoppritz algorithm. In Figure 5.4, we can see that the top of the Cardium sand has a positive normal-incidence reflection coefficient and decreases in amplitude with increasing offset; therefore, it belongs to Class I AVO type or a type between Class I and Class II.

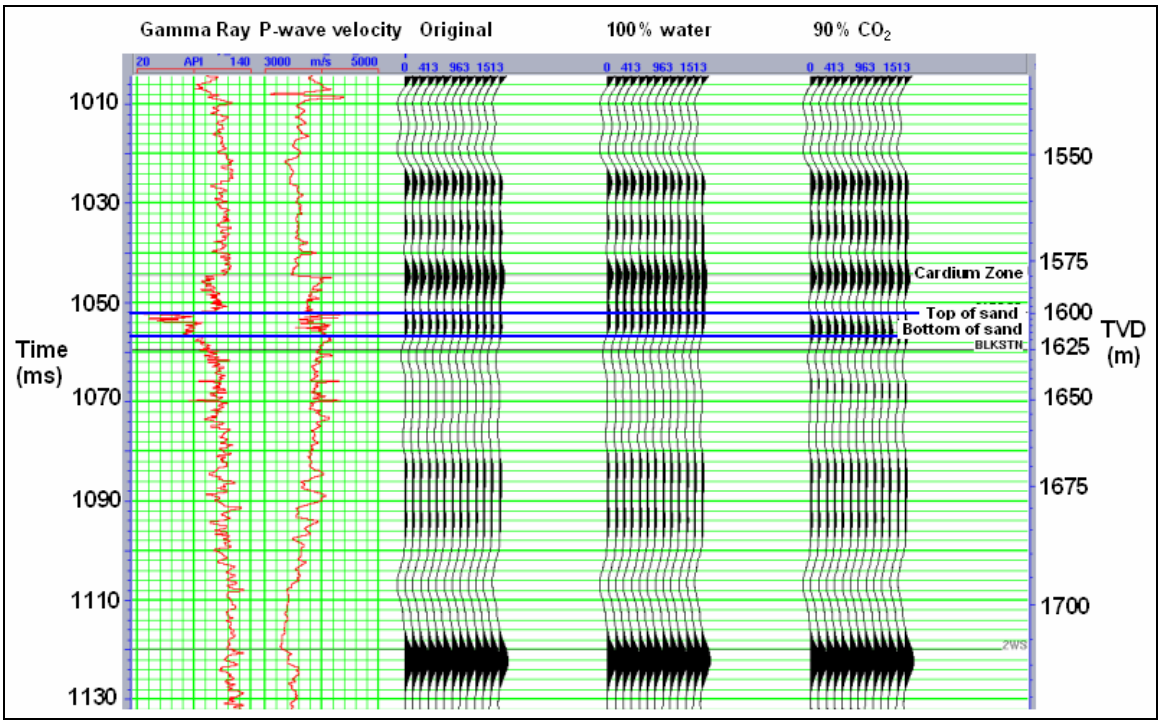


Figure 5.4 Synthetic seismograms before and after fluid substitutions of well 102/08-14-48-9W5. The panel on the left is the synthetic seismogram with in-situ fluid in the Cardium sand; the panel in the middle is the synthetic seismogram with 100% water in the Cardium sand; the panel on the right is the synthetic seismogram with 90% $CO_2$ and 10% water in the Cardium sand.

Two primary attributes (the intercept A, and the product of intercept and gradient A*B) were extracted from the synthetic seismograms. In Figure 5.5, the first five traces are the in-situ (50% water, 50% oil) model; the second five traces are the wet (100% water) model; the last five traces are the $CO_2$ (90% $CO_2$, 10% water) model. The trace data is the intercept (A); while the color data is the product of intercept and gradient (A*B). There exist weak AVO anomalies at the base of the Cardium sand for the $CO_2$ model: the AVO products become larger than the original fluid and wet models and the color changes from green to light blue.

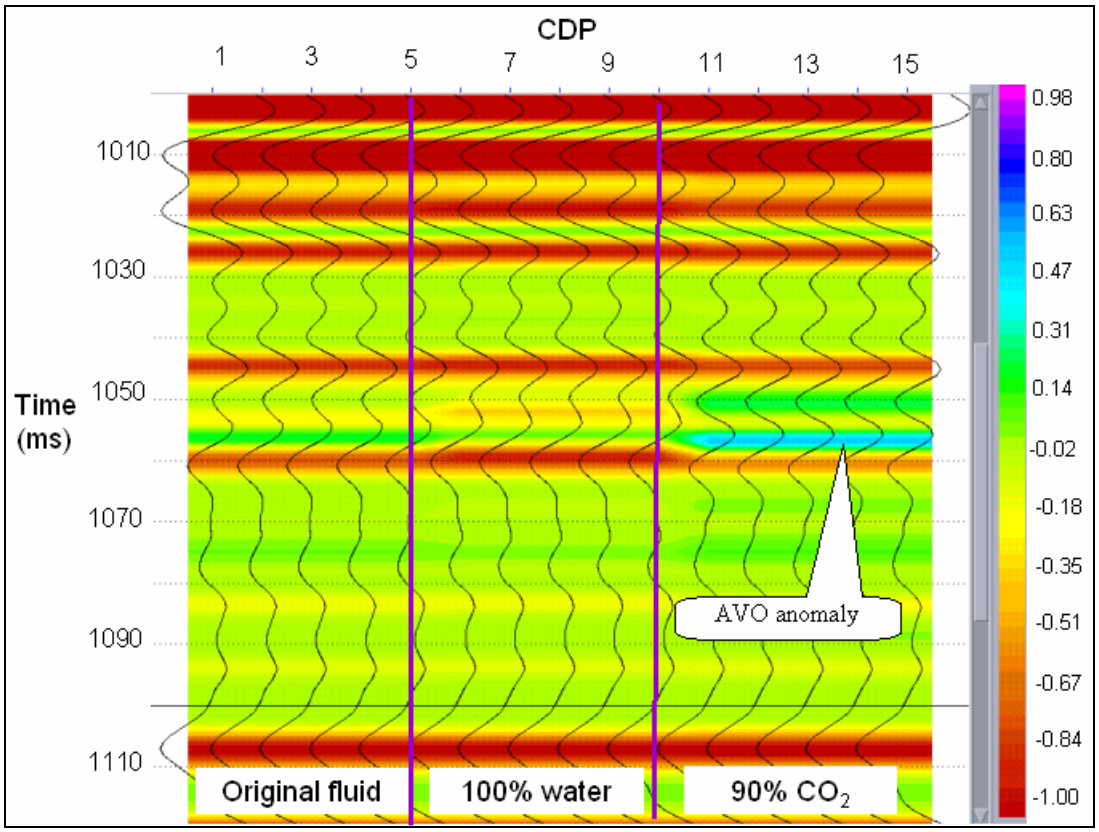


Figure 5.5 AVO attributes of the synthetic CDP gathers in Figure 5.4. The intercept (A) is presented in trace display (wiggle), the product of AVO intercept and gradient (A*B) is displayed as variable density colors; the original fluid model is on left, the wet model on center, and the $CO_2$ model on right.

### 5.3 AVO Inversion

The required input data for AVO inversion are CDP gathers (Figure 5.6), but we can see that the original CDP gathers are too noisy to perform AVO analysis, especially the near offset traces (from offset 0 to 200 m). In order to improve the signal-to-noise ratio, super gathers were generated by averaging 5 original CDPs with offset binning of 140 m (Figure 5.7 and Figure 5.8). In Figure 5.7 and Figure 5.8, we can see that the super CDP gathers look cleaner than the original CDP gathers. Also, the AVO character is

maintained, such as the positive reflection at about 905 ms; but the reflections of the Cardium are still very weak.

AVO attribute inversion was undertaken from both the baseline and monitor super gathers of line 1 (Figure 5.9 and Figure 5.10). Even though there are differences between the two sections, it seems all the differences are caused by noise and there are no meaningful AVO anomalies at the $CO_2$ injection point on both the baseline and monitor sections. A possible explanation is that the AVO anomaly for the $CO_2$ model is based on the $CO_2$ substitution of interval from 1605-1623m; however, if the $CO_2$ is limited in the very thin (about 6 m) good Cardium sand, the magnitude of the AVO anomaly on real seismic data will be significantly less than the modeling result. Therefore, the AVO anomaly caused by the injected $CO_2$ is very small and cannot be identified at the time of the first monitor survey.

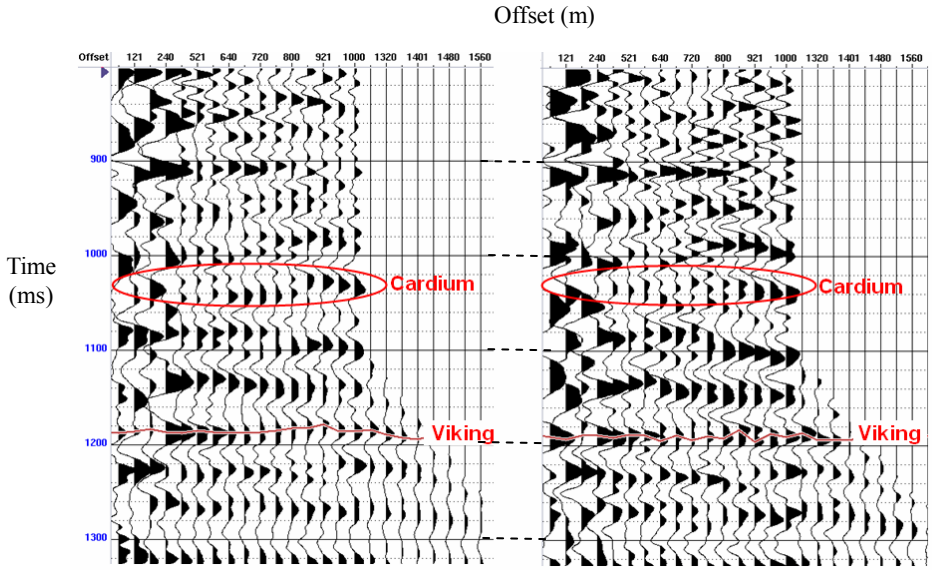


Figure 5.6 CDP gather 350 with NMO of line 1 at the location of $CO_2$ injection well 102/10-11-48-9W5 (baseline survey left, monitor survey right)

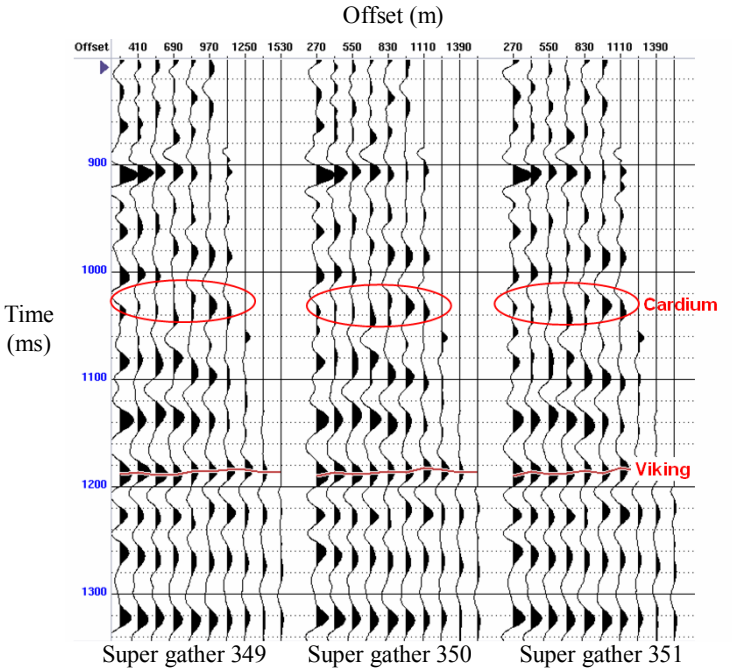


Figure 5.7 Three super-gathers of line 1 adjacent to the $CO_2$ injection well 102/10-11-48-9W5 (baseline survey, 5 adjacent CDPs were averaged).

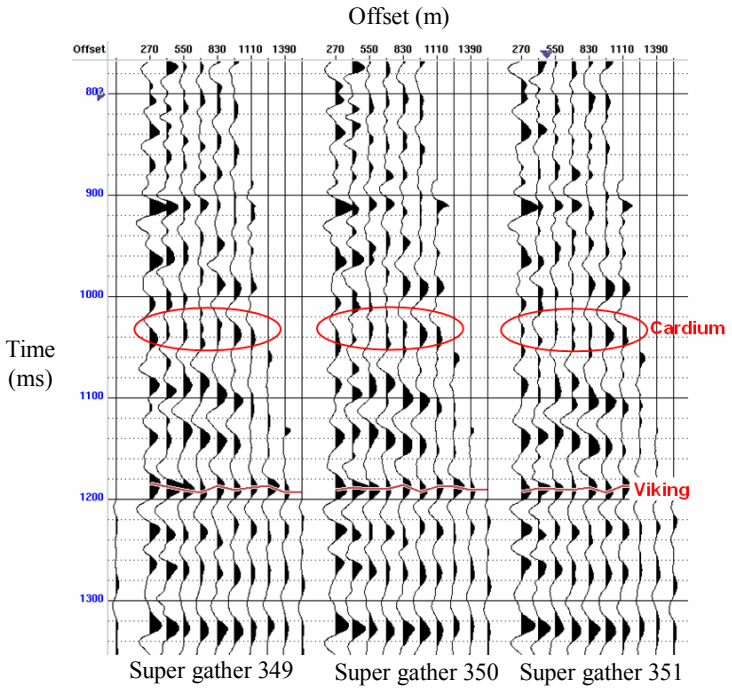


Figure 5.8 Three super-gathers of line 1 adjacent to the $CO_2$ injection well 102/10-11-48-9W5 (monitor survey, 5 adjacent CDPs were averaged).

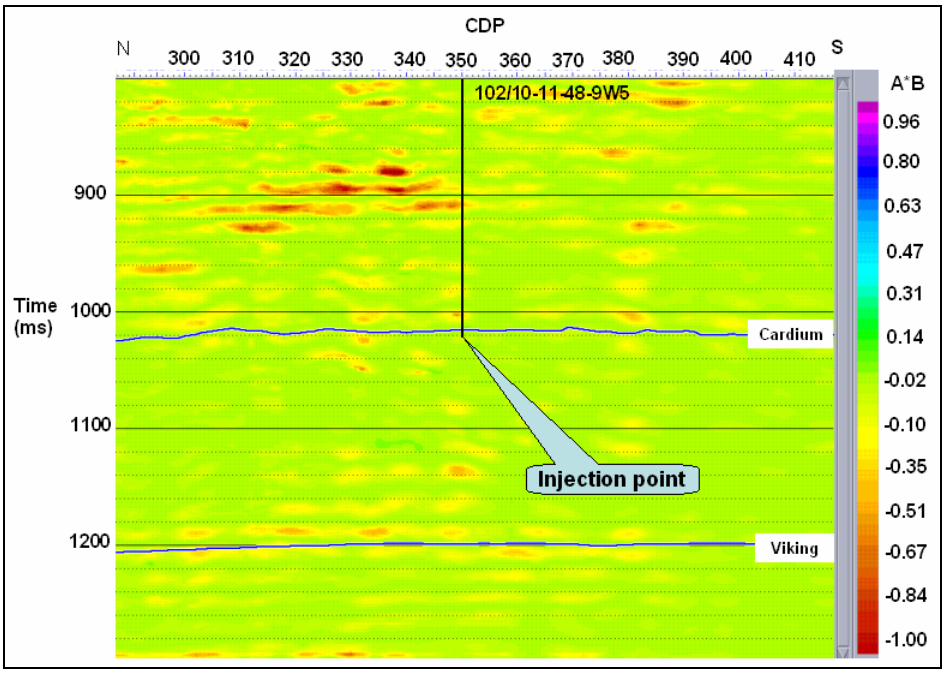


Figure 5.9 AVO inversion result of line 1 (baseline survey). The product of AVO intercept and gradient (A*B) is displayed in variable colors.

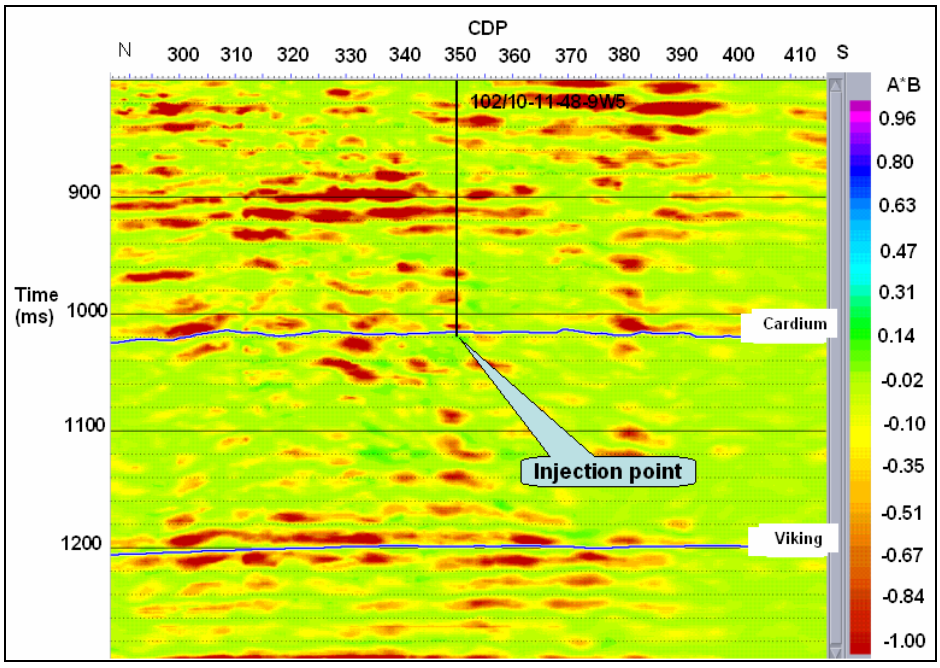


Figure 5.10 AVO inversion result of line 1 (monitor survey). The product of AVO intercept and gradient (A*B) is displayed in variable colors.

## 5.4 Chapter summary

Amplitude-versus-offset (AVO) technique is a useful tool for discriminating gas reservoirs, especially for gas reservoirs with bright spot anomalies. Seismic reflections from gas sands exhibit a wide range of AVO characters, which can be grouped into four classes based on their locations in the A-B plane and their normal incidence reflection coefficients. AVO modeling shows that the Cardium sand belongs to Class I AVO type or a type between Class I and Class II, and the injected $CO_2$ will produce a weak AVO anomaly in the Cardium reservoir. However, analysis of the field data did not show an identifiable change in AVO response before and after $CO_2$ injection. This may be due to noise within the data or that the $CO_2$ is confined to a much thin injection zone.

# CHAPTER 6: DISCUSSION AND CONCLUSIONS

## 6.1 Discussion

Although time-lapse technology has been used successfully to monitor $CO_2$ storage in some areas, such as in Sleipner gas field in North Sea and Weyburn oil field in Saskatchewan, Canada, the question arises after the Violet Grove time-lapse surface seismic data interpretation as to why time-lapse technology is not effective, at least so far, for monitoring the $CO_2$ distribution within the reservoir in the Violet Grove area. After comparing the reservoir properties at the Sleipner and at the Violet Grove $CO_2$ injection sites, some insights are gained.

In comparing the Violet Grove $CO_2$ project with the Sleipner $CO_2$ project (Table 6.1), there exist two main differences between them: the reservoir character and the $CO_2$ injection volume. Firstly, the Utsira reservoir at Sleipner consists of uncemented sands with high porosity (35% to 40%), large thickness (100-300m), and shallow burial depth (800-900 m) (Chadwick, et al., 2000). In contrast, the Cardium reservoir of Violet Grove consists of cemented sands with low porosity (10%-20%), small thickness (gross thickness is about 20m, and net thickness is only about 6 m) and greater burial depth (approximately 1650m). Secondly, for the Sleipner field, more than 2 million tonnes of $CO_2$ had been injected into the reservoir prior to shooting the first monitor survey; but for the Violet Grove, only approximately 20000 tonnes of $CO_2$ had been injected into the

reservoir prior to acquiring the first monitor survey. The anomaly corresponding to the injected $CO_2$ at the Violet Grove is not large enough to overwhelm the background differences between the monitor and baseline surveys. As a result, the injected $CO_2$ cannot be identified by the time-lapse seismic data at the Violet Grove at the time of the first monitor survey.

However, as more and more $CO_2$ is injected into the reservoir, the anomalies caused by $CO_2$ effect should become more obvious than at the time of the first monitor survey. As a result, it is possible that the $CO_2$ distribution in the Cardium reservoir may be identified by the next monitor survey.

| **Reservoir properties** | **The Cardium Sand** | **The Utsira Sand** |
|---|---|---|
| Location | The Pembina oil field in central Alberta, Canada | The Sleipner gas field in the North Sea |
| Trap type | Stratigraphic trap | Stratigraphic trap |
| Reservoir type | Cemented fine grained sand, with conglomerate | Uncemented fine grained sand, with medium and occasional coarse grains |
| Age | Upper Cretaceous | Mio-Pliocene |
| Burial depth | 1600m | 800-900m |
| Thickness | About 20m | 100-300m |
| Porosity | 10-15% | 35-40% |
| Formation water type | Fresh water originally, polluted by saline water | Saline water |
| Amount of CO2 injected by the shot of first monitor survey | Approximately 20000 tonnes | 2.34 million tonnes |
| Original reservoir velocity | About 4000m/s | About 2100m/s |
| P-wave velocity decrease after CO2 injection | About 5% | About 29% |

Table 6.1: Comparison between the properties of the Cardium sand and the Utsira Sand.

## 6.2 Conclusions

Time-lapse seismic technology was implemented at the Violet Grove $CO_2$ injection project, which is located at the center of the Pembina Oil Field. The baseline survey was shot in March 2005 prior to $CO_2$ injection; the first monitor survey was acquired in December 2005, after about 20,000 tonnes of $CO_2$ had injected. The baseline and monitor surface seismic data were acquired and processed by using the same acquisition parameters and processing flows. The repeatability of the baseline and monitor surveys is very high; several non-repeated shots were excluded from processing.

Fluid substitution modeling was accomplished by using Gassmann method. The modeling results show that after 90% $CO_2$ substitution, the P-wave velocity of the Cardium Sand decreases about 5% and the S-wave velocity increases about 1%, and the total time-shift corresponding to the injected $CO_2$ for the seismic signals of the Cardium Sand will be less than 1 ms. The modeling predicts that a modest amplitude difference will be generated around the Cardium reservoir after $CO_2$ injection.

Synthetic seismograms were made from two wells at the Violet Grove $CO_2$ injection site and they match the surface seismic data very well. The top of the Cardium sand correlates to a weak peak at approximately 1043 ms and 1690 ms in the PP and PS survey, respectively. Three steps of calibration, which are phase and time matching, shaping filter, and cross normalization, were applied to the monitor survey prior to 4D

seismic interpretation, and the monitor survey had a better match with the baseline survey after calibration.

Different time-lapse analysis methods, including time shift, amplitude difference, $V_p/V_s$, post-stack impedance inversion, and AVO were tested. Subtle changes at the Cardium Sand in the PS data and P-wave impedance inversion were found along Line 1 between the monitor and baseline surveys, but differences on Line 2 and 3 and in the 3D volume were less clear.

The analysis showed no significant changes in the seismic data above the reservoir, from which it is interpreted that no leakage is occurring from the reservoir. The lack of predicted anomalies at the Cardium level indicates also that the $CO_2$ is probably confined to a thin layer (<6m) of porous sand in the Cardium Formation.

**REFERENCES**

Aki, K., and Richards, P.G., 1980, Quantitative seismology-theory and methods, 1: W.H. Freeman and Co., San Francisco.

Arts, R., Eiken, O., Chadwick, A., Zweigel, P., Meer, L., and Zinszner, B., 2002, Monitoring of $CO_2$ injected at Sleipner using time lapse seismic data: Abstracts of the 6th international conference on greenhouse gas control technology (GHGT-6), Kyoto, Japan.

Arts, R., Elsayed, R., Meer, L., Eiken, O., Ostmo, S., Chadwick, A., Kirby, G., and Zinszner, B., 2002, Estimation of the mass of injected $CO_2$ at Sleipner using time-lapse seismic data: EAGE annual meeting, Florence, Italy.

Asghari, K., and Al-Dliwe, A., 2004, Optimization of carbon dioxide sequestration and improved oil recovery in oil reservoirs: the 7th international conference on greenhouse gas control technology (GHGT-7), Vancouver, Canada.

Bachu, S., 2000, Suitability of the Alberta subsurface for carbon-dioxide sequestration in geological media: Alberta Geological Survey, Alberta Energy and Utilities Board, Earth Sciences Report 00-11.

Bachu, S., Adams, J.J., Michael, K., and Buschkuehle, B.E., 2003, Acid gas injection in the Alberta Basin: a commercial-scale analogue for $CO_2$ geological sequestration in sedimentary basins: Alberta Geological Survey, Geoscience expertise and information on energy and mineral resources in Alberta, Canada.

Bachu, S., and Shaw, J., 2005, $CO_2$ storage in oil and gas reservoirs in Western Canada: effect of aquifers, potential for $CO_2$-flood enhanced oil recovery and practical capacity: the 7th international conference on greenhouse gas control technology (GHGT-7), Vancouver, Canada.

Baker Atlas, 2002, Introduction to wireline log analysis, Baker Hughes Inc..

Batzle, M., and Wang, Z., 1992, Seismic properties of pore fluids: Geophysics, 57, 1396-1408.

Bortfeld, R., 1961, Approximation to the reflection and transmission coefficients of plane longitudinal and transverse waves: Geophysical Prospecting, 9, 485-502.

Castagna, J.P., and Smith, S.W., 1994, Comparison of AVO indicators: a modeling study: Geophysics, 59, 1849-1855.

Castagna, J.P., Swan, H.W., and Foster, D.J., 1998, Framework for AVO gradient and intercept interpretation: Geophysics, 63, 948-956.

Chadwick, R.A., Holloway, S., Kirby, G.A., Gregersen, U., and Johannessen, P.N., 2000, The Utsira Sand, Central North Sea - An assessment of its potential for regional $CO_2$ disposal. In: Williams, D., Durie, B., McMullan, P., Paulson, C., and Smith, A.: Proceedings of the 5$^{th}$ International Conference on Greenhouse Gas Control Technologies, Cairns, Australia, CSIRO Publishing: 349-354.

Chen, F., and Lawton, D.C., 2006, Interpretation of baseline multi-component seismic data at the Violet Grove $CO_2$ injection site, Alberta: CSPG-CSEG-CWLS Convention abstract.

Christensen, N.I., and Wang, H.F., 1985, The influence of pore pressure and confining pressure on dynamic elastic properties of Berea sandstone: Geophysics, 50, 207-213.

Cooke, D.A., and Schneider, W.A., 1983, Generalized linear inversion of reflection seismic data: Geophysics, 48, 665-676.

Davis, T.L., Terrell, M.J., and Benson, R.D., 2003, Multi-component seismic characterization and monitoring of the $CO_2$ flood at Weyburn Field, Saskatchewan: the Leading Edge, 22, 696-697.

Domenico, S.N., 1977, Elastic properties of unconsolidated porous sand reservoirs: Geophysics, 42, 1339-1368.

Fatti, J.L., Smith, G.C., Vail, P.J., Strauss, P.J., and Levitt, P.R., 1994, Detection of gas in sandstone reservoirs using AVO analysis: a 3D seismic case history using the Geostack technique: Geophysics, 59, 1362-1376.

Gouveia, W.P., Johnston, D.H., Solberq, A., and Lauritzen, M., 2004, Characterization of fluid contact movement from time-lapse seismic and production logging tool data: the Leading Edge, 23, 1187-1194.

Graul, M., 2005, AVO: seismic lithology: SEG continuing education, Texseis Inc., Houston, Texas.

Gregory, A.R., 1976, Fluid saturation effects on dynamic elastic properties of sedimentary rocks: Geophysics, 41, 895-921.

Herawati, I., 2002, The use of time-lapse P-wave impedance inversion to monitor $CO_2$ flood at Weyburn Field, Saskatchewan, Canada: Thesis of the Reservoir Characterization Project, Colorado School of Mines.

Hilterman, F., 2001, Seismic amplitude interpretation: distinguished instructor short course, distinguished instructor series, No. 4, European Association of Geoscientists & Engineers.

Hilterman, F., Schuyver, C.V., and Sbar, M., 2000, AVO examples of long-offset 2-D data in the Gulf of Mexico: the Leading Edge, 19, 1200-1213.

Hilterman, F., Sherwood, J., Schellhorn, R., Bankhead, B., and Devault, B., 1998, Identification of lithology in the Gulf of Mexico: the Leading Edge, 17, 215-222.

Koefoed, O., 1955, On the effect of Poisson's ratios of rock strata on the reflection coefficients of plane waves: Geophysical Prospecting, 3, 381-387.

Krause, F.F., and Collins, H.N., 1984, Pembina Cardium recovery efficiency study: a geological and engineering synthesis: Petroleum Recovery Institute.

Krause, F.F., Collins, H.N., Nelson, D.A., Machemer, S.D., and French, P.R., 1987, Multi-scale anatomy of a reservoir: geological characterization of Pembina-Cardium

Pool, west-central Alberta, Canada: the American Association of Petroleum Geologists Bulletin, 71, 1233-1260.

Krebes, E.S., 2004, Seismic theory and methods: Geophysics 551 course notes, University of Calgary.

Landrø, M., Veire, H.H., Duffaut, K., and Najjar, N., 2003, Discrimination between pressure and fluid saturation changes from marine multi-component time-lapse seismic data: Geophysics, 68, 1592-1599.

Lawton, D.C., 2005, Seismic survey design for monitoring $CO_2$ storage: integrated multi-component surface and borehole seismic surveys, Penn West Pilot, Alberta, Canada: the 8$^{th}$ international conference on greenhouse gas control technology (GHGT-8), Trondheim, Norway.

Lawton, D.C., Coueslan, M., Chen, F., Bland, H., Jones, M., Gallant, E., and Bertram, M., 2005, Overview of the Violet Grove $CO_2$ seismic monitoring project: CREWES research report, 17, 1-24.

Li, G., 2003, 4D seismic monitoring of $CO_2$ flood in a thin fractured carbonate reservoir: the Leading Edge, 22, 690-695.

Lu, H.X., 2006, Velocity picking and offset range in Violet Grove 2D data processing: personal unpublished paper.

Lumley, D.E., 2004, Business and technology challenges for 4D seismic reservoir monitoring: the Leading Edge, 23, 1166-1168.

Meyer, R., 2001, 4D seismic and time-lapse reservoir geology: CREWES research report, 13, 895-906.

Miller, S., 1996, Multicomponent seismic data interpretation, M. Sc. thesis, University of Calgary.

Nielsen, A.R., and Porter, J.W., 1984, Pembina oil field-in retrospect: Canadian Society of Petroleum Geologists Memoir, 9, 1-13.

Nur, A., 1989, Four-dimensional seismology and (true) direct detection of hydrocarbons: the petrophysical basis: the Leading Edge, 8, 30-36.

Ostrander, W.J., 1984, Plane-wave reflection coefficients for gas sands at non-normal angles of incidence: Geophysics, 49, 1637-1648.

Patterson, N.R., 1957, Geology of Pembina field, Alberta: Bulletin of the AAPG, 41, 937-949.

Ross, C.P., 1985, Effective AVO crossplot modeling: a tutorial: Geophysics, 65, 700-711.

Ross, C.P., and Kinman, D.L., 1995, Non-bright-spot AVO: two examples: Geophysics, 60, 1398-1408.

Russell, B.H., 1988, Introduction to seismic inversion methods: Society of Exploration Geophysicists, Course Notes Series, No. 2, S.N. Domenico, Series Editor.

Rutherford, S.R., and Williams, R.H., 1989, Amplitude-versus-offset variations in gas sands: Geophysics, 54, 680-688.

Sheuy, R.T., 1985, A simplification of the Zoeppritz equations: Geophysics, 50, 609-614.

Smith, G.C., and Gidlow, P.M., 1987, Weighted stacking for rock property estimation and detection of gas: Geophysical Prospecting, 35, 993-1014.

Smith, G.C., and Sutherland, R.A., 1996, The fluid factor as an AVO indicator: Geophysics, 61, 1425-1428.

Smith, T.M., Sondergeld, C.H., and Rai, C.S., 2003, Gassmann fluid substitutions: a tutorial: Geophysics, 68, 430-440.

Sparkman, G., 1998, An introduction to this special section: time lapse or time elapse?: the Leading Edge, 17, 1386-1165.

Torp, T.A., and Gale, J., 2002, Demonstrating storage of $CO_2$ in geological reservoirs: The Sleipner and SACS projects: Abstracts of the $6^{th}$ international conference on Greenhouse Gas Control Technology (GHGT-6), Kyoto, Japan.

Verm, R., and Hilterman, F., 1995, Lithology color-coded seismic sections: the calibration of AVO cross plotting to rock properties: the Leading Edge, 14, 847-853.

Wang, Z., 1997, Feasibility of time-lapse seismic reservoir monitoring: the physical basis: the Leading Edge, 16, 1327-1329.

Wang, Z., 2001, Fundamentals of seismic rock physics: Geophysics, 66, 398-412.

Wang, Z., Cates, M.E., and Langan, R.T., 1998, Seismic monitoring of a $CO_2$ flood in a carbonate reservoir: A rock physics study: Geophysics, 63, 1604-1617.

Wang, Z., Hirsche, W.K., and Sedqwick, G., 1991, Seismic monitoring of water floods?-a petrophysical study: Geophysics, 56, 1614-1623.

Xue, Z., and Ohsumi, T., 2004, Seismic wave monitoring of $CO_2$ migration in water-saturated porous sandstone: Exploration Geophysics, 35, 25-32.

Yilmaz, O., 2001, Seismic data analysis: Society of Exploration Geophysicists, Tulsa.

Yu, G., 1985, Offset-amplitude variation and controlled-amplitude processing: Geophysics, 50, 2697-2708.

Zweigel, P., Arts, R., Bidstrup, T., Chadwick, A., Eiken, O., Gregersen, U., Hamborg, M., Johanessen, P., Kirby, G., Kristensen, L., and Lindeberg, E., 2001, Results and experiences from the first industrial-scale underground $CO_2$ sequestration case (Sleipner Field, North Sea): Extended abstract of oral presentation given at the annual meeting of the American Association of Petroleum Geologists (AAPG), Denver, Colorado.